Charge correlation using balance function of identified particles in heavy-ion collisions at LHC energy

by

Sk Noor Alam

Enrolment No. : **PHYS04201204006**

Variable Energy Cyclotron Centre, Kolkata

A thesis submitted to the Board of Studies in Physical Sciences
in partial fulfillment of the requirements for the degree of

Doctor of Philosophy

of

HOMI BHABHA NATIONAL INSTITUTE
Bhabha Atomic Research Centre
Mumbai-400085, India

November 2018

Version approved during the meeting of Standing Committee of Deans held during 29-30 Nov 2013

Homi Bhabha National Institute[1]

Recommendations of the Viva Voce Committee

As members of the Viva Voce Committee, we certify that we have read the dissertation prepared by Sk Noor Alam entitled "Charge correlation using balance function of identified particles in heavy-ion collisions at LHC energy" and recommend that it may be accepted as fulfilling the thesis requirement for the award of Degree of Doctor of Philosophy.

Chairman - Prof. Tapan Kumar Nayak		**Date:** 26/3/2019
Guide / Convener - Prof. Subhasis Chattopadhyay		**Date:** 26/3/2019
Co-guide - - (if any)		**Date:**
Examiner - Prof. Ajay Kumar Singh		**Date:** 26.3.19
Member 1- Prof. Sukalyan Chattopadhyay		**Date:** 26.3.19
Member 2- Dr. Zubayer Ahammed		**Date:** 26/3/2019

Final approval and acceptance of this thesis is contingent upon the candidate's submission of the final copies of the thesis to HBNI.

I/We hereby certify that I/we have read this thesis prepared under my/our direction and recommend that it may be accepted as fulfilling the thesis requirement.

Date: 26/3/2019

Place: VECC- KOLKATA

Guide

[1] This page is to be included only for final submission after successful completion of viva voce.

Version approved during the meeting of Standing Committee of Deans held during 29-30 Nov 2013

STATEMENT BY AUTHOR

This dissertation has been submitted in partial fulfillment of requirements for an advanced degree at Homi Bhabha National Institute (HBNI) and is deposited in the Library to be made available to borrowers under rules of the HBNI.

Brief quotations from this dissertation are allowable without special permission, provided that accurate acknowledgement of source is made. Requests for permission for extended quotation from or reproduction of this manuscript in whole or in part may be granted by the Competent Authority of HBNI when in his or her judgment the proposed use of the material is in the interests of scholarship. In all other instances, however, permission must be obtained from the author.

Sk. Noor Alam

Sk Noor Alam

DECLARATION

I, hereby declare that the investigation presented in the thesis has been carried out by me. The work is original and has not been submitted earlier as a whole or in part for a degree / diploma at this or any other Institution / University.

Sk. Noor Alam

Sk Noor Alam

List of Publications arising from the thesis

Journal

1. "Effect of simulating parity-odd observables in high energy heavy ion collisions on balance functions of charged particles and elliptic flow of pions"

Sk Noor Alam and Subhasis Chattopadhyay

Nuclear Physics A, 2018, 977, 208-216

Chapters in books and lectures notes

Communicated

1. S.N Alam and Subhasis Chattopadhyay: "Balance Functions of identified particles probing hadronisation time at LHC energy" (PRC)

Conferences

1. "Charge correlations using balance functions of identified particles in Pb-Pb collisions at $\sqrt{s_{NN}} = 2.76$ TeV with ALICE"
Sk Noor Alam on behalf of the ALICE collaboration.
https://doi.org/10.22323/1.314.0151 (EPS Conference, Venice , Italy)

2. "Model-based Simulation Of Correlation Between J/ψ and Charged Hadrons in p-p Collisions at LHC energy"
Sk Noor Alam and Subhasis Chattopadhyay
Nuclear Physics 2013, 58, 750

3. "J/ψ - hadron correlation at LHC energy to study the production mechanism of J/ψ"
Sk Noor Alam and Subhasis Chattopadhyay
Nuclear Physics 2015, 60, 790

4. "Deciphering the Charge Production Dynamics with General Charge Balance Functions in Pb-Pb Collisions $\sqrt{s_{NN}} = 2.76$ TeV at ALICE"
Sk Noor Alam on behalf of the ALICE collaboration
https://indico.cern.ch/event/433345/contributions/2373778/ (Quark Matter-2017, Chicago,U.S.A, 6-11 February, 2017)

ALICE Collaboration papers

1. B.Abeleve, et al., " Multiplicity dependence of jet-like two-particle correlation structures in p-Pb collisions at $\sqrt{s_{NN}} = 5.02$ TeV, Physics Letters B 741 (2015) 38-50

2. J.Adama, et al., " Multiplicity and transverse momentum evolution of charge-dependent correlations in pp, p-Pb, and Pb-Pb collisions at the LHC ", Eur. Phys. J. C (2016) 76:86

3. S. Acharya, et al., " Anisotropic flow of identified particles in Pb-Pb collisions at $\sqrt{s_{NN}} = 5.02$ TeV ", JHEP 09 (2018) 006

Analysis note

1. Sk Noor Alam , " Charge correlation using Balance Functions of Identified Particles in Pb-Pb collisions at $\sqrt{s_{NN}} = 2.76$ TeV" https://alice-notes.web.cern.ch/node/582

Sk. Noor Alam

Sk Noor Alam

Dedicated to my parents and grandparents

ACKNOWLEDGEMENTS

I thank my guide Prof. Subhasis Chattopadhyay for his constant supervision, training and constant motivation. It was never possible for me to continue my research works without his precious guidance and support. I thank Prof. Tapan Kumar Nayak for his constant encouragement and motivation. I thank Dr. Michael Weber and Dr. Panos christakoglou for spending their valuable time that helped me to get trained over the period of this work. I woud like to thank Prof. Dinesh K Srivastava and Prof. S.A Bass for valuable suggestions and encouragements. I would like to thank Dr. Alice Ohlson and Dr. Anthony Timmins for discussions and supports during PWG-CF meetings. I am very much grateful to Saikat Biswas. His advice on my research carrier has been very useful to me. I would like to thank Sidharth Kumar Prasad and Supriya Das for valuable discussions. I would like to thank Anand dubey,Premomoy Ghosh, Sanjib Muhuri and Partha Bhaduri for their suggestions in our weekly discussions. I thank my dear friends Arunabha,Asgar,Debasis,Koushik,Sarwar and Utsab for source of enthusiasm and inspiration in my life. I would like to thank Jane Alam,Saurav Sarkar,Asis Kumar Chowdhury,Zubayer Ahammed,D.N Basu,Asish Dhara and Prithwish Tribedy for helpful discussions and encouragements. I thank Srikanta, Pooja,Rahul,Ashpreet and Serdal for their help and suggestions. I would like to thank also my seniors Sumit Basu, Subikash, Debojit, Abhirup and my juniors Rajendra,Arghya,Pingal, Somnath,Ashik,Nachiketa,Mahfuzur,Sumit,sanchari,shreyashi,samrangy,Soumen, Santanu,Kalyan and Dipen for their constant support.

I express my gratitude to my parents and family members for their endless love.

SK. Noor Alam.

Sk Noor Alam

Contents

0.1 Synopsis

0.1.1 Introduction

Quantum Chromodynamics (QCD) is the theory of elementary particles that describes interaction among them via strong force. QCD predicts that there is a transition from hadronic phase to a phase of deconfined quarks and gluons known as Quark Gluon Plasm (QGP) at high temperature and/or high baryon density. Calculations of QCD using the lattice gauge theory predicts that a transition from hadronic phase to partonic phase occurs at temperature $T_c \approx 170$ MeV [1, 2, 3]. Main aim of the experiments using collisions of high energy heavy-ion such as, performed at the Relativistic-Heavy-Ion Collider (RHIC) and at the Large Hadron Collider (LHC) is to study the production of such a phase of matter. There are several experimental observables that are expected to probe the QGP state produced in collisions between heavy ions at ultra-relativistic energy [4, 5]. Strangeness enhancement is one of the main observable that suggests that a novel state of matter is created in heavy-ion collisions [6]. Observables related to correlations and fluctuations are used as powerful tools to study the properties of the created matter [7, 8, 9, 10, 11]. In this study, we have worked on two-particle correlations by measuring angular correlations between two particles represented by $\Delta\eta - \Delta\varphi$ where $\Delta\eta$ and $\Delta\varphi$ are difference between rapidity/pseudorapidity (η) and azimuthal angle (φ) pair of two particles called trigger $\&$ associated particles. One such observable, called the balance function (BF) is very sensitive to the charge separation between positively and negatively charged particles in rapidity/pseudorapidity and azimuthal plane as was first introduced by Steffen A. Bass , P. Danielewicz and S. Pratt [12]. Basic principle of BF is based on the fact that there is a local charge conservation i.e positive and negatively charges are produced at a same phase space point and they are strongly correlated in rapidity/pseudorapidity and azimuthal angle due to collective flow. Particles from central collisions are more strongly correlated in rapidity/pseudorapidity and azimuthal angle and result in narrower balance function. By studying balance functions of several hadronic species, one can gain insight into the chemical evolution of the Quark Gluon Plasma and radial flow. In this work, we have analysed this observable using data collected by the ALICE (A Large Ion Collider Experiment) for Pb-Pb collisions at 2.76 TeV at LHC using identified particles like pion as trigger particles. Width of the balance function distribution is a key parameter that is said to represent the hadronization time. The width in data is followed to be narrower in central collisions than peripheral collisions suggesting a long-lived QGP state. In section 2, we have discussed in detail two particle correlation function and the balance function. In section 3, we have given the details of data selection including the event and track selection procedure in ALICE experiment and then the results of balance function. In section 4, we have performed a model based study using balance function and elliptic flow of pions to simulate parity-odd observables i.e chiral magnetic effect (CME) using A Multi Phase Transport Model (AMPT). In section 5, we have concluded with a summary.

0.1.2 Two Particle Correlation and Balance Function

Two Particle Correlation

In this work, we have introduced two particle correlations using rapiditity/pseudorapidities (η) and azimuthal angles (φ) of particles. Two particle correlation is defined as

$$C(\Delta\eta, \Delta\varphi) = \frac{\frac{1}{N_{pairs}^{signal}} S(\Delta\eta, \Delta\varphi)}{\frac{1}{N_{pairs}^{mixed}} B(\Delta\eta, \Delta\varphi)}, \tag{1}$$

where S($\Delta\eta, \Delta\varphi$) is the signal distribution and B($\Delta\eta, \Delta\varphi$) is the background distribution. In the signal distribution, trigger and associated particles are chosen from the same event. In the background distribution, trigger and associated particles are chosen from different events. We have chosen trigger particle's transverse momentum (p_T) to be greater than that of the associated particle. The signal distribution is expressed as:

$$S(\Delta\eta, \Delta\varphi) = \frac{d^2 N_{pairs}^{signal}}{d(\Delta\eta) d(\Delta\varphi)} \tag{2}$$

where N_{pairs}^{signal} gives the number of pairs per event. Similary the background distribution is expressed as:

$$B(\Delta\eta, \Delta\varphi) = \frac{d^2 N_{pairs}^{mixed}}{d(\Delta\eta)(\Delta\varphi)} \tag{3}$$

where N_{pairs}^{mixed} is the number of pairs per event from the mixed events. Differences between pseudorapidities and azimuthal angles between trigger and associated particles are defined as

$$\Delta\eta = \eta_{trigger} - \eta_{associated} \tag{4}$$

$$\Delta\varphi = \varphi_{trigger} - \varphi_{associated} \tag{5}$$

In Fig. 5-3, we have shown distributions of signal, background and ratio as an illustration for Pb+Pb collisions at $\sqrt{s_{NN}}$=2.76 TeV .

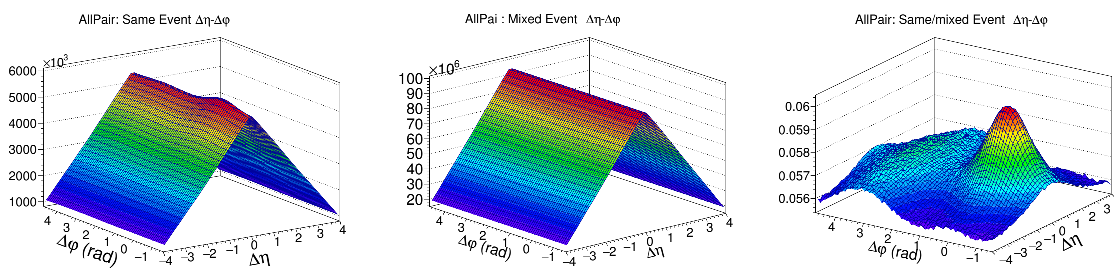

Figure 0-1: $\Delta\eta - \Delta\varphi$ plot of same event (left) , mixed event (middle) and correlation i.e same/mixed (right)

Balance Function

Particles are produced from space time evolution of quarks and gluons. There are very strong spatial correlation between quarks and anti-quarks at the early stage. As the system expands, correlations are affected by difusion and rescattering. So in case quark anti-quark pairs are produced early , their initial spatial correlation gets diluted at freeze-out. If quark anti-quark pairs are produced late , initial correlations will remain unaffected. Therefore, the BF of the produced hadrons carry information on the hadronization time of hot and dense medium created at the collisions. The time clocked by the balance function therefore represents the lifetime of the medium. Balance function is defined as a conditional probability of observing a charge with respect to another charge [12]. It is defined as

$$B = \frac{1}{2}\Big[\frac{\langle N_{(a,b)}\rangle}{\langle N_a\rangle} - \frac{\langle N_{(b,b)}\rangle}{\langle N_b\rangle} + \frac{\langle N_{(b,a)}\rangle}{\langle N_b\rangle} - \frac{\langle N_{(a,a)}\rangle}{\langle N_a\rangle}\Big], \tag{6}$$

here $\frac{\langle N_{(a,b)}\rangle}{\langle N_a\rangle}$ is the conditional probability of observing a particle of type *b* within a relative separation i.e $\Delta\eta =\mid \eta_a - \eta_b \mid$ or $\Delta\phi =\mid \phi_a - \phi_b \mid$ with respect to a particle type *a*. Particle type *a* and *b* are used as trigger particle and associated particles respectively. $\langle N_{(a,b)}\rangle$ is the number of pairs that satisfies relative separation condition which is a function of relative separation and transverse momenta of trigger and associated particles i.e $\langle N_{(a,b)}(\Delta\eta, \Delta\phi, p_{\mathrm{T,trig}}, p_{\mathrm{T,asso}})\rangle$.

0.1.3 ALICE data analysis

Event and track selection

Extraction of BF with identified particles as trigger has been performed using Pb-Pb dataset at $\sqrt{s_{NN}}$ = 2.76 TeV as collected by ALICE in 2010. Approximately 12 M minimum bias events were used for this analysis. Only events with a valid reconstructed vertex and with z position of the vertex $\mid V_z \mid< 10$ cm were analysed. The events were divided in different centrality classes, spanning 0-80$\%$ of the total inelastic cross section. The most central events were analyzed in 5$\%$ bins (0-5$\%$ and 5-10$\%$) and the peripherals in 10$\%$ bins. The centrality of an event was estimated by using the multiplicity distribution of signals from the V0 detectors. Primary tracks are reconstructed, selected [13] and identified [14] using the Time

Projection Chamber (TPC) and the Time-Of-Flight detector (TOF). Here, the $n\sigma$ method is used to identify particles where $n\sigma$ is defined as

$$n\sigma = \frac{signal_{pid} - signal_{expected}}{\sigma} \tag{7}$$

Here, signal means $\beta = \frac{v}{c}$ and relative energy loss w.r.t distance for TOF and TPC respectively. The TPC is used for identification of particles with p_T of 0.2 to 0.6 GeV/c. The combination of TPC and TOF information have been used for identification of particles with p_T of 0.6 to 1.4 GeV/c. Fig. 0-2 shows TPC and TOF signals extracted from Pb-Pb collisions with $\sqrt{s_{NN}}$ = 2.76 TeV energy. In this work, we have selected pions as trigger $\&$ associated particles. The correlation functions have been corrected for efficiency $\&$ purity obtained from simulated data.

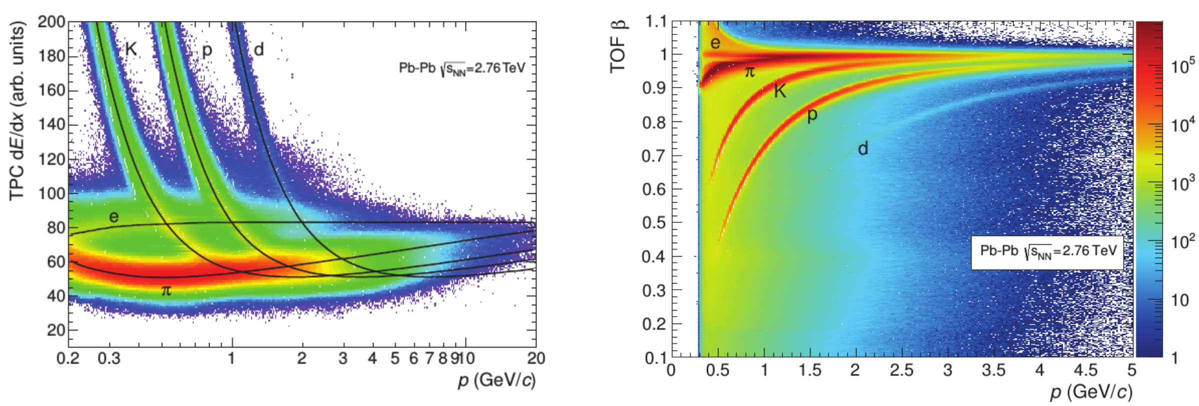

Figure 0-2: Left: Specific energy loss (dE/dx) in the TPC vs. particle momentum in Pb-Pb collisions at $\sqrt{s_{NN}}$ = 2.76 TeV. The lines show the parametrisation of the expected mean energy loss. Right: Distribution of β as measured by the TOF detector as a function of momentum for particles reaching the TOF in Pb-Pb interactions. Figures are taken from [14].

Results

Width of the BF provides information on the hadronisation time of particles produced in the collisions. Width is calculated using the RMS value or the weighted average of the BF distributions projected in Δy and $\Delta\varphi$. The results for identified charged pion pairs are shown in Fig. 0-3. The correlation functions have a dip near $\Delta y = 0$ and $\Delta\varphi = 0$. This dip might be a combined effect of Bose-Einstein correlations and Coulomb interactions between charged pions. Widths of the balance functions for three centrality classes are shown in Fig. 5-4. A significant narrowing of the BF width of pions with increasing centrality is observed. The broadening of the balance functions for less central collisions is a result of a larger separation between balancing charges. This centrality dependence is consistent with two scenarios: delayed hadronisation and increasing radial flow.

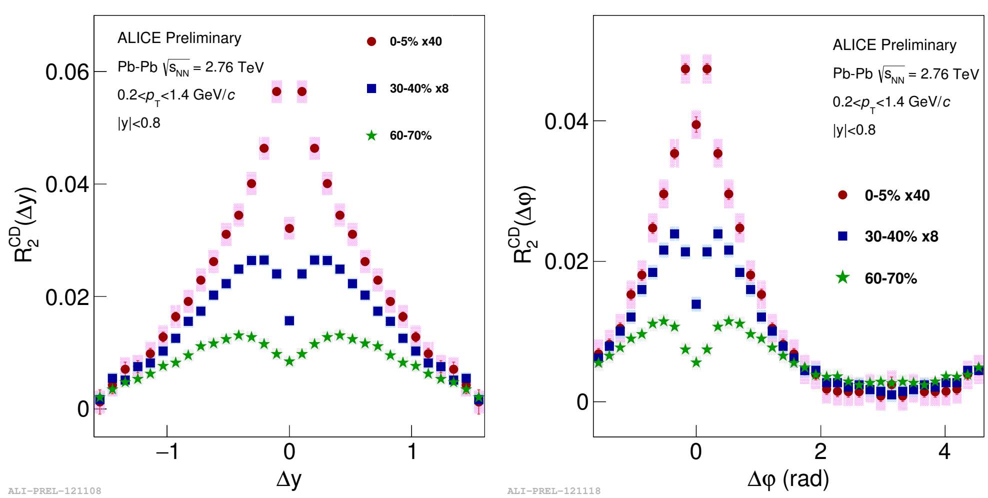

Figure 0-3: The balance function versus y (left plot) and azimuthal angle (φ) (right plot) for identified pion pairs from central and peripheral Pb-Pb collisions at $\sqrt{s_{NN}}$= 2.76 TeV

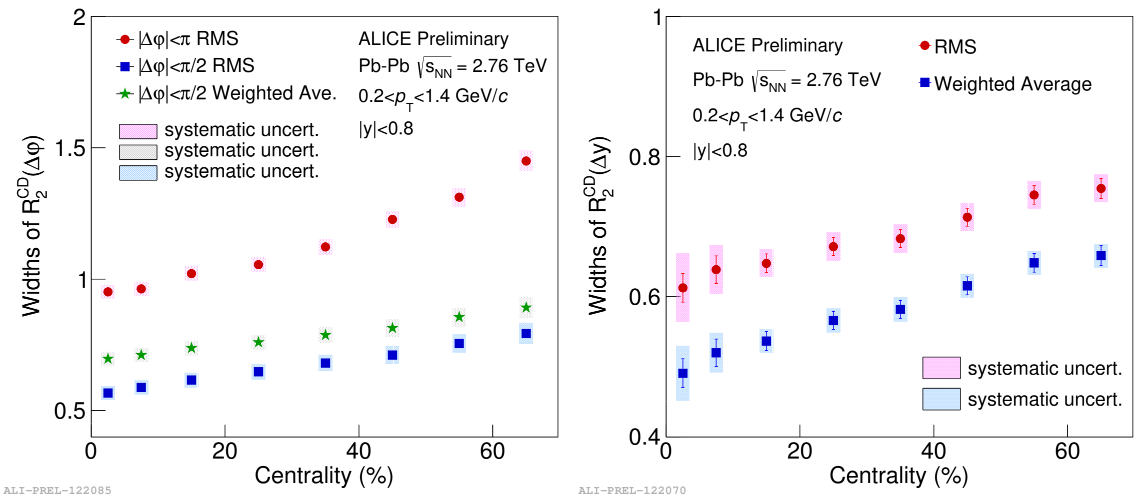

Figure 0-4: The width of the balance function for pions in terms of $\langle \Delta y \rangle$ and $\langle \Delta\varphi \rangle$ as a function of centrality. Error bars shown are systematic. The width in $\Delta\varphi$ is shown for different ranges in $\Delta\varphi$ when projecting.

0.1.4 Parity-odd observables using balance function of charged particles and elliptic flow of pions in high energy heavy-ion collisions

At the early stage of heavy ion collisions, non-trivial topologies of the gauge fields can be created resulting in an imbalance of axial charge density and eventually separation of electric charges along the direction of the magnetic field produced in such collisions. This process is called the chiral magnetic effect (CME) [15, 16, 17, 18, 19]. In this work we implement such a charge separation at the partonic level in AMPT for Au+Au collisions at $\sqrt{s_{NN}}$ = 200 GeV to study its consequence on experimental observables. We present the effects on the pion elliptic flow (v_2) and the charged particle balance function (BF) for varying strengths of initial charge separation. Charge balance functions show a peak at $\Delta\phi \sim 180$ with charge separation implemented in the partonic level as expected for the parity violation. We find that the shape of the balance function is sensitive to the increasing charge separation. v_2 of pion shows a strong decreasing trend at higher transverse momenta (p_T) with increasing charge separation [20].

We have also calculated parity observable γ_P in the form of BF's moments. γ_P is defined as

$$\gamma_P =< \cos(\phi_1 + \phi_2 - 2\psi_{RP}) > \tag{8}$$

where ψ_{RP} is the reaction plane angle and ϕ_1 , ϕ_2 denote the azimuthal angles of the produced charged particles. γ_P shows a decreasing trend with charge separation. It has a negative value for charge separation produced by flipping higher than 30 $\%$ of quarks in the parton level. We also notice that $< \gamma_P >$ for the same charge correlation and the opposite charge correlation shows negative and positive values, respectively.

We have calculated these parity violation terms in the form of balance function moments. We know $\gamma_P = \cos(\phi_i + \phi_j) = \cos(2\phi_i)\cos(\Delta\phi) - \sin(2\phi_i)\sin(\Delta\phi)$ where P stands for parity and $\Delta\phi = \phi_j - \phi_i$. γ_P can be expressed when weighted with azimuthal distribution of particles as

$$\gamma_P = \langle C_b \cos(2\phi)\rangle - \langle S_b \sin(2\phi)\rangle \tag{9}$$

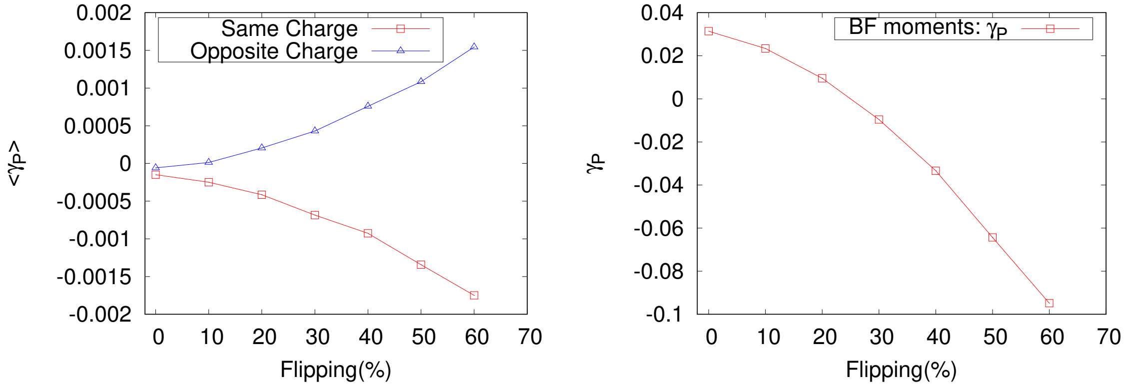

Figure 0-5: $<\gamma_P>$ with different flipping fractions (left plot) ; γ-correlator in the form of BF's moment with different flipping fractions (right plot)

where

$$C_b = \frac{1}{Z_b} \int d\Delta\phi B(\Delta\phi) \cos(\Delta\phi), \tag{10}$$

$$S_b = \frac{1}{Z_b} \int d\Delta\phi B(\Delta\phi) \sin(\Delta\phi), \tag{11}$$

$$Z_b = \int d\Delta\phi B(\Delta\phi) \tag{12}$$

Z_b is integral of balance function used as normalization factor.

Left plot of Fig. 5-7 shows that $<\gamma_P>$ with same charges and opposite charges have negative and positive values respectively. This figure indicates that gamma correlator has larger magnitudes with higher flipping fraction for both same and

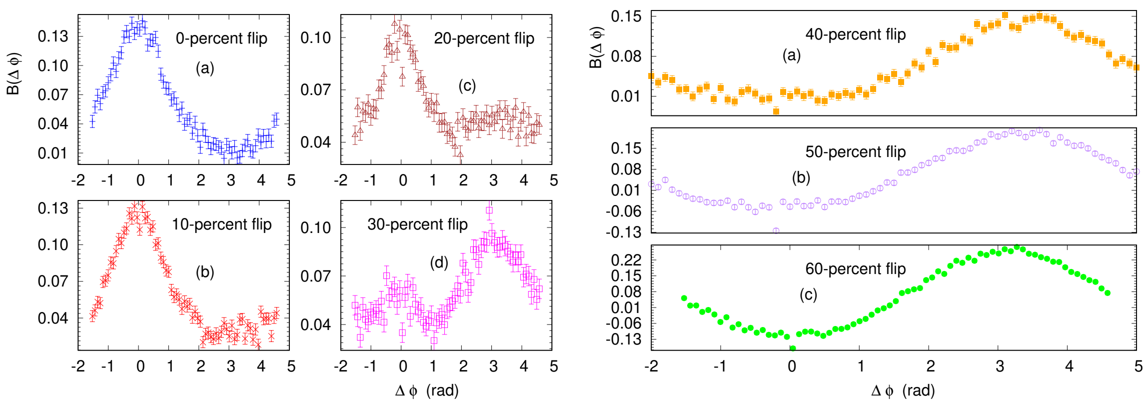

Figure 0-6: BF for Au+Au minimum bias at $\sqrt{s_{NN}}$ = 200 GeV with different flipping fractions from 0 to 60 %

opposite charge correlation. Right plot of Fig. 5-7 shows that the parity odd observable in form of BF moments becomes negative when flipping fraction is $\sim$ 30 % or higher.

From Fig. 0-6 , it is clearly seen that the shape of the balance function evolves with the flipping fraction. It shows a peak$\sim 0^c$ when there is no flipping. The peak shifts towards π^c when flipping for charge separation is 30 % or greater.

In Fig. 5-5, it is observed that the elliptic flow of pion increases upto $p_T \sim$ 1.1 GeV/c and then decreases at higher p_T. There is an increase in out-of plane particle production , so v_2 shows a decreasing trend for higher flipping fractions.

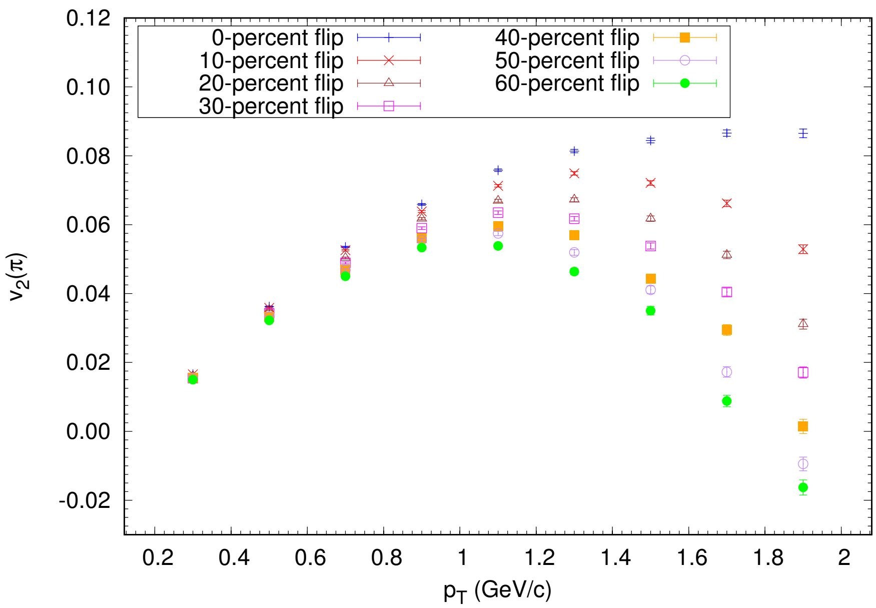

Figure 0-7: Elliptic flow of pions for different flipping fractions and no flip

0.1.5 Summary

Two particle correlation is an useful tool to study the production mechanism in high energy heavy-ion collisions. A form of this two particle correlation called balance function represents the correlation between oppositely charged particles. The balance function represents the hadronization time of the produced particles. BF can be measured using identified or non-identified trigger/associated particles. The width of the BF in case of identified particles helps to differentiate two possible scenarios i.e delayed hadronization or radial flow.
In this work, ALICE data have been used to measure balance functions of identified particles. We have measured the balance function distributions for Pb-Pb collisions at $\sqrt{s_{NN}}$ = 2.76 TeV taken by ALICE experiment for pions as trigger and associated particles. We have observed that the balance function in terms of Δy and $\Delta\varphi$ for pions decrease when moving from peripheral to central collisions. It is consistent with the picture of a delayed hadronisation.

In this study, momenta of initial partons of AMPT generator have been flipped to generate an out-of-plane charge separation in Au+Au collisions at $\sqrt{s_{NN}}$ = 200 GeV. The fraction of a type of quark(u,$\bar{u}$,d,$\bar{d}$) has been taken as a variable. This charge separation represents the effect of parity-odd observable in heavy ion collisions where magnetic fields are generated. We have studied the effect of this charge separation on two widely used observables i.e charge particle BF and elliptic flow of pions. γ-correlator has also been used for comparison. The observables are chosen in such a way that they characterize the effect of net-charge and their

distribution on azimuthal plane. Different fractions represent varying centrality in such collisions. In this study, with varying fraction of flipping, both the BF and v_2 show significant sensitivity with the peak of the BF shifting from $\Delta\phi = 0$ towards $\Delta\phi = \pi$ with increasing flipping fraction and v_2 of pions decreases at higher p_T. The reduction in v_2 with respect to no-flipping scenario depends on the flipping fraction. The gamma correlator in form of BF moment with different flipping fraction shows a decreasing trend. We also notice that $< \gamma_P >$ for same charge correlation and opposite charge correlation have opposite values and varies with charge separation. Experimentaly, the STAR has an upper limit for the value of gamma correlator of the order of $10^{-}3$. We have observed that the gamma correlator of $\approx 10^{-}3$ corresponds to flipping fractions range of 0 to 60%. We hereby propose to look at both the observables i.e BF and elliptic flow together for making an unambiguous conclusion on the generation of parity-odd effects in high energy heavy ion collisions.

Bibliography

[1] E. Shuryak, "A "little bang" arrives at the lhc," Physics, vol. 3, p. 105, Dec 2010. 6.

[2] Z. Fodor and S.D. Katz: "Lattice determination of the critical point of QCD at finite T and μ", JHEP 0203, 014 (2002) 24, 25, 29, 97, 99.

[3] C.R. Allton et al.: "The Equation of state for two flavor QCD at nonzero chemical potential", Phys. Rev. D68, 014507 (2003) 97.

[4] M.Aggarwal et.al., Nucl. Phys. A610, 200c (1996)

[5] S. A. Bass, M. Gyulassy, H. StoÂÍcker, and W. Greiner, J. Phys. G 25, R1 (1999)

[6] WA97 Collaboration, E. Andersen et al., Phys. Lett. B 433, 209 (1998); WA97 Collaboration, R. Lietava et al., J. Phys.G 25, 181 (1999); WA97 Collaboration, R. Caliandro et al., J. Phys. G 25, 171 (1999); NA49 Collaboration, S. Margetis et al., J. Phys. G 25, 189 (1999); NA49 Collaboration, F. Gabler et al., J. Phys. G 25, 199 (1999); WA85 and WA94 Collaborations, D. Evans et al., J. Phys. G 25, 209 (1999).

[7] S. Jeon and V. Koch, Phys. Rev. Lett. 85, 2076 (2000)

[8] M. Asakawa, U. Heinz, and B. MuÂÍller, Phys. Rev. Lett. 85, 2072 (2000).

[9] Zi-wei Lin and C. M. Ko, Phys. Rev. C 64, 041901 (2001)

[10] H. Heiselberg and A. D. Jackson, Phys. Rev. C 63, 064904 (2001).

[11] E.V. Shuryak and M. A. Stephanov, Phys. Rev. C 63, 064903 (2001).

[12] S. A. Bass, P. Danielewicz and S. Pratt: "Clocking Hadronization in Relativistic Heavy-Ion Collisions with Balance Functions", Phys. Rev. Lett. 85, (2000) 2689.

[13] J. Adam et al. [ALICE Collaboration], Eur. Phys. J. C 76 (2016) 86

[14] J. Adam et al. [ALICE Collaboration], Int. J. Mod. Phys. A 29 (2014) 1430044

[15] A. A. Belavin, et al., Phys. Lett. 59B, 85 (1975).

[16] G.Hooft, Phys. Rev. Lett. 37, 8 (1976); Phys. Rev. D 14,3432 (1976).

[17] Kenji Fukushima,Dmitri E. Kharzeev,and Harmen J. Warringa, Phys. Rev D 78, 074033 (2008).

[18] Dmitri E. Kharzeev, Larry D. McLerran , Harmen J. Warringa a,Nuclear Physics A 803 (2008) 227-253.

[19] L.D. McLerran, E. Mottola, M.E. Shaposhnikov, Phys. Rev. D 43 (1991) 2027

[20] S.N.Alam , S. Chattopadhyay, Nulcear Physics A 977(2018) 208-216

List of Figures

List of Tables

Chapter 1

Introduction

1.1 Standard Model and quantum Chromodynamics

Standard Model

According to the standard model (SM), all matters are composed of three kinds of elementary particles (leptons , quarks , and mediators). Leptons and quarks have spin-$\frac{\hbar}{2}$. We can classify leptons according to charge (Q), electron number (l_e), muon number (l_μ) and tau number (l_τ). A table 1.1 is drawn below to give an idea about lepton's Q, l_e, l_μ, and l_τ numbers.

There are also antiparticles of leptons i.e antileptons which have reversed quantum numbers with respect to leptons. For example, an electron carries a charge of -1 and a positron carries a charge of +1. Similarly quarks are classified by charge, strangeness (S), charm (C), beauty (B) and truth(T). We can divide quarks and leptons into three generations according to mass and quantum numbers. 1) First gen-

Table 1.1: Lepton's charge, electron number, muon number and tau number.

Lepton					
generation	l	Q	l_e	l_μ	l_τ
I	e	-1	1	0	0
	ν_e	0	1	0	0
II	μ	-1	0	1	0
	ν_μ	0	0	1	0
III	τ	-1	0	0	1
	ν_τ	0	0	0	1

eration: electron,electron neutrino, up quark and down quark. 2) Second generation: muon, muon neutrino, strange quark and charm quark. 3) Third generation: Tau, tau neutrino, bottom and top quark. It is shown in table 1.2. Antiquarks

Table 1.2: Quark's charge, strangeness, charm, beauty ,truth number.

Quark						
generation	q	Q	S	C	B	T
I	d	-1/3	0	0	0	0
	u	2/3	0	0	0	0
II	s	-1/3	-1	0	0	0
	c	2/3	0	1	0	0
III	b	-1/3	0	0	-1	0
	t	2/3	0	0	0	1

have reversed quantum numbers. Now, one of the most important questions is how these quarks and leptons will interact among each other. There are four fundamental interactions: gravitational , electromagnetic, strong and weak. There are different kinds of mediators for each interaction. γ is the mediator for electromagnetic interaction. There are three carriers i.e W^+, W^-, Z^0 used to describe the weak interaction. Carriers of strong interaction are 8 types of gluons with different combinations of colour charges. In the standard model, gravity is not included.

Masses of quark and lepton (MeV/c^2)			
lepton	mass	quark	mass
ν_e	$< 2 \times 10^-6$	u	2
ν_μ	< 0.2	d	5
ν_τ	< 18	s	100
e	0.511	c	1200
μ	106	b	4200
τ	1777	t	174000

Table 1.3: Quark and lepton masses (MeV/c^2)

Masses of quarks and leptons are shown in table 1.3. It has been observed that leptons are free particles where quarks compose particles. Mesons are composed of one quark $\&$ one anti-quark and baryons are composed of three quarks[1]. The leptons with heavier masses decay to electron and neutrinos (ν_e, ν_μ, ν_τ). Heavier mass lepton like muon (μ) decays to electron, muon neutrino and anti-electron neutrino ($\mu \rightarrow e + \nu_\mu + \bar{\nu}_e$). In this decay mode, lepton number is conserved. The mechanism which breaks electroweak symmetry in the SM recently has been verified experimentally [3]. This mechanism [4, 5, 6, 7, 8, 9] gives mass to elementary massive particles. This mechanism implies that there is a scalar particle called Higgs Boson (H). Higgs boson can decay to several channels. Some of decay channels are $H \rightarrow ZZ^{(*)} \rightarrow 4l$, $H \rightarrow \gamma\gamma$ and $H \rightarrow WW^{(*)} \rightarrow e\nu\mu\nu$. Fig. 1-1 shows invariant mass spectrum of diphoton from pp collisions at $\sqrt{S}$ = 7 TeV and 8 TeV measured by ATLAS. Here $H \rightarrow \gamma\gamma$ decay channel is considered. This result provides an evidence of new particle with mass around 126 GeV.

SM is not an ultimate theory. It proves many experimental results. But gravi-

[1]LHCb's recent results have shown that there are particles which are composed of five quarks[1].

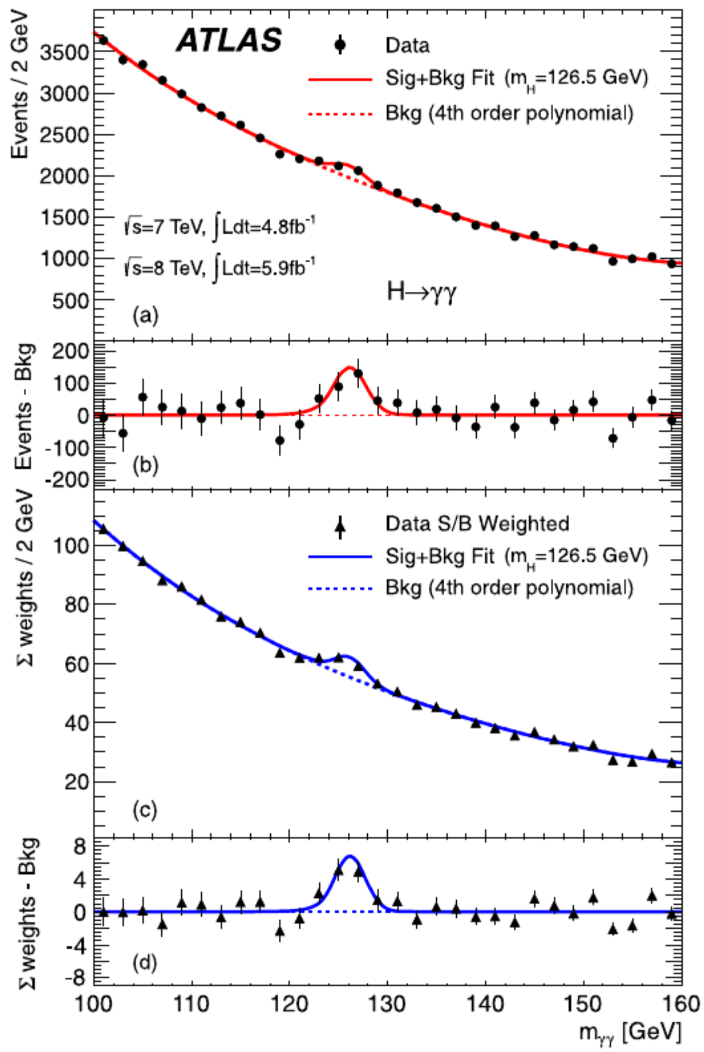

Figure 1-1: (Color online) Distribution of invariant mass spectrum of diphoton from pp collisions at $\sqrt{S}$ = 7 TeV and 8 Tev respectively. Background of diphoton reconstruction is elliminated from signal by fitting fourth-order Bernstein polynomial. Here $H \to \gamma\gamma$ decay channel is considered. It is observed from lower panel that Higgs boson has mass around 126.5 GeV [3].

tational interaction which mostly interact between all kind of massive particles is not included in SM. In next paragraph, interaction between quarks and gluons is described. This interaction theory is called Quantum Chromodynamics.

Quantum Chromodynamics

The strong interaction between quarks is described by a theory of gauge group SU(3)$_c$ where c stands for color of quarks. This theory is called Quantum Chromodynamics (QCD). Each quark takes one color among three values; R=red, G=green, B=blue. There are 9 possible ways for a gluon to interact between an initial and a final quark. Eight gluons form an octet of SU(3) group [10],

$$\begin{aligned}
&g_1 = R\bar{G} \qquad g_2 = R\bar{B} \qquad g_3 = G\bar{R} \\
&g_4 = G\bar{B} \qquad g_5 = B\bar{R} \qquad g_6 = B\bar{G} \\
&g_7 = \frac{1}{\sqrt{2}}(R\bar{R} - G\bar{G}) \\
&g_8 = \frac{1}{\sqrt{6}}(R\bar{R} + G\bar{G} - 2B\bar{B})
\end{aligned} \tag{1.1}$$

SU(3) singlet is

$$g_0 = \frac{1}{\sqrt{3}}(R\bar{R} + G\bar{G} + B\bar{B}) \tag{1.2}$$

SU(3) color symmetry is carried out by octet of gluons and the three colors. The Lagrangian form of QCD is given by

$$\mathcal{L}_{QCD} = \sum_q \left(\bar{\psi_{q_i}} i\gamma^\mu \left[\delta_{ij}\partial_\mu + ig\left(G^\alpha_\mu t_\alpha\right)_{ij}\right]\psi_{q_j} - m\bar{\psi_{q_i}}\psi_{q_i}\right) - \frac{1}{4}G^\alpha_{\mu\nu}G^{\mu\nu}_\alpha \tag{1.3}$$

where $G^{\mu\nu}_{\alpha}$ is color field tensor and it is defined as

$$G^{\mu\nu}_{\alpha} = \partial^{\mu} G^{\nu}_{\alpha} - \partial^{\nu} G^{\mu}_{\alpha} - g f^{\alpha\beta\gamma} G^{\mu}_{\beta} G^{\nu}_{\gamma} \tag{1.4}$$

Here G^{ν}_{α} represents the four potentials of gluonic fields ($\alpha = 1, ..8$). q is the flavour index (q = u,d,s,c,b,t), ψ_i is the DIRAC spinor of quark field(i represents color), t_{α} is 3×3 Gell-Mann matrices (basically generators of SU(3) group), $f^{\alpha\beta\gamma}$ is the structure constant of SU(3) group, $g = \sqrt{4\pi\alpha_s}$ where α_s is the strong coupling constant. m is the mass of quark. As a result of the gluon self coupling, QCD entails that strength of coupling i.e α_s has a large value at a large distance. Strength of coupling constant depends on momentum transfer Q.

$$\alpha_s(Q^2) = \frac{1}{\beta_0 \ln(\frac{Q^2}{\lambda^2})} \tag{1.5}$$

where $\beta_0 = \frac{33-2N_f}{12\pi}$. Here N_f is the number of quark flavours. Technically, λ is similar to energy scale Q where $\alpha_s(Q^2)$ goes to infinity.

From equation 1.5, it is observed that QCD has two unique properties: color confinement and asymptotic freedom [11, 12, 13, 14]. At low energy, confinement is dominant and at high energy asymptotic freedom is dominant.

Fig. 1-2 shows QCD coupling constant as a function of Q for different measurements.

- **Color confinement:** When distance between two quark increases, coupling constant becomes so strong that it is impossible to obtain free quarks from hadrons. This property is called confinement. So at low momentum trans-

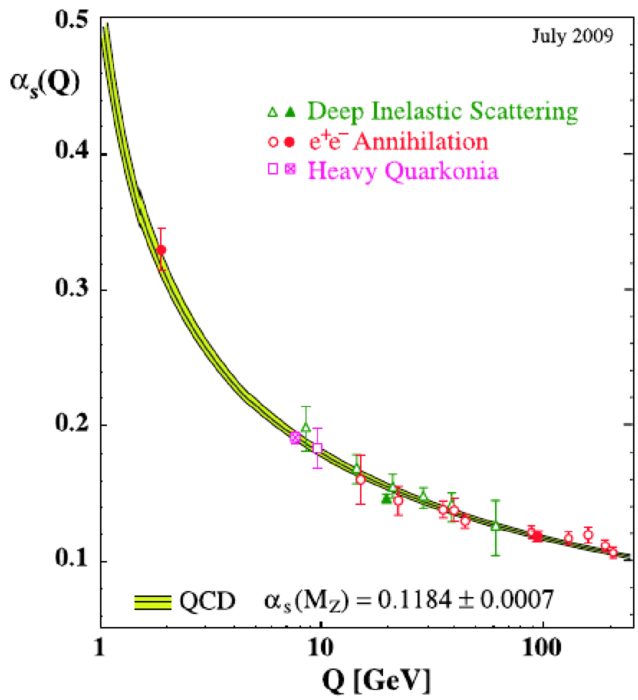

Figure 1-2: (Color online) Summary of measurements of α_s as a function of momentum transfer Q. Results from N3LO QCD are shown by full symbols. Open circles are from NNLO QCD theory and Open triangles/sqaures are from NLO QCD theory [15].

fer, therefore, it is impossible to find quarks and gluons as independent particles. Energy required for separation of quarks is almost infinite. New quarks and gluons are however obtained in case of higher momentum transfer. These produced quarks and gluons form hadrons. Because of this, there are no color charged particles which move independently. So color charged particles are confined always in hadrons. Hadrons are therefore colorless.

- **Asymptotic freedom:** At very short distances, there is almost no interaction between particles. It is because of large momentum transfer at short distances and coupling constants acquire low values. Partons are therefore asymptotically free at short distances. Asymptotic freedom is responsible for creating a state at extreme temperature where quarks and gluons, building blocks of matter are deconfined. This deconfined state of quarks and gluons is called quark-gluon-plasm (QGP).

1.2 Quark-Gluon-Plasma

Deconfinement of quarks and gluons at extremely high temperature constitute a state of matter called QGP [16]. A few microseconds after the Big Bang, this state of matter is said to be produced. R.Hagedron suggested that particles of different masses are primarily controlled by temperature and after attaining a temperature more particles will be produced for extra energy instead of enhancing the temperature to system [17]. This temperature is called the Hagedron temperature and its value is 170 MeV. There is therefore a transition from ordinary matter to the deconfined phase at this Hagedron temperature [18, 19, 20, 21]. Non-perturbative latice QCD calculation is performed to understand this transition [22, 23, 24]. Fig. 1-3 shows latice QCD calculation of energy desity as a function of temperature of hadronic matter at zero baryonic potential.

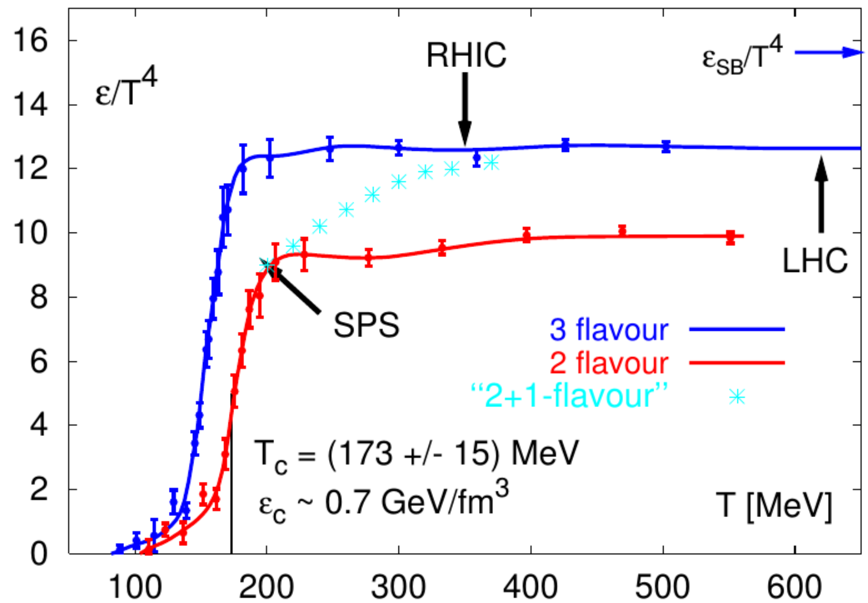

Figure 1-3: (Color online) The energy density of QCD as a function of temperature. The latice calculations are performed for two massless quarks, three massless quarks and two massless quark plus one with its actual real mass. It is observed that there is a transition at temperature at 173 MeV and at energy density 0.7 GeV/fm^3[25].

From Fig. 1-3, it is observed that there is a transition at baryonic potential μ_B = 0 for massless quarks. From the theroy of spontaneous breaking of the chiral symmetry in QCD, it is expected. The phase transition is observed at temperature 173 MeV and at energy density 0.7 GeV/fm^3. A sketch of the QCD phase diagram is shown in Fig. 1-4. In this figure without any scale shown, the Y axis represents the temperature T (MeV) and the X axis represents baryochemical potential μ_b. The hadronic phase exists at low temperature and a baryonic chemical potential $\mu_b \approx$ 940 MeV. Protons and neutrons stick together to form nuclei at low energies. The hadronic matter consists of a gas of hadrons at high temperature, close to that at the transition to the quark gluon plasma. In this figure, this transition is shown to be of 1^{st} order. Because of this 1^{st} order transition, there is a finite gap in the first order derivative of the thermodynamic potential. So there should be a cross-over at low μ_b and a first order phase transition at high μ_b. The low temperature hadronic phase and the high temperature partonic phase are connected at the critical point. Experimentally, existence of the critical point is a matter of intese study. Fig. 1-4 also suggests that there is a deconfinement at lower temperatures if the μ_b is higher. If one increases the baryon density of matter to 5-10 times the normal matter density $\rho_0 \approx 0.15$ fm$^{-}3$, then such a transition might occur. Such a state of high density is believed to have existence in the core of neutron stars [27, 28, 29].

1.3 Heavy ions collisions

Collisions between two nuclei at very high energy can give an access to understand the properties of produced matter in this collisions. Several experiments performed at various accelerators like Super Proton Synchroton (SPS) at CERN-Geneva, Relativistic Heavy Ion Collider (RHIC) at Brookhaven National Laboratory and the Large Hadron Collider (LHC) at CERN have been used to understand the matters produced in collisions of heavy nuclei.

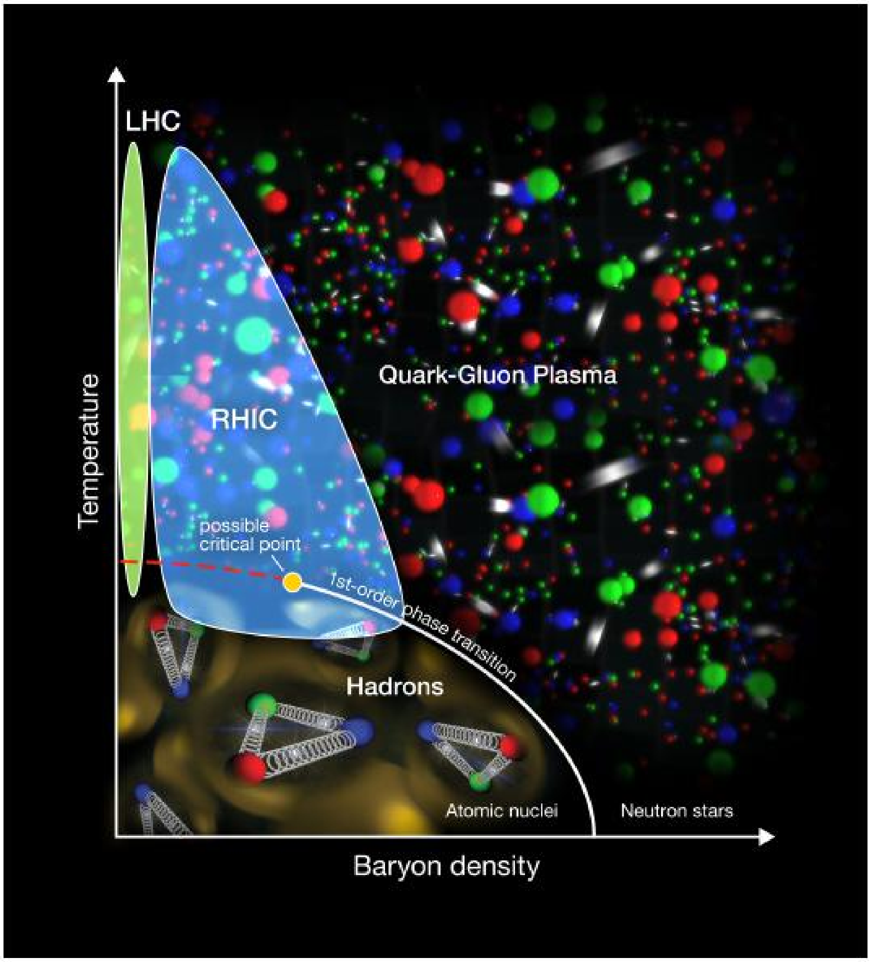

Figure 1-4: (Color online) The phase diagram of QCD . Temperature is along Y axis and baryochemical potential μ_B is along X axis. The critical point might situate at the parton-hadron phase transitions line[26].

Several observables measured as a function of centrality representing the participations of nuclei in the collisions are required to understand the matter produced in several high energy collisions. The impact parameter (b) which is the distance between two colliding nuclei's centre characterises the centrality of each collision. It is not possible to calculate the impact parameter experimentally. The number of particles produced in each collision i.e multiplicity is used to measure centrality. The central collisions are defined with small impact parameters and large numbers of produced particles compared to that at collisions with large impact parameters known as peripheral collisions. In a central collision, most of the nucleons participate in interaction. These nulceons are called participants (N_{part}) and rest of the nucleons which do not participate in interaction are called spectators. There are small number of participants and large number of spectators in peripheral collisions.
When two nuclei collide , there are several stages of evolution as shown in Fig. 1-5. The initial state is actually defined not only by the positions of nucleons but also by the positions of partons before collisions. Positions of nucleons fluctuates from event to event. When the momenta of the final state particles are measured by detectors, the fluctuations in initial position are reflected. After a few fm/c in relativistic heavy-ion collisions, a huge energy gets confined in a very small region and constituents of this region interact with each other to reach a state of local equilibrium. Thermalization time is the time to form this local equilibrium.

There is a considerable fluctuation in the energy density in the produced system and the fluctuation depends on the geometry of the collisions. This generates

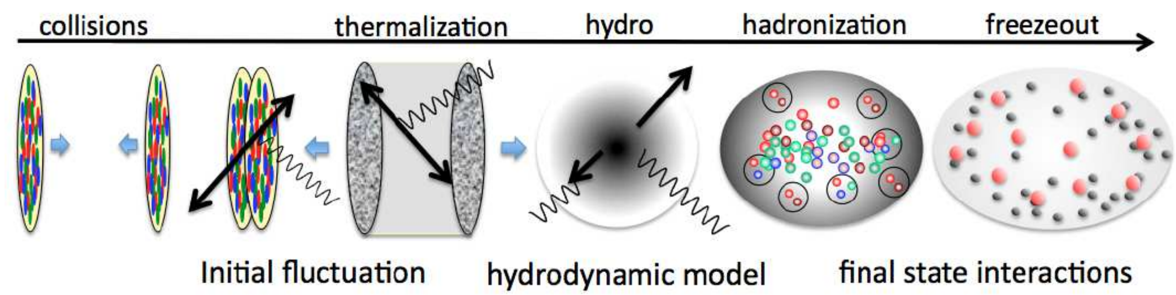

Figure 1-5: (Color online) Schematic view of the evolution of heavy ion collisions [30].

pressure gradients which subsequently create momentum anisotropies among the produced particles. The system then follows hydrodynamic expansion. The energy density and the temperature of the system decrease as the system expands. Expansion of the system depends on the values of shear and bulk viscosities. Initial energy density fluctuation and pressure gradients depend on shear and bulk viscosities. Shear viscosity and bulk viscosity work opposite to each other. Shear viscosity tries to expand the system and more shear viscosity make the final state system more isotropic. Bulk viscosity reduces radial expansion of the system. When temperature decreases below the critical temperature, hadronisation takes place. This hadronisation procedure is described either by parton fragmentation or combination of quarks. The parton frgmentation is performed by parton showering and combination of quarks is done by coalescence. When the number of inelastic collisions is very small, different particle species are produced in a fixed ratio among them. It is called chemical freeze-out. When average distance between the particles are larger than the strong interaction range, there is no elastic collisions between particles. It is called kinetic freeze-out.

1.3.1 Experimental results from high energy heavy ion collisions

There are several measurements performed for undestanding the properties of heavy-ion collisions at SPS, RHIC and LHC. Here we describe three measurements in details :centrality dependence of the charged particle multiplicity, elliptic flow and jet quenching. These measurements shed light to understand the transport properties of the produced system.

Centrality dependence of the charged particle multiplicity

The multiplicity of produced particles in heavy ion collisions is an important property of collisions. The multiplicity depends on collision geometry, the initial parton densities, and the energy density. The particle production in a collision is very sensitive to impact parameter. There are hard (large momentum transfer) and soft (small momentum transfer) processes for particle production. When collision energy increases, partons scatterings through hard processes increase. Charged particle multiplicity density i.e $\frac{dN_{ch}}{d\eta}$ as a function energy $\sqrt{s_{NN}}$ and number of participants is shown in Fig. 1-6. It is oberved from Fig. 1-6 that the value of ($\frac{2}{<N_{part}>} < dN_{ch}/d\eta >$) is increasing with increasing energy and number of participants. The dependence of ($\frac{2}{<N_{part}>} < dN_{ch}/d\eta >$) on $\sqrt{s_{NN}}$ is fitted with a power law as^b and fitting parameters are shown in the left panel of Fig. 1-6. From the right panel of Fig. 1-6, it is observed that the centrality depedence of $< dN_{ch}/d\eta >$ at Pb+Pb collisions with $\sqrt{s_{NN}}$ = 5.02 TeV is very similar to that of

Pb+Pb collisions at $\sqrt{s_{NN}}$ = 2.76 TeV.

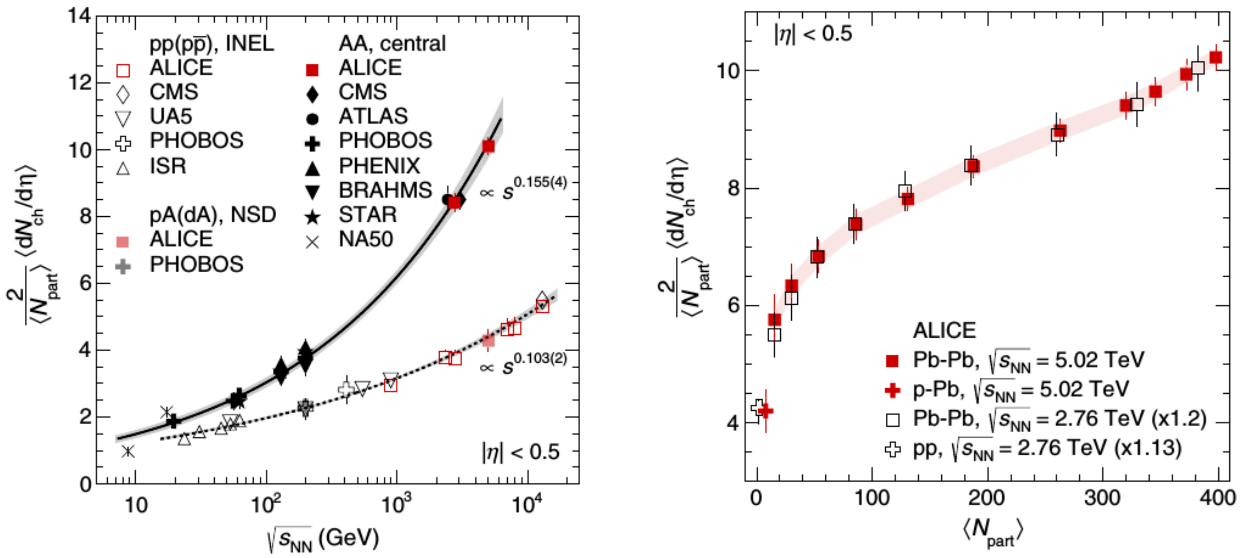

Figure 1-6: (Color online) Values of ($\frac{2}{<N_{part}>} < dN_{ch}/d\eta >$) as a fucntion of $\sqrt{s_{NN}}$ (left panel) and $< N_{part} >$ (right panel) for pp, Pb+Pb and Au+Au collisions are shown [31].

Elliptic flow

Flow is an observable which is used to get experimental information on the transport properties of the produced QGP. Anisotropy in azimuthal direction of produced particles is the clearest experimental signature of collective flow. The second fourier coefficient of azimuthal distribution as shown in Eq. 1.7 is called elliptic flow. Elliptic flow is measured by the anisotropy distribution of the produced particles. Elliptic flow is sensitive to the early stage of the evolution of the system where partonic pressure gradients play a role in anisotropy distribution. This partonic pressure gradient depends on the intial collisions's geometry

[32, 33, 34, 35, 36]. Emission of particles takes place "in" or "out" of the reaction plane which is defined by a plane containing the beam direction and the direction of the impact parameter for noncentral collisions as shown in Fig. 1-7. The

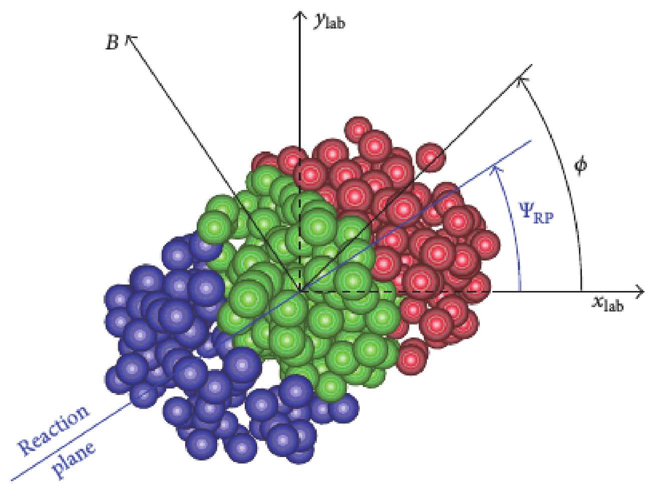

Figure 1-7: (Color online) A picture of transverse plane for a collision . (the left one emerging from and the right one going into the page) [37].

anisotropy distribution of the produced particles in the azimuthal direction can be described using a Fourier distribution described below [38, 39]:

$$E\frac{d^3N}{dp^3} = \frac{1}{2\pi}\frac{d^2N}{p_T dp_t dy}\Big[1 + 2\sum_{n=1}^{\infty} v_n cos\big[n(\varphi - \psi_{RP})\big]\Big] \tag{1.6}$$

From Eq. 1.6, one can get $v_n(p_T, y)$ using the orthogonality properties of cosine function.

$$v_n(p_T, y) =< cos\big[n(\varphi - \psi_{RP})\big] > \tag{1.7}$$

In Eq. 1.6, E is the energy of particle, p the momentum, y the rapidity, p_T the transverse momentum,ψ_{RP} the reaction plane angle, φ the azimuthal angle and the v_n represents the n^{th} order Fourier coefficients. The second harmonic i.e v_2 (from Eq. 1.7) measures relative increase of in-plane particle yield with respect to out-plane particle yield at midrapidity region. Fig. 1-8 shows the p_T differential elliptic flow i.e v_2 as a function of p_T ($0.2 < p_T < 6.0$ GeV/c) for identified particle species measured in Pb+Pb collisions at $\sqrt{s_{NN}}$ = 2.76 TeV [40]. For all particle species, the value of v_2 increases from central to peripheral collisions. It is consistent with the understanding that the initial state eccentricity has higher values for peripheral collisions and the final state anisotropy is controlled by the geometry of collisions. From this figure, it is observed that in low p_T region i.e $p_T \leq 3$ GeV/c, there is a clear mass ordering in v_2 for all centrality bins. It is because of the interplay between radial and elliptic flow. Radial flow creates a depletion at low p_T and this depletion increases with increasing transverse velocity and mass of particle. This depletion is larger for in-plane than in out-of-plane. At a particular p_T, the particles with higher mass have smaller v_2 compared to particles with smaller mass.

The number of constituent quark (n_q) scaling of identified particles's v_2 gives that in early stage of collisions, quark degrees of freedom dominate [41, 42, 43, 44]. In Fig. 1-9, v_2/n_q is plotted as function of p_T/n_q for particles $\pi^{\pm}$, K, p+$\bar{p}$, ϕ, $\Lambda + \bar{\Lambda}$ and $\Xi^- + \Xi^+$ using Pb+Pb collisions data at $\sqrt{s_{NN}}$ = 2.76 TeV.

In ref [31, 46, 47, 48, 49, 50, 51], it is shown that at intermediate p_T range, quark coalescence mechanism dominates. From Fig. 1-9, it is observed that there is a poor scaling for $p_T/n_q < 1$ GeV/c and better scaling for $p_T/n_q > 1$ GeV/c. There

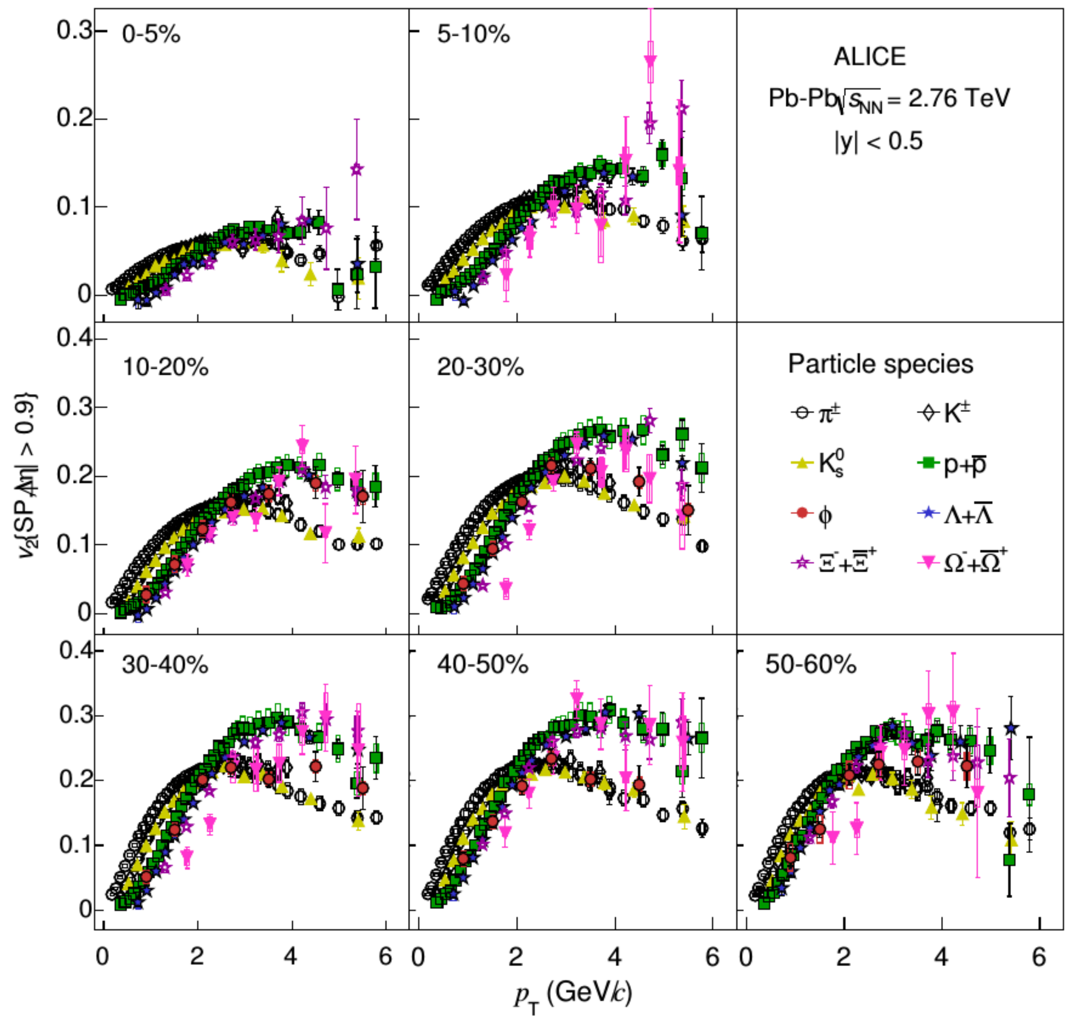

Figure 1-8: (Color online) The p_T differential v_2 for identified different particle species for different centrality collisions of Pb+Pb at $\sqrt{S_{NN}}$ = 2.76 TeV [40].

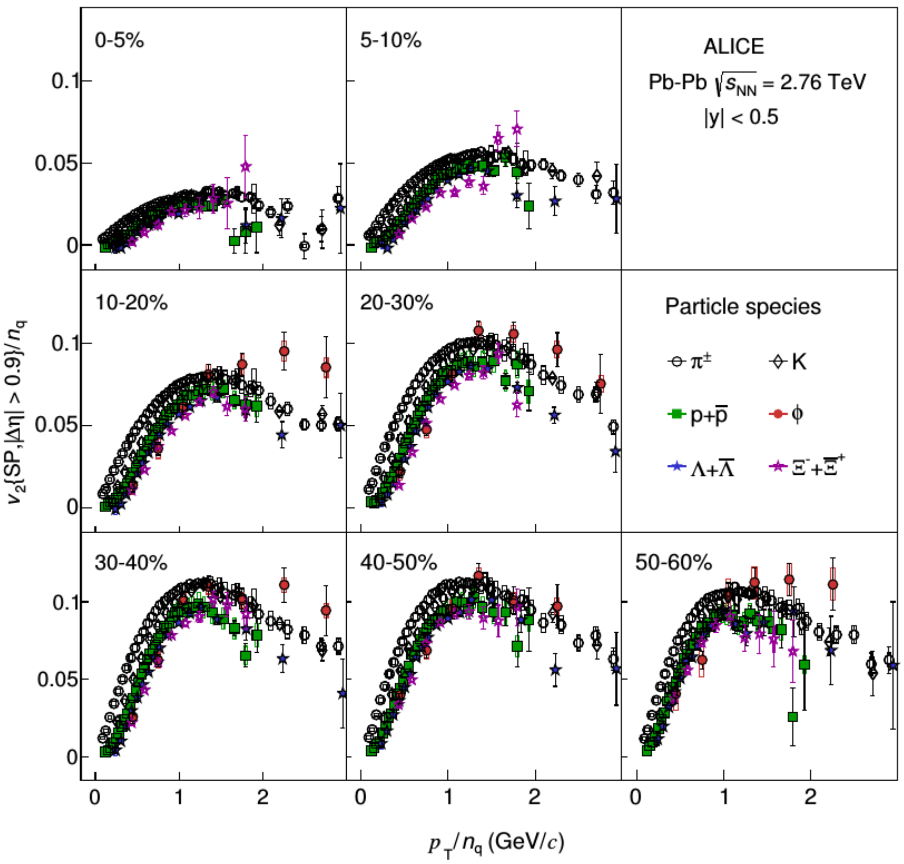

Figure 1-9: (Color online) v_2/n_q plotted as a function of p_T/n_q for $\pi^{\pm}$, K, p+$\bar{p}$, ϕ, $\Lambda + \bar{\Lambda}$ and $\Xi^{-} + \Xi^{+}$ for Pb+Pb collisions at $\sqrt{s_{NN}}$ = 2.76 TeV [40].

is a large error bars for $p_T/n_q > 1$ GeV/c. This result indicates that the scaling is aproximate at all centralities at LHC energy.

Jet quenching

Jet quenching is another phenomenon which reveals the medium properties. The partons loose energy while travelling in the dense QGP medium. The attenuation of partons gives rise to quenching of jets as shown schematically in Fig. 1-10. One can observe jet quenching by observing suppresion in the p_T spectrum of high p_T particles [53, 54, 55, 56, 57, 58]. The nuclear modification factor (R_{AA}) defined as a ratio between the yields of the particle ($d^2N_{ch}^{AA}/d\eta dp_T$) in heavy-ion collisions and the yields of the partilces ($d^2N_{ch}^{pp}/d\eta dp_T$) in pp collisions scaled by the number of nucleon-nucleon collisions ($< N_{coll} >$) is used to calculate the degree of suppresion. The definition of R_{AA} is shown in Eq. 1.8.

$$R_{AA} = \frac{1}{< N_{coll} >} \frac{N_{evt}^{pp}}{N_{evt}^{AA}} \frac{d^2N_{ch}^{AA}/d\eta dp_T}{d^2N_{ch}^{pp}/d\eta dp_T} \tag{1.8}$$

In Eq. 1.8, η represents pseudorapidity defined as $\eta = -\ln\left[\tan(\frac{\theta}{2})\right]$ where θ is the polar angle between the direction of particles and beam axis. Number of events in A+A and pp collisions are represented by N_{evt}^{AA} and N_{evt}^{pp} respectively. $< N_{coll} >$ represents the average number of nucleon-nucleon collisions and it is equal to the product of the inelastic nucleon-nucleon cross section and the nuclear overlap function. $< N_{coll} >$ is determined from montecarlo glauber model [59]. Fig. 1-11 shows R_{AA} in central Pb+Pb collisions as measured by the ALICE compared to the measurements of R_{AA} by STAR and PHENIX experiments at RHIC.

From the figure, it is observed that R_{AA} at LHC at p_T 6-7 GeV/c is smaller than that at RHIC.

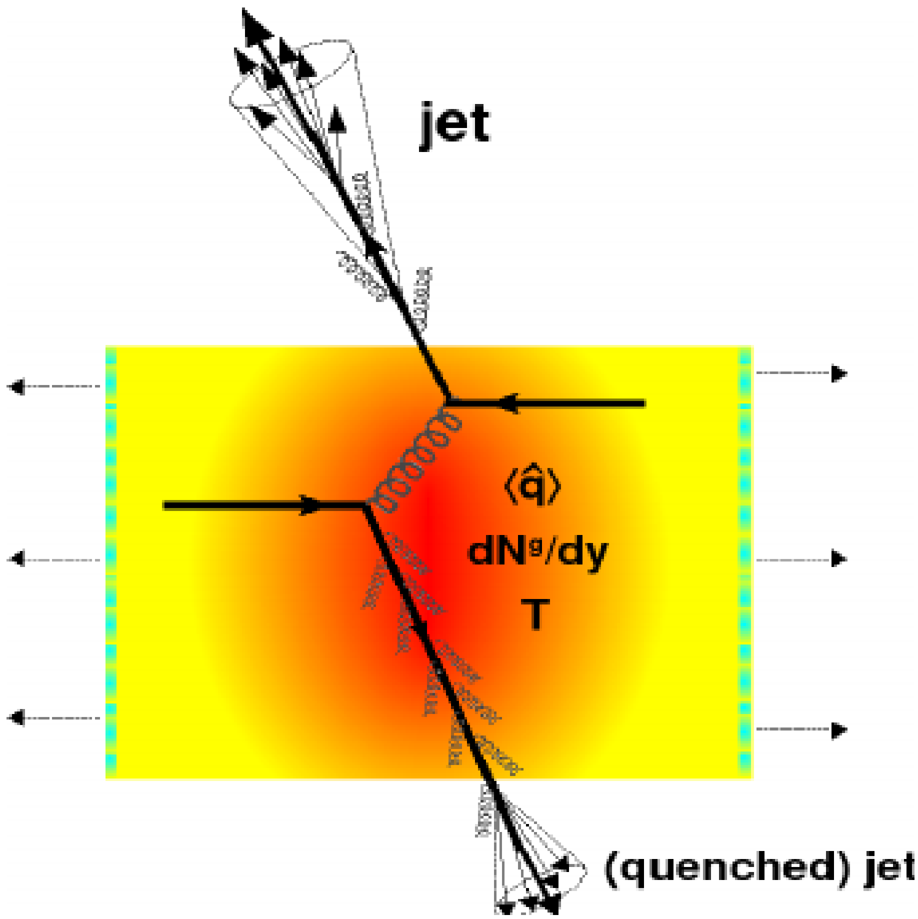

Figure 1-10: (Color online) A hard scattering between two quarks. One quark goes out to vacuum by radiating a few gluons and finally hadronise. Other quark goes through the dense QGP medium. This quark looses energy due to medium-induced gluonstrahlung and finally it fragments into a quenched jet [52].

Data suggests that there is an enhanced energy loss at LHC and therefore a denser medium is created.

Recently ATLAS measured photon tagged jet quenching in QGP [61]. Photons

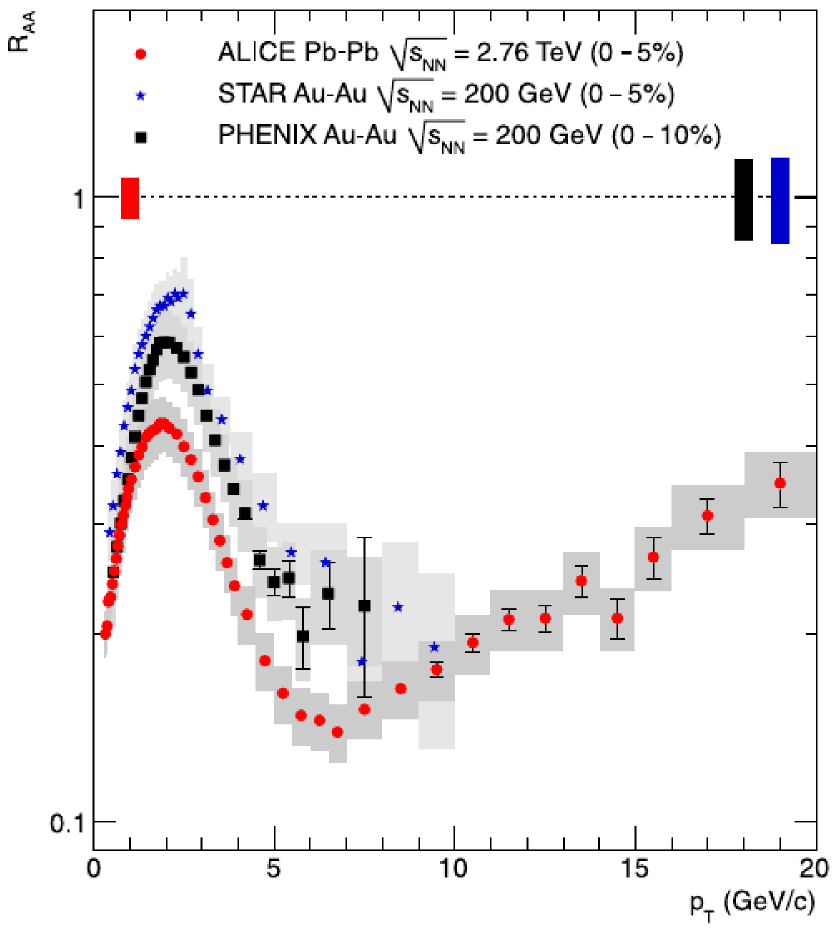

Figure 1-11: (Color online) Comparision of nuclear modification factor in central Pb+Pb collisions at LHC to measurements at STAR and PHENIX at $\sqrt{S_{NN}}$ = 200 GeV. The statistical and systematic errors are shown by error bars and boxes respectively. The vertical bars around R_{AA} = 1 represents p_T independent scaling errors on R_AA [60].

have no color charge. So photons do not interact strongly with medium and rate of photons production are unchanged by the medium [62]. Because of this property of photon, one can probe the direction of parton before loosing energy for interaction with medium. So photon-jet correlation can therefore give light on intial parton transverse momentum dependence of parton energy loss. This result tells that when jets travel through QGP region, its structure is modified.

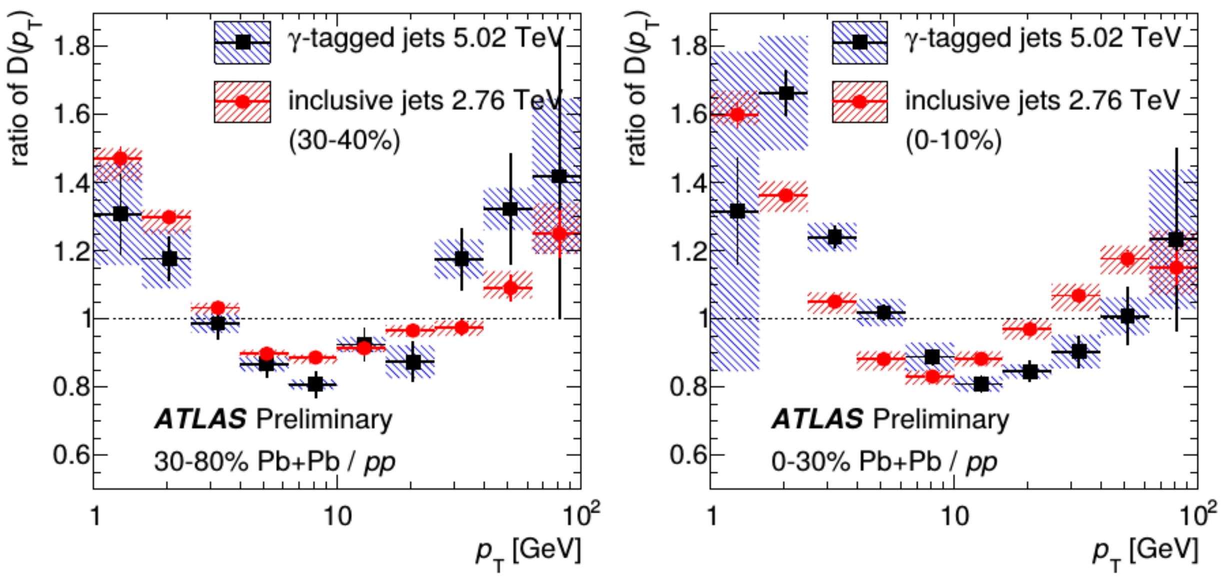

Figure 1-12: (Color online) Ratio of fragmentation function for jets which are azimuthally balanced with high-p_T photon for two centrality 30-80% (left plot) and 0-30% (right plot). Black points are for results with photon-tagged jets and red points show results for inclusive jets [61].

Fig. 1-12 shows ratio of fragmenation function for jets which are azimuthally balanced with high p_T photon for Pb+Pb collisions at $\sqrt{s_{NN}}$ = 5.02 TeV. These ratios are also compared with inclusive jets's results for Pb+Pb collisions at $\sqrt{s_{NN}}$ = 2.76 TeV. It is observed from left panel of Fig. 1-12 that modification pattern for photon-tagged jets is very similar to that observed for inclusive jets in peripheral collisions. In central collision, it is observed that there is a suppresion and enhancement at high p_T and low p_T respectively.

In addition to the measurements of these observables, there are observables related to the measurements of the angular correlation between produced particles. These observables are used as powerful tools to measure properties of created system in high energy heavy-ion collisions. This thesis has main goal to study these observables.

In this thesis, theory of balance function and previous experimental results are shown in chapter 2. In chapter 3, LHC and ALICE experiment are described in details. Chapter 4 presents data analysis and experimental results. Balance function probing chiral magnetic effect is presented in chapter 5. Finally a discussion is given in chapter 6.

Bibliography

[1] LHCb Collaboration, R. Aaij et al.,"Observation of J/ψp Resonances Consistent with Pentaquark States in $\lambda_b^0 \to J/\psi \bar{K} p$ Decays" Phys. Rev. Lett. 115 (2015) 072001.

[2] F. Englert and R. Brout, "Broken symmetry and the mass of gauge vector mesons", Phys. Rev. Lett. 13 (Aug, 1964) 321-323 ,
P. W. Higgs, "Broken symmetries and the masses of gauge bosons",Phys. Rev. Lett. 13 (Oct, 1964) 508-509.

[3] ATLAS Collaboration, G. Aad et al., "Observation of a new particle in the search for the Standard Model Higgs boson with the ATLAS detector at the LHC", Phys. Lett. B716 (2012) 1-29,
CMS Collaboration, S. Chatrchyan et al., "Observation of a new boson at a mass of 125 GeV with the CMS experiment at the LHC", Phys. Lett. B716 (2012) 30-61.

[4] F. Englert, R. Brout, Phys. Rev. Lett. 13 (1964) 321.

[5] P.W. Higgs, Phys. Lett. 12 (1964) 132.

[6] P.W. Higgs, Phys. Rev. Lett. 13 (1964) 508.

[7] G.S. Guralnik, C.R. Hagen, T.W.B. Kibble, Phys. Rev. Lett. 13 (1964) 585.

[8] P.W. Higgs, Phys. Rev. 145 (1966) 1156.

[9] T.W.B. Kibble, Phys. Rev. 155 (1967) 1554.

[10] Richard D. Field, "Application of Perturbative QCD"

[11] K. G. Wilson, Phys.Rev., vol. D10, (1974) pp. 2445-2459

[12] G. 't Hooft, On the Phase Transition Towards Permanent Quark Confinement, Nucl.Phys., vol. B138, (1978), p. 1.

[13] G. 't Hooft, Topology of the Gauge Condition and New Confinement Phases in Non- abelian Gauge Theories, Nucl.Phys., vol. B190, p. 455, 1981.

[14] D. J. Gross and F. Wilczek, Ultraviolet Behavior of Nonabelian Gauge Theories, Phys.Rev.Lett., vol. 30, pp. 1343-1346, 1973.

[15] Siegfried Bethke, Eur. Phys. J. C (2009) 64: 689-703

[16] E. V. Shuryak, "Quantum Chromodynamics and the Theory of Superdense Matter", Phys. Rept. 61 (1980) 71-158.

[17] R. Hagedorn: "Statistical thermodynamics of strong interac- tions at high energies" http://cds.cern.ch/record/346206/files/CM-P00057114.pdf

[18] K. Bardakci and S. Mandelstam: "Analytic Solution of the Linear-Trajectory Bootstrap", Phys. Rev. 184, 1640 (1969) 2.

[19] H. Satz: "The Limits of Hadron Thermodynamics", Fortschr. Phys. 33, 259 (1985) 3.

[20] M. Asakawa and T. Hatsuda: "Thermodynamics and Bulk Properties of QCD Plasma", Nucl. Phys. A 610, 470c (1996) 5,9.

[21] K. Wilson: "Confinement of quarks", Phys. Rev. D 10, 2445 (1974) 620.

[22] Z. Fodor and S.D. Katz: "Lattice determination of the critical point of QCD at finite T and μ ", JHEP 0203, 014 (2002) 24, 25,29, 97, 99.

[23] Ph. de Forcrand and O. Philipsen: "The QCD phase diagram for small densities from imaginary chemical potential", Nucl.Phys. B642,(2002) 290.

[24] C.R. Allton et al.: "The Equation of state for two flavor QCD at nonzero chemical potential", Phys. Rev. D68, 014507 (2003) 97.

[25] F. Karsch. Lattice QCD at High Temperature and Density. Lecture Notes of Physics, vol. (2002) 583. arXiv:hep-lat/0106019.

[26] Relativistic Heavy Ion Collider at the Brookhaven National Laboratory. https://www.bnl.gov/rhic.

[27] S.L. Shapiro and S. Teukolsky: "Black Holes, White Dwarfs and Neutron Stars", Wiley, New York, (1983) 25.

[28] F. Weber: "Pulsars as Astrophysical Laboratories", Institute of Physics Publishing, Bristol (1999).

[29] R. Oechslin, H.T. Janka and A. Marek: "Relativistic neutron star merger simulations with non-zero temperature equations of state I. Variation of binary parameters and equation of state", astro-ph/ 0611047 25.

[30] Chiho Nonaka and Masayuki Asakawa: https://arxiv.org/pdf/1204.4795.pdf

[31] ALICE Collaboration, Phys. Rev. Lett. 116, (2016), 222302

[32] J.Y. Ollitrault, Phys. Rev. D 46,(1992), 229.

[33] STAR Collaboration, Phys. Rev. Lett. 86,(2001), 402.

[34] H. Heiselberg and A.M. Levy, Phys. Rev. C 59, (1999), 2716 .

[35] H. Sorge, Phys.Rev. Lett. 82, (1999), 2048 .

[36] S.A. Voloshin and A.M. Poskanzer, Phys. Lett. B 474,(2000),27.

[37] Gang Wang and Liwen Wen, https://doi.org/10.1155/2017/9240170

[38] S. Voloshin and Y. Zhang, Z.Phys.C70, (1996), 665-672.

[39] A.M. Poskanzer and S.A. Voloshin, Phys. Rev. C 58, (1998), 1671.

[40] ALICE Collaboration: JHEP 06 (2015) 190.

[41] D.Molnar and S.A.Voloshin, Phys. Rev. Lett. 91, (2003),092301.

[42] V. Greco, C.M. Ko and P. Levai, Phys. Rev. C 68, (2003), 034904.

[43] R.J. Fries, B. M ÌĹuller, C. Nonaka and S.A. Bass, Phys. Rev. C 68, (2003), 044902.

[44] R.C. Hwa and C.B. Yang, Phys. Rev. C 70, (2004), 024904.

[45] STAR collaboration, J. Adams et al., Phys. Rev. Lett. 92, (2004),052302.

[46] STAR collaboration, B.I. Abelev et al.Phys. Rev. C 75, (2007), 054906.

[47] STAR collaboration, J. Adams et al., Phys. Rev. C 72, (2005), 014904.

[48] PHENIX collaboration, S.S. Adler et al., Phys. Rev. Lett. 91,(2003), 182301.

[49] PHENIX collaboration, S. Afanasiev et al.,Phys. Rev. Lett. 99,(2007), 052301.

[50] PHENIX collaboration, A. Adare et al.,Phys. Rev. Lett. 98, (2007,)162301.

[51] PHENIX collaboration, A. Adare et al.,Phys. Rev. C 85, (2012),064914.

[52] David Enterria Barbara Betz, Hadron Suppression and Jet Quenching: DOI 10.1007/978-3-642-02286-9_9

[53] ALICE Collaboration: JHEP 30 ,(2014), 013.

[54] ALICE Collaboration: Phys. Rev. Lett. 108,(2012),092301.

[55] C.A. Salgado and U.A. Wiedemann, Phys. Rev. Lett. 93,(2004),042301 .

[56] I. Vitev, S. Wicks and B.W. Zhang, JHEP 0811,(2008),093.

[57] F. Arleo: Eur.Phys. J. C 61: (2009), 603-627.

[58] ALICE Collaboration: Phys. Lett. B 696 (2011) 30-39.

[59] M. Miller, K. Reygers, S. Sanders, P. Steinberg, Annu. Rev. Nucl. Part. Sci. 57,(2007), 205 .

[60] ALICE Collaboration: Phys. Lett. B 696,(2011),30-39.

[61] ATLAS Collaboration, "Measurement of the fragmentation function for photon-tagged jets in $\sqrt{s_{NN}}$ = 5.02 TeV Pb+Pb and pp collisions with the ATLAS detector", ATLAS-CONF-2017-074, http://cds.cern.ch/record/2285812

[62] F. Arleo, K. J. Eskola, H. Paukkunen and C. A. Salgado, JHEP 04, (2011), 055.

Chapter 2

Balance function

In high energy heavy ion collisions, a state of matter composed of quarks and gluons has been hypothesized to exist. Charge dependent correlation is one of tools used to study the properties of the created matter. The correlation between charges and associated anticharges are studied with the use of balance function (BF) [1]. In this thesis, we have described the measurement of BF in Pb+Pb collisions at the LHC energy by the ALICE experiment in detail. In this chapter, therefore, a detailed account on the theory and the previous measurements of BF have been given. Description of balance function is given in section 2.1. Theoretical explanations and experimental results of balance functions are given in section 2.2 and 2.3 respectively.

2.1 The Balance function observable

Dynamical evolutions of quarks and gluons are responsible for production of particles in high energy heavy ion collisions. The produced particles from the collisions follow charge conservation means, if there is a positively charged particle produced, there should be a negatively charged particle at the same space-time point. The BF measures the correlation between this pair and gives a hint of produced QGP medium's life time. In a collision, a signal which pinpoints the time of quark's production would give an important information of QGP. Balance function has a sense of probing production time of quarks. Charge-anticharge pairs are created at the same space-time point. These pairs are correlated in rapidity and azimuthal angle due to collective expansion of the system. If pairs are created earlier, the interaction time with the medium is greater than the pairs which are created later. The initial correlation between constituent quarks of a pair created later is therefore not destroyed. The pairs that are created earlier can separate from each of them in rapidity even further with evolution. Higher initial temperature and more diffusive interactions with another particles make this separation. The separation between charges are governed by the sum of separation of quarks before hadronisation and the separation of particles after hadronisation. The separtion of particles after hadronisation is mostly due to hadronic rescattering. Fig. 2-1 shows a pair of balancing partner created at the same space-time point. Here balancing partner is taken as s quark and its anti-quark. In this diagram, system expands horizontally with a rate that decreases with time. The balancing partners created at 1 fm/c is called as early stage production and that at 8 fm/c called as late stage production. It is seen that this early stage balancing partners are separated further in rapidity than those of late stage balancing partners. These balancing partners subsequently combine with some quarks and hadrons are formed. Now these hadrons can further separate in coordinate and momentum space as a result of interaction between them.

Hence, one can determine the QGP medium's life time by knowing the time when charges are produced. Their subsequent interaction with the medium through collective velocity and finally the hadronisation are the effect of the hadronic rescattering.

The balance function observable is based on the princple of local charge conservation. Correlation between these charges that are produced in pairs is quantified by the balance function in space-time. Now the widths of the balance functions measure this separation of these charges. If the hadron pairs are created at a later stage, width is expected to be narrower and wider compared to the case of pairs that are created early. The balance functions are similar to observables which were used to describe hadronisation in jets created in $p\bar{p}$ or e^+e^- collisions [3, 4]. Let's consider, there is a particle in the momentum bin p_1. The balance function is a conditional probability of observing this particle with respect to a particle of opposite charge in the momentum separation bin p_2. So balance function is defined as,

$$B(p_2|p_1) = \frac{1}{2}\Bigg\{\rho(b, p_2|a, p_1) - \rho(b, p_2|b, p_1) + \rho(a, p_2|b, p_1) - \rho(a, p_2|a, p_1)\Bigg\} \quad (2.1)$$

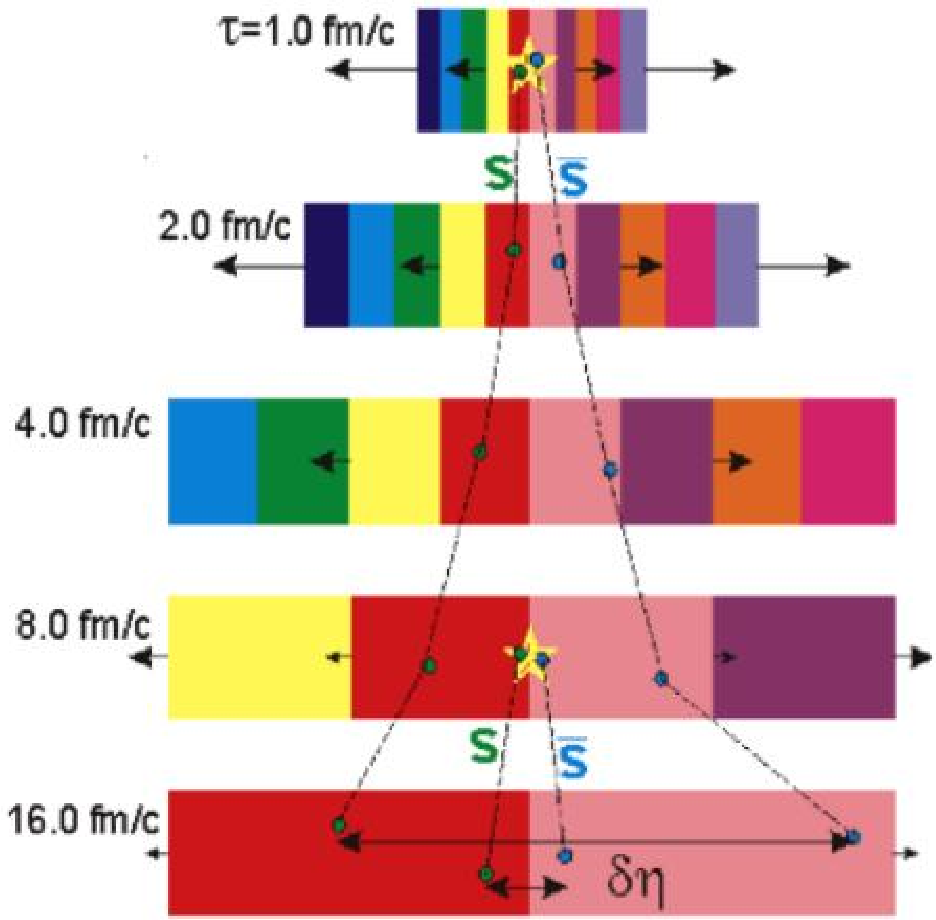

Figure 2-1: (Color online) Balancing partners produced at 1 fm/c and 8 fm/c respectively. Separtion is larger in early produced pair than late produced pair [2].

Here $\rho(b, p_2|a, p_1)$ is a conditional probability of observing a particle *b* in bin p_2 with respect to a particle *a* in bin p_1. Here *a* is taken as a trigger particle and *b* as a associated particle. Particles *a* and *b* can be different types of particles with different charges. In this work, *a* refers to positively charged particle and *b* refers to negatively charged particle. The conditional probability $\rho(b, p_2|a, p_1)$ is calculated by counting the number of pairs i.e $N(b, p_2|a, p_1)$ and dividing by the number of trigger particles i.e $N(a, p_1)$. Here binning in p_1 has been measured using maximum and minimum cuts in p_1. Binning in p_2 refers to relative separation between rapidity and azimuthal angle of particles *a* and *b*. So the conditional probability would be a function of relative rapidity ($\Delta\eta/\Delta y$) or relative azimuthal angle ($\Delta\varphi$) and it is defined as

$$\rho(b, p_2|a, p_1) = \frac{N(b, p_2|a, p_1)}{N(a, p_1)} = C_{ab}(\Delta\eta, \Delta\varphi) \tag{2.2}$$

where $\Delta\eta = \eta_a - \eta_b$ and $\Delta\varphi = \varphi_a - \varphi_b$. Each term in Eq. 2.1 is calculated from each event and the resulting values are averaged over all events. We can write Eq. 2.1 as an equation

$$B(\Delta\eta, \Delta\varphi) = \frac{1}{2}\Bigg\{C_{ab}(\Delta\eta, \Delta\varphi) - C_{bb}(\Delta\eta, \Delta\varphi) + C_{ba}(\Delta\eta, \Delta\varphi) - C_{aa}(\Delta\eta, \Delta\varphi)\Bigg\} \tag{2.3}$$

Let's consider M_a and M_b are the average multiplicities of partilce type *a* and *b* respectively. If all particles with positive/negative charges conserve globally in charge, balance function should be normalized to 1.

$$\sum_{p_2} B(p_2|p_1) = \frac{1}{2}\left\{\frac{{}^{M_b}C_1 M_a}{M_a} - \frac{{}^{M_b-1}C_1 M_b}{M_b} + \frac{{}^{M_a}C_1 M_b}{M_b} - \frac{{}^{M_a-1}C_1 M_a}{M_a}\right\}$$
$$= \frac{1}{2}\left\{M_b - (M_b - 1) + M_a - (M_a - 1)\right\} = 1 \quad (2.4)$$

When acceptance effects, correction in detector and tracking in-efficiency are included, balance function gives a fractional value. Main contributing terms of balance function are first two terms in Eq. 2.3 and these terms are used in several analysis of $e^+e^- \rightarrow$ jets. Last two terms in Eq. 2.3 are kept to retain normalization properties for the case where nonzero net charge exist i.e M_a-$M_b \neq 0$ [1].

2.2 Theory of Balance Function

When system expands with time , temperature decreases. Then the hadronisation starts and finally free hadrons are formed. The width of the balance function reflects the effect of all these stages. Effect of collective flow, freeze-out temperature, resonance decays are keys to affect the width of a balance function.

In ref [1], it is shown that the balance function width gives information about hadronisation time of the produced system. In this paper, Bjorken boost invariant parametrization [5] of an expanding source along the z axis is used. Collective velocity of the expanding source is proportinal to $\frac{z}{t}$ and all intrinsic variable used for describing the system are function of the proper time τ ($\sqrt{t^2 - z^2}$). The width of the balance function of particles with mass m generated from the same space time point following a thermal distribution (Maxwell Boltzmann distribution) at temperature T is given by,

$$\sigma_y = \sqrt{\frac{2T}{m}} \tag{2.5}$$

Heavier mass particles are therefore characterized by narrower distribution of balance function. Fig. 2-2 shows the balance function distribution of pions and protons for two temperatures i.e 165 MeV and 225 MeV. It is seen that the BF of massive particles is highly sensitive to temperature. So the narrower distribution of balance function of a particular massive particle indicates that particles are produced at lower temperature and thus at a latter time in system evolution of high energy heavy ion collisions.

Diffusion affects the balance functions. Diffusion equation in Bjorken coordinates (τ, η) is

$$\frac{\partial}{\partial \tau} f(\tau, \eta) = -\frac{\beta}{\tau} \frac{\partial^2}{\partial \eta^2} f(\tau, \eta) \tag{2.6}$$

where *f* is a probability of finding a particle at a position η at time τ. β is a constant. Here initial condition is at τ_0 , $\eta = 0$. The solution of Eq. 2.6 is a Gaussian distribution with variance $\sigma_\eta^2 = 2\beta \ln(\tau/\tau_0)$. The width of balance function is now a combination of the thermal width (σ_{therm}) and width due to diffusion.

$$\sigma_y^2 = \sigma_{therm}^2 + 4\beta \ln(\tau/\tau_0) \tag{2.7}$$

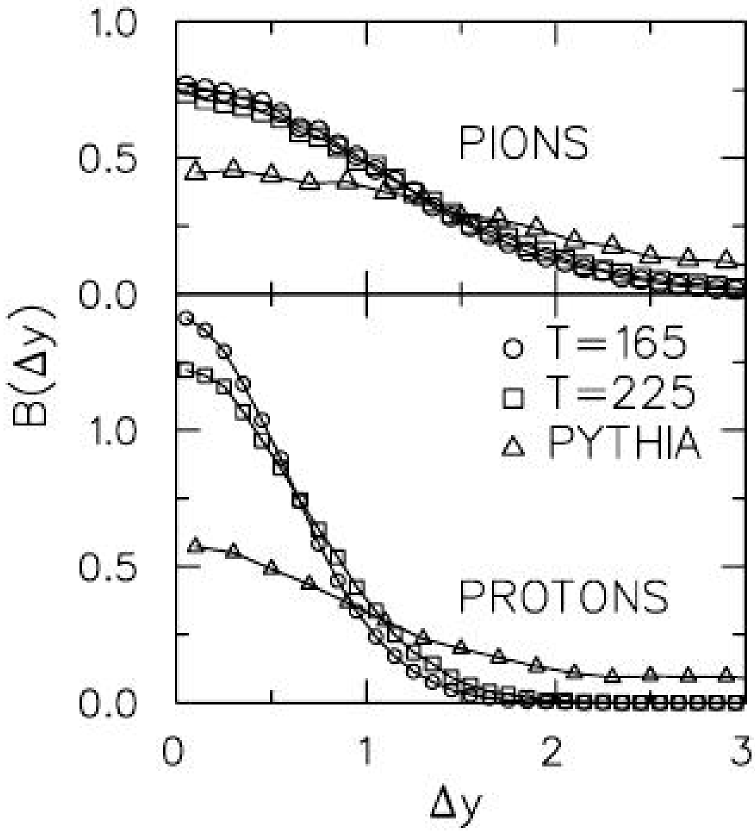

Figure 2-2: (Color online) Balance function of pions and proton for two temperature 225 and 165 MeV. Heavier particles with lower temperature are strongly correlated in rapidity. Balance function distribution of pions and protons are compared with PYTHIA simulation result. Balance function from PYTHIA has wider distribution with respect to thermally generated balance function [1].

The width from the thermal distribution i.e σ_{therm} decreases with time (temperature decreases). If production happens at early stage , $\ln(\tau/\tau_0)$ has a large value and it makes balance function significantly broader. If production happens late, diffusion is negligible. So balance function width depends only on thermal width.

In ref [7], it is shown that balance function could measure transverse flow at the freeze-out temperature. Balance function of pions $\&$ protons have been calculated using thermal models with varying freeze-out temperature and transverse flow velocities. Balance function of pions are constructed for resonance and nonresonant contribution for the production of a pair of opposite charges. Resonance contribution is governed by the decays of neutral hadronic resonances with a pion pair in the final state. Nonresonant contribution is determined by the emission of a pair of charged particles with opposite charge from a local thermal source. These charged particles get momentum from its thermal distribution and are boosted by the collective flow velocity of the source. Two thermal models, the single freeze-out model [8] and the boost invariant blast-wave model [9] are used to study the effect of transverse velocity and freeze-out temperature on pion balance function. Here freeze-out temperature T_f = 165 MeV and moderate transverse velocity $< \beta >$ = 0.5 are used for the single freeze-out model. The transverse velocity $< \beta >$ = 0.6 and freeze-out temperature T_f = 90 MeV have been used for blast-wave model.

Fig. 2-3 shows narrower balance function for lower freeze-out temperature and higher transverse flow velocity. The increase in temperature and lower transverse flow make azimuthal balance function broader. The width of the azimuthal

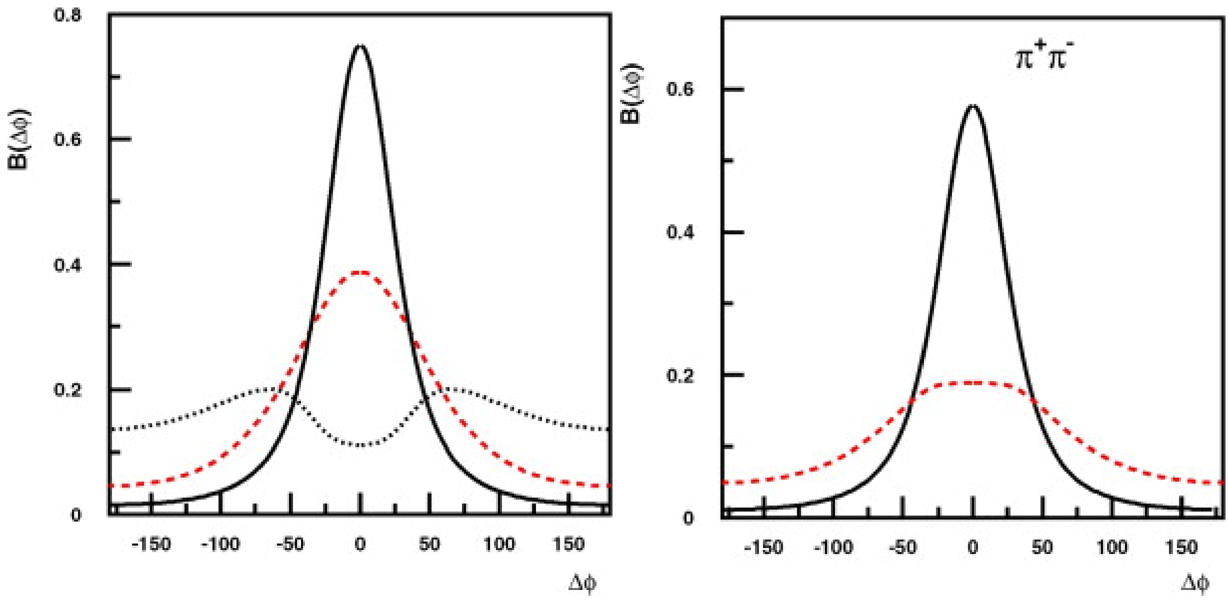

Figure 2-3: (Color online) Left plot: Pion's balance function for two different freeze-out conditions: T_f = 165 MeV , average transverse velocity <β> = 0.5 and T_f = 90 MeV , <β> = 0.6. Dashed line is for nonresonant pions and dotted line is for pions from decay of ρ_0 resonance at T_f=165 MeV and <β> = 0.5. Solid line is for nonresonant pions at T_f = 90 MeV and <β> = 0.6. Right plot: The correlation between the pions is given by a weighed [6] sum of the two mechanisms i.e non-resonant pions and decay products of resonances for T_f = 165 MeV (dashed line) and by nonresonant pion pairs for the freeze-out at 90 MeV (solid line) [7].

balance function can therefore be applied to determine the freeze-out parameters as shown in Fig. 2-3.

In ref [10], balance function is measured as a function of the invariant relative momentum Q_{inv}. The balance function as a function of Q_{inv} is analysed to eliminate the sensitivity to collective flow while the collective flow affects the spectra, it does not affect the invariant momentum differences if pairs of particles are produced from same space-time point. Left panel of Fig. 2-4 shows pion balance function with (circles) and without (square) distortion as a function of Q_{inv}. Right panel shows balance function as a function of Δy. Here distortion is basically interpair interaction of balancing charges with other charged particles. It is observed that distortion effect in balance funtion as function of Δy is less compared to Q_{inv} balance function.

Balance function as obtained in case of the quark coalescence model is described in ref [11]. First, Neutral clusters are formed using partons. Each cluster decays into quark-antiquark pairs and gluons (i.e $u\bar{u}$ or $d\bar{d}$). Positive, negative and neutral pions are formed by recombination of quarks and anti-quarks. The rest of gluons form a new cluster and this procedure continues until all partons are converted into hadrons. There is an observed reduction of the width of the balance function measured in pseudorapidity for central collisions as shown in Fig. 2-5.

Balance function of charged particles and baryons are measured using the coalescence model. It is shown in ref [12]. The decay of isotropic and uncorrelated

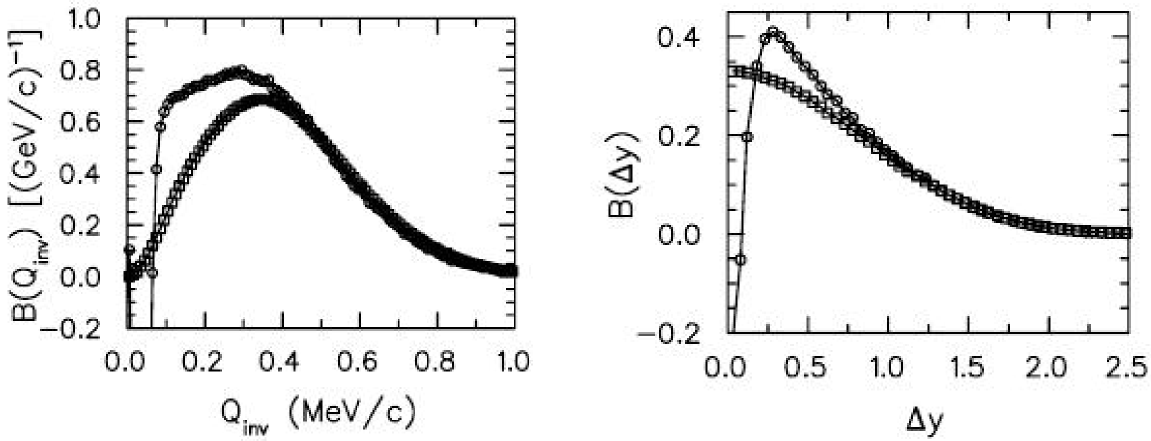

Figure 2-4: (Color online) Pion balance function with (circles) and without (squares) distortion (it is coming from interpair interaction) from blast-wave model are shown in left plot. Blast-wave model has a breakup temperature 120 MeV, a maximum transverse velocity of 0.7c and spread σ_η = 0. The balance function without distortion was scaled by 70% to account for balancing pairs by other species. These balance functions are filtered by STAR acceptance. Balance function as a function of relative rapidity (Δy) with and without distortion are shown in right plot. There is a less distortion effect in Δy. [10]

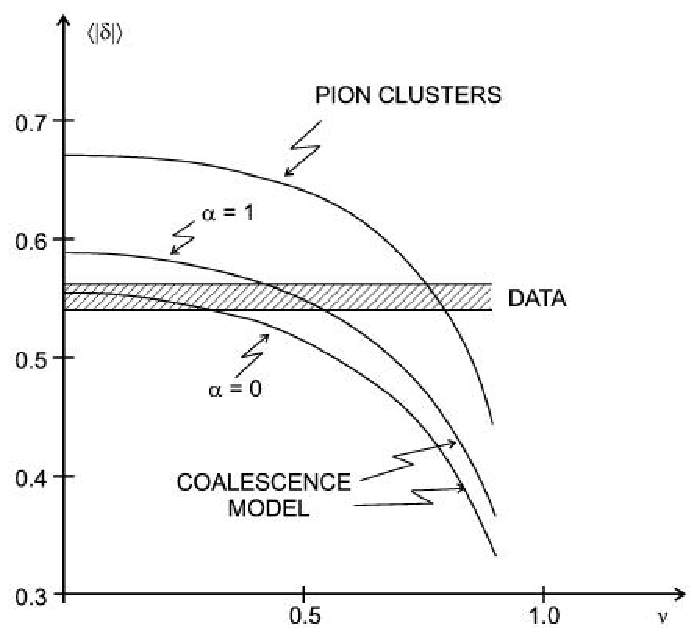

Figure 2-5: (Color online) The width of the balance function i.e. $<|\delta|>$ is plotted versus transverse velocity v. The width of balance function decreases when transeverse velocity of clusters increase. The quantitative agreement with data is gained when transverse velocity of clusters is nearly 0.8c. [13]

cluster is used to explain the width of balance function. The width of meson's balance function distribution of the two independent varibale is decreased by a factor $\frac{1}{\sqrt{2}}$ with respect to the width of individual distribution [13]. The width of baryon's balance function is reduced by a factor $\frac{1}{\sqrt{3}}$. So the baryon balance function width with respect to the charged balance function is reduced by $\frac{\frac{1}{\sqrt{3}}}{\frac{1}{\sqrt{2}}} = \sqrt{\frac{2}{3}} = 0.8164$. So baryon balance function is smaller by a factor of 0.8 with respect to charge balance function. This prediction is confirmed by data. This result shows that baryon balance functions could probe insight in the coalescence model of hadronisation.

In ref [14], balance function is studied using microscopic hadronic models (RQMD , HIJING/GROMIT) and thermal model (Blast-wave). The results from the microscopic models are contrary to recently balance function results published from the STAR Collaboration. The thermal model with temperature 120 MeV and transverse collective velocity 0.7c moreover reproduces the experimental results. By decreasing break up temperature and increasing collective flow , one should be able to explain pion spectra. Balance function of these pions is more narrower than that measured experimentally. So a significant longitudinal size is needed for charge conservation in thermal model. Balance function using multidimensional analysis in the relative momenta of the pions is studied to clarify this ambiguity. The width of the balance function for relative momenta Q_{out}, Q_{side} and Q_{long} [15] should be same if there is delayed charge production.

In ref [16], it is shown that quarks are produced in two waves. The first wave is during the first fm/c of the high energy heavy ion collision. At this time, gluons thermalize into QGP. A second wave happens at hadronisation where time is 5-10 fm/c. Quark-antiquark pairs created in first wave are separated strongly in coordinate space. Pairs created in second wave are separated less in cooridnate space. It is because of less time for separation. Temperature in final state and collective velocity are used as parameters for blast-wave model. The balancing charges separated in coordinate space in the initial conditions of QGP is ruled by $\sigma_{(qgp)}$ parameter. $\frac{\sigma_{(had)}}{\sigma_{(qgp)}}$ is used as an another parameter where $\sigma_{(had)}$ is the spread of balancing charges produced during or after hadronisation. The study of identified particles's balance function is motivated by two wave model. Fig. 2-6 shows balance function distribution of kaons for two contribution 1. Hadronic contribution 2. QGP contribution. Triangles represent hadronisation component and squares represent QGP contribution. The hadronization is the smallest component, since few strange quarks are produced during this stage. Number of strange quarks produced during hadronisation is very small. The hadronisation contribution in $K^{+}K^{-}$ correlation is small (upper plot). If there is half strangness in the QGP, hadronisation contribution would be larger and balance function distribution is narrow.

In conclusion, the author states that it is possible to get information about the system's chemical evolution and further constrain the input parameters of the models which are used to describe high energy heavy-ion collisions. These correlations are used to understand the properties of QGP matter produced in ALICE at the LHC.

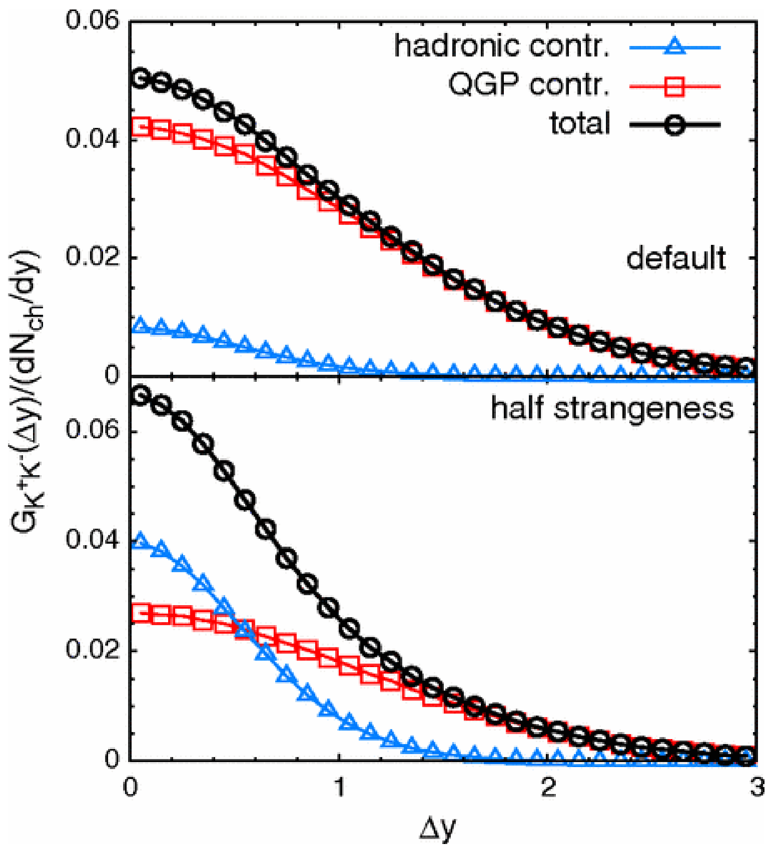

Figure 2-6: (Color online) The contribution from hadronisation in balance function of K^+K^- is small. It is shown in the upper panel. If there is half strangness in the QGP, hadronisation contribution would be larger and balance function distribution is narrow. [17]

2.3 Experimental results of balance function

First result on balance function of all charged particles and identified charged pions have been measured by the STAR experiment with Au-Au collisions at $\sqrt{s_{NN}}$ = 130 GeV. It is observed that there is a narrowing of the balance function distribution in $\Delta\eta$ and Δy with centrality for all charged particles and identified pions respectively as shown in Fig. 2-7.

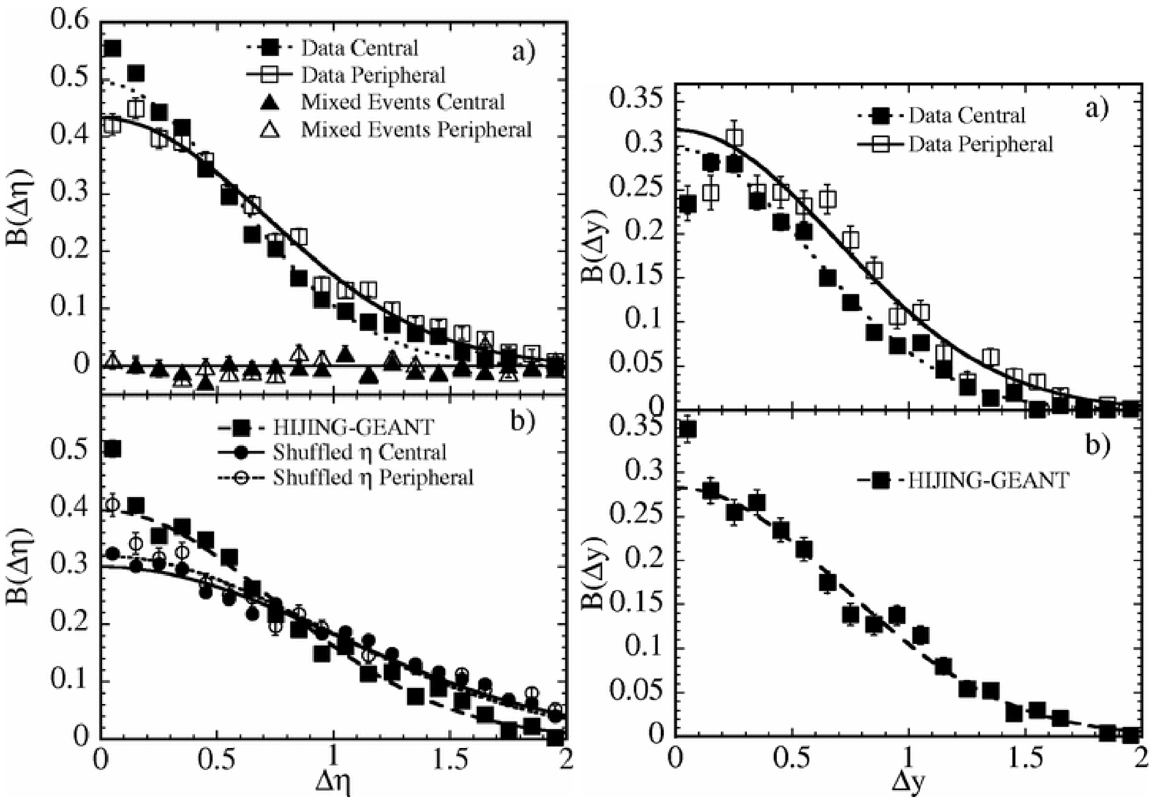

Figure 2-7: (Color online) The balance function distribution of all charged partilces and identifed pions for central and peripheral collisions between two Au nuclei at $\sqrt{s_{NN}}$ = 130 GeV are shown in left and right plot respectively [18].

There is a dip near Δy = 0 in balance function distribution of identified charged pions. The origin of this dip can be understood as the resultant effect of coulomb interactions and Bose-Einstein correlations between identified charged pions as shown in ref [19]. Study of the system size dependence of balance function is performed by the NA49 collaboration as shown in ref [20].

In this paper BF have been measured in p+p, C+C, Si+Si and Pb+Pb collisions at a centre of mass energy of $\sqrt{S_{NN}}$ = 17.2 GeV. Fig. 2-8 and Fig. 2-9 show that the widths of balance function decreases as system size increases. The width of the balance function for Pb+Pb collisions decreases with increasing centrality as shown in Fig. 2-9. The narrowing trend of the balance function from peripheral to central in Pb+Pb collisions at SPS and in Au+Au collisions at RHIC gives a hint about a delayed hadronisation of the produced QGP matter.

In ref [21], the balance function of identified pions and kaons are studied for Au+Au, *d*+Au and p+p collisions at $\sqrt{s_{NN}}$ = 200 GeV. The results of balance function distribution for identified pions and kaons for Au+Au collisions for nine centrality bins are shown in Fig. 2-10 and 2-11. The balance function distribution for identified pions gets narrower in more central collisions. The balance function calculated from mixed events coincides with zero for all centrality bins. The balance function of kaons shows very little dependence on centrality. This almost no dependence on centrality may hint that the strangeness production is dominated in the early stage than in the late stage of hadronisation. Fig. 2-12 shows the balance function distribution as a function of q_{inv} for identified charged pions in nine centrality bins for Au+Au collisions at $\sqrt{s_{NN}}$ = 200 GeV. There is a peak for each centrality bin corresponding to the charged pions created from de-

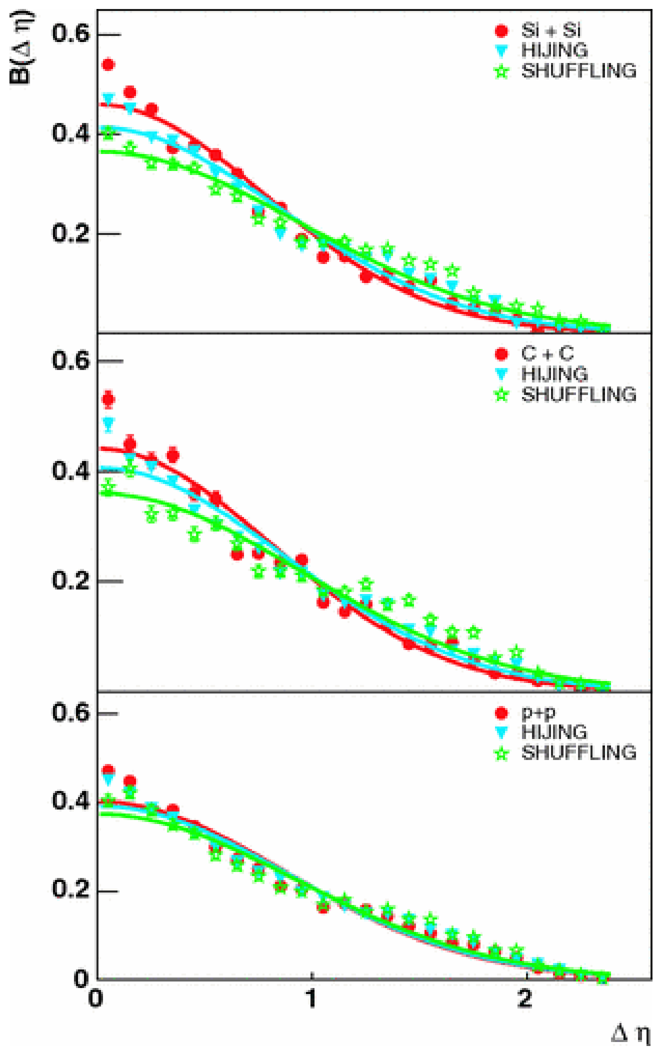

Figure 2-8: (Color online) Balance function distribution as a function of $\Delta\eta$ for Si+Si, C+C and p+p collisions with real, shuffled and HIJING events are shown. The BF from HIJING event generator is independent of centrality and system size of nuclei. The distribution is wider than BF from real data. It is also observed that BF distribution is more narrower for Si+Si collisions than C+C and pp collisions [20].

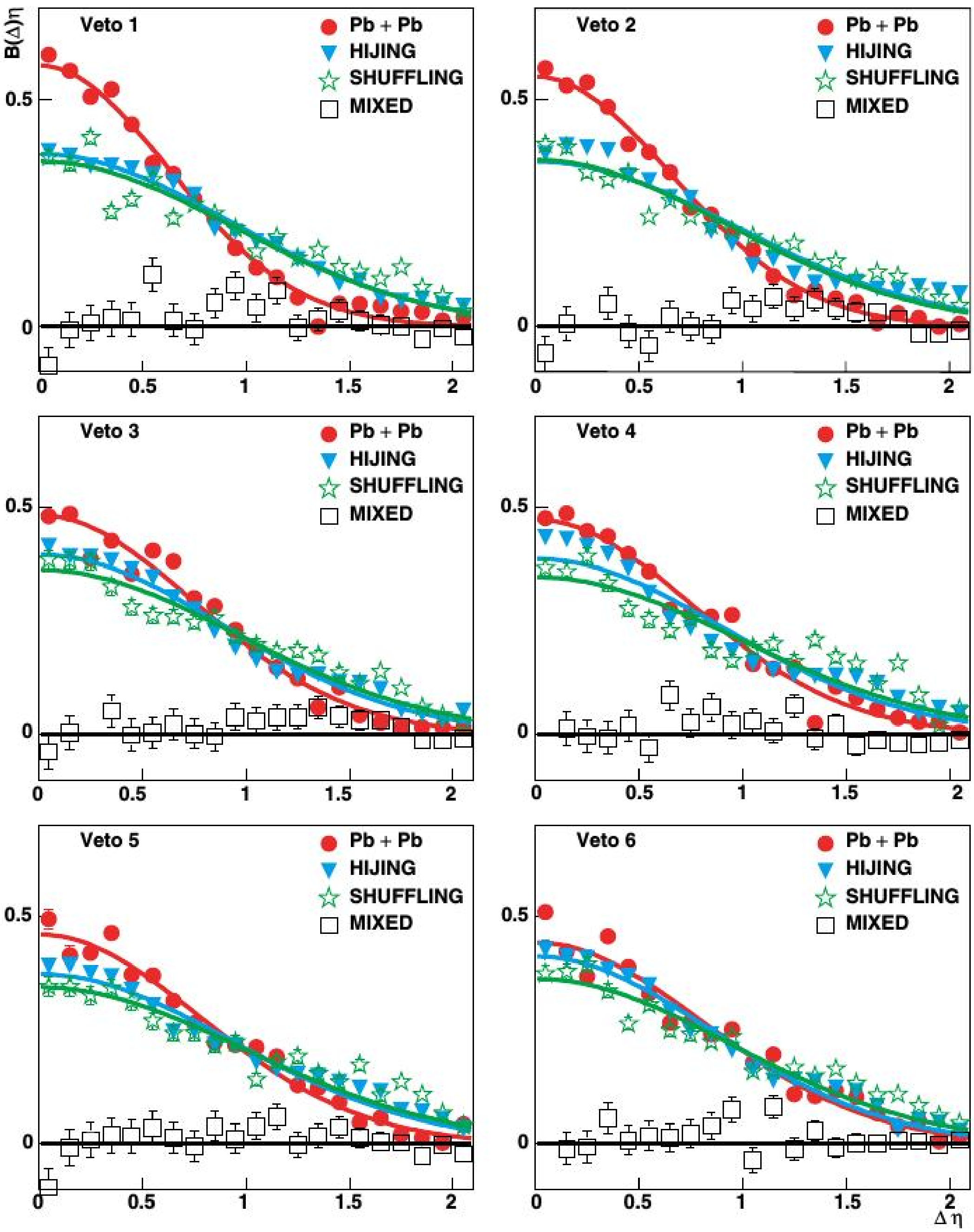

Figure 2-9: (Color online) The balance function distribution of Pb+Pb collisions with different centrality are shown. Real data points are shown with darked circle and marker [20].

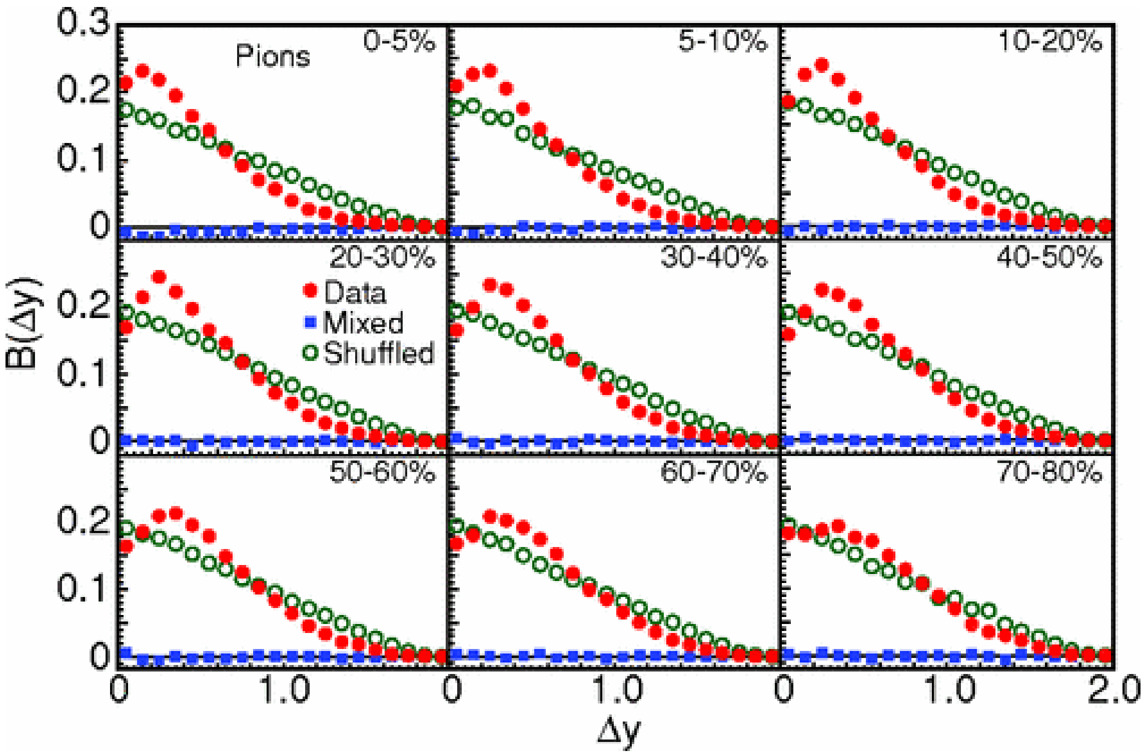

Figure 2-10: (Color online) The balance function distribution as a function of Δy for identified charged pions produced in Au+Au collisions at $\sqrt{s_{NN}}$ = 200 GeV. Pion balance function get narrower in central collisions with respect to peripheral collisions [21].

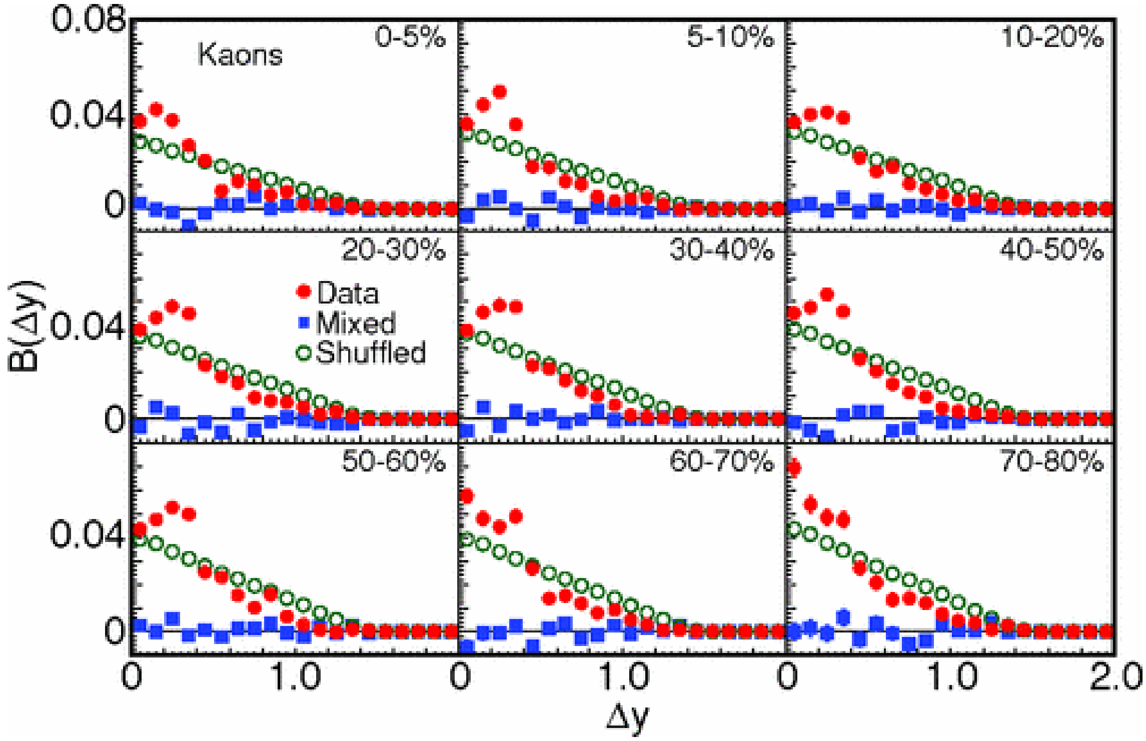

Figure 2-11: (Color online) The balance function distribution as a function of Δy for identified charged kaons produced in Au+Au collisions at $\sqrt{s_{NN}}$ = 200 GeV. There is a very little dependence on centrality in kaon balance function distribution [21].

cay of $K_S^0 \rightarrow \pi^+ + \pi^-$. Similarly the balance function distribution for identified charged kaons is shown in Fig. 2-13. In this figure, there is a peak corresponding to charged kaon pairs deriving from $\varphi \rightarrow K^+ + K^-$. The width of the balance function in terms of q_{inv} for both pions and kaons decreases with increasing centrality. The reason of this narrowing may be explained by the evolution of kinetic freeze-out temperature with centrality.

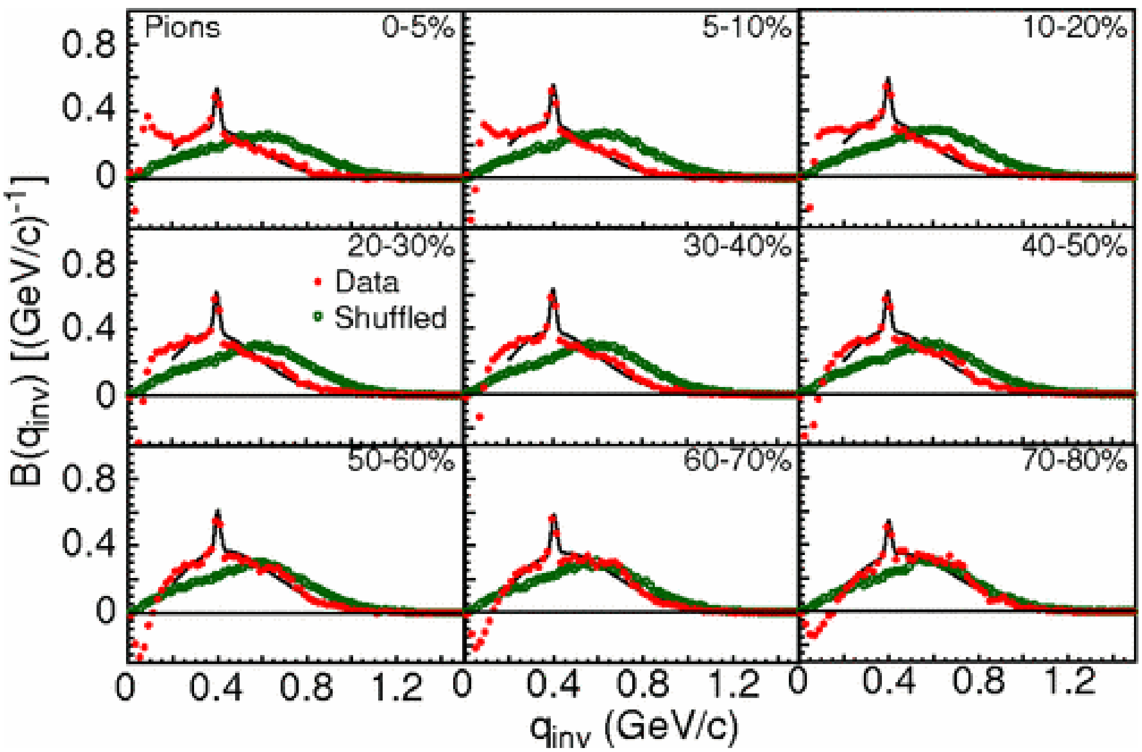

Figure 2-12: (Color online) The balance function distribution as a function of q_{inv} for identified charged pions produced in Au+Au collisions at $\sqrt{s_{NN}}$ = 200 GeV in nine centrality bins. Contribution from a thermal distribution and K_S^0 decay is represented by curves [21].

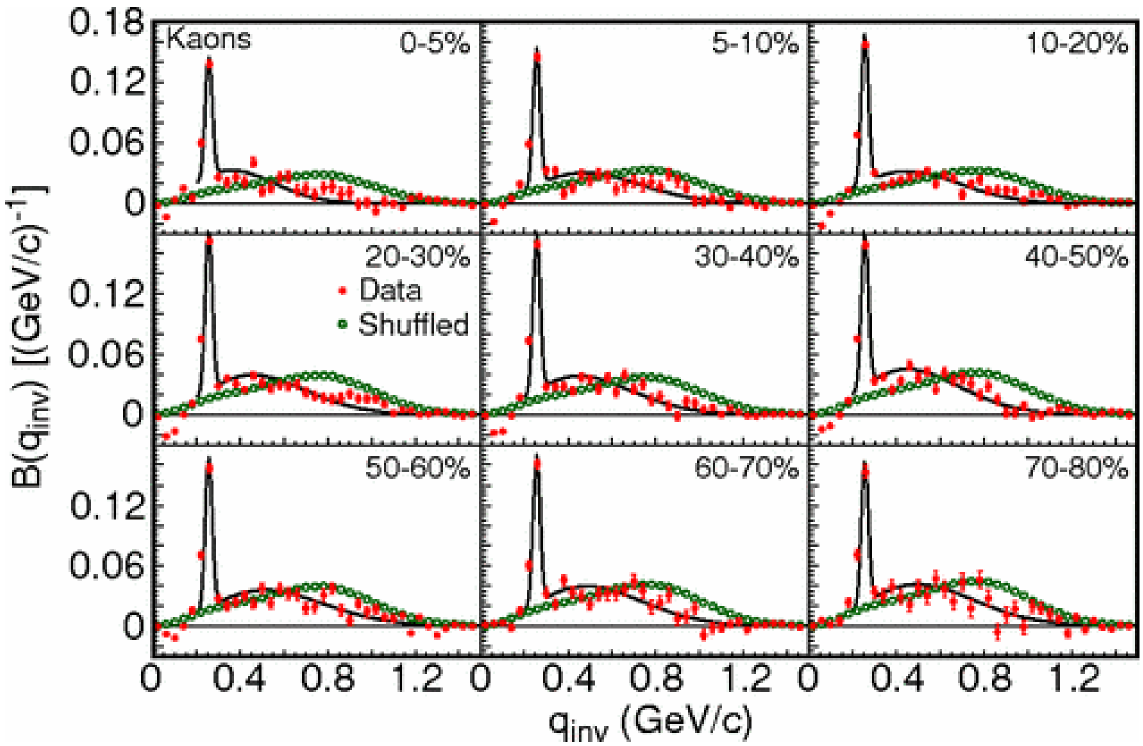

Figure 2-13: (Color online) The balance function distribution as a function of q_{inv} for identified charged kaons produced in Au+Au collisions at $\sqrt{s_{NN}}$ = 200 GeV in nine centrality bins. Contribution from a thermal distribution and φ decay is represented by curves [21].

Bibliography

[1] S.A Bass, P.Danielewicz and Scott Pratt, Phys.Rev.Lett 85, (2000),2689.

[2] www.star.bnl.gov/central/physics/results/result.php?res = 17cat = ebye

[3] D.Drijard et al., Nucl. Phys. B155,(1979), 269 ; D.Drijard et al., Nucl. Phys. B166,(1980),233 ; I.V. Ajinenko et al., Z.Phys. C 43,(1989), 37 .

[4] R.Brandelik et al., Phys.Lett. B 100, (1981), 357 ; M.Athoff et al., Z.Phys. C 17,(1983),5 ; H.Aihara et al., Phys.Rev.Lett. 53,(1984), 2199 ; H. Aihara et al., Phys.Rev.Lett. 57,(1986), 3140 ; P.D. Acton et al., Phys.Lett.B 305, (1993), 415 .

[5] J.D Bjorken, Phys.Rev.D 27,(1983), 140 .

[6] P. Bozek, W. Broniowski, W. Florkowski, nucl-th/0310062.

[7] Piotr Bozek, Physics Letters B 609, (2005), 247-251.

[8] W.Broniowski, W.Florkowski, Phys.Rev.Lett. 87,(2001), 272302.

[9] J.Adams, et.al., STAR Collaboration, Phys.Rev.Lett. 92, (2004), 112301.

[10] S. Pratt and S. Cheng, Phys. Rev. C 68, (2003), 014907.

[11] A. Bialas, Phys. Rev. C 83,(2011), 024914.

[12] A. Bialas and J. Rafelski, Phys. Lett. B 633,(2006), 488-491 .

[13] A.Bialas, Physics Letters B, 579 (2004) 31-38.

[14] Sen Cheng et al., Phys. Rev. C 69, (2004), 054906.

[15] S. Pratt and S. Cheng, Phys. Rev. C 68,(2003), 014907 .

[16] Scott Pratt, Phys.Rev.C 85, 014904 (2012)

[17] Scott Pratt, Phys.Rev.Lett 108,(2012), 212301.

[18] STAR Collaboration: Phys.Rev. Lett. 90, (2003),172301 .

[19] S.Jeon and S.Pratt, Phys.Rev.C 65,(2002), 044902.

[20] NA49 Collaboration:Phys. Rev. C 71,(2005),034903.

[21] STAR Collaboration: Phys. Rev. C 82,(2010), 024905.

Chapter 3

The LHC and ALICE experiment

3.1 The Large Hadron Collider

The Large Hadron Collider (LHC) is located at the European Organisation for Nuclear Research (CERN) on the border of Switzerland and France [1]. LHC is a circular collider with two beams of protons or heavy ions circulating in opposite direction. Proton with maximum centre of mass energy $\sqrt{s}$ = 13 TeV and heavy ion (Pb) with maximum centre of mass energy per nucleon $\sqrt{s_{NN}}$ = 5.02 TeV are accelarated in LHC. LHC collider also provides asymmetric collisions i.e a collisions between proton and heavy ion. There are four interaction points in LHC rings and each interaction point is covered by large detector system. Each experiment at each interaction point has its special motivation for understanding physics of particle interaction. CMS (Compact Muon Solenoid) and ATLAS (A Toroidal LHC ApparatuS) are used to study the creation & the properties of Higgs boson and to explore the physics beyond the Standard Model. Main purpose of LHCb (Large Hadron Collider beauty) experiment is to study the CP violation in physics of heavy quarks. ALICE (A Large Ion Collider Experiment) is built to study the properties of novel matter created in heavy ion collisions. These four experimental setups are shown in Fig. 3-1.

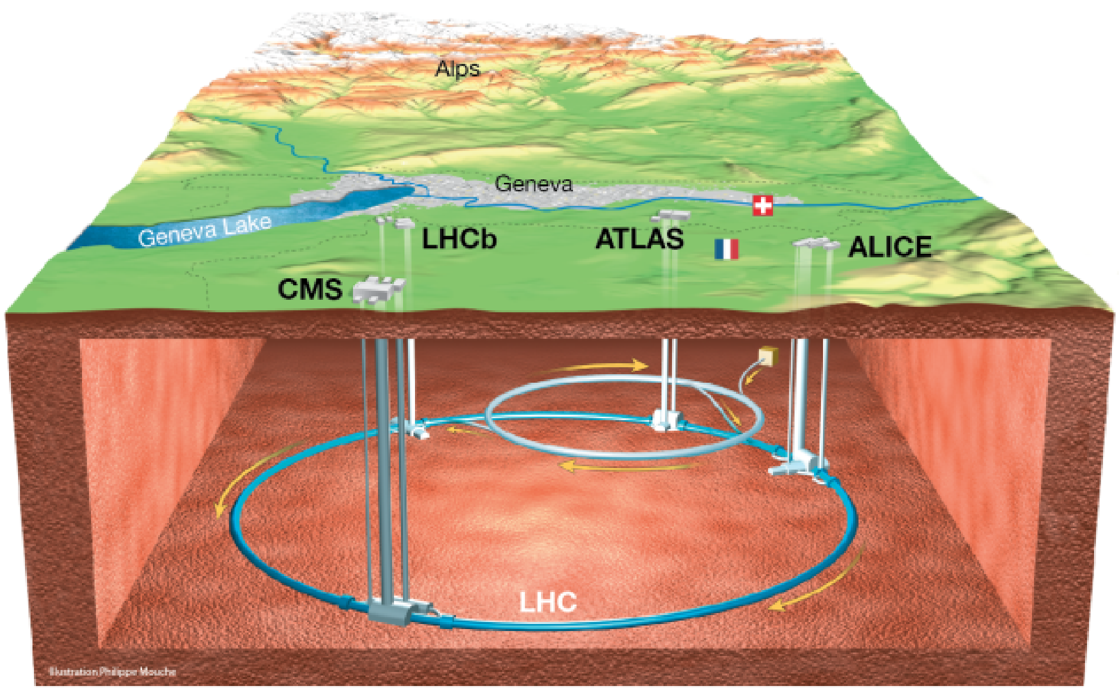

Figure 3-1: (Color online) Overall view of the LHC with 4 LHC detectors [2].

3.2 Design of the LHC

There are eight straight sections and total 9600 magnets of differen types i.e dipoles, quadrupoles, sextupoles in LHC [3, 4]. There are total 1232 dipole magnets used in the arcs for bending the beam on the curved path. Each dipole has length of 14.3m. The Quadrupoles and sextupoles are used to focus the beam or to guide the beam at region of interaction or in the insertion step. The temperature of the system is 1.9K reached by liquid helium cooling. There are eight cavities placed at the interaction regions 4 for accelarating the beam. Radio frequency (RF) of 400 MHz are used in these cavities for creating an average electrical field of 5.5 MV/m.

The Particle colliders's performance is described by beam energy and luminosity. Luminosity is defined as

$$\mathcal{L} = \frac{N_1 N_2 f N_b}{A} \tag{3.1}$$

Here, N_1 and N_2 are the number of particles per bunch and N_b is the number of bunches with a revolution frequency of f. Here A is the effective beam cross-section. For p+p collisions, luminosity is $\mathcal{L}$ = 10^{34} cm^{-2}s^{-1} and for Pb+Pb collisions it has value $\mathcal{L}$ = 10^{27} cm^{-2}s^{-1}. If the luminosity is very high, then there is a chance for multiple particle collisions in one bunch crossing. It is called pileup effect.

In a Pb ion, there are 82 protons. There is a strong repulsive force in Pb bunches with respect to proton bunches. Because of this, number of Pb ions in one bunch is decreased comapred to protons in one bunch. So there is a high luminosity in p-p collisions than Pb-Pb collisions.

There are several collimators installed at the interaction region (IR) 3 and 7 to clean the beam. Particles are scttered out of the beam at IR3 if particles have a high momentum offset. If particles have a large betatron amplitude (It is a deviation from actual path of particles designed in accelarator) scattered at IR 7. These scatterd particles are absorbed by secondary and tertiary collimators.

3.3 The ALICE experiment

ALICE [5] experiment had been designed to study the novel matter (QGP) created in high energy heavy ion collisions. The experiment has been designed to handle 8000 charged particles per unit rapidity at mid-rapidity region in collisions of Pb ions at $\sqrt{S_{NN}}$ = 5.5 TeV [6, 7] .
ALICE detector setup is represented in Fig. 3-2. There are three main subdetector system i.e the central detectors system, the muon arm and the forward detectors. The central detectors system covers midrapidity i.e $|\eta| \leq 0.9$. The muon arm has psuedorapidity range between -4 to -2.5. Different pseudorapidity ranges are covered by the forward detectors. The central detectors system is situated inside a huge solenoid magnet which produced magnetic field of strength 0.5 T.
The central detectors system is the main tracking detectors of ALICE. From the collisions vertex to the outside, the central detectors system includes six layers of high resolution silicon detectors, the Inner Tracking System (ITS), after that there is the main tracking system which measures momentum of tracks called Time Projection Chamber (TPC), a Transition Radiation Detector (TRD) for identification

of electron, and a Time of Flight (TOF) detector. Identification of particles which have high momentum is done by an array of ring-imaging Cherenkov detectors with High Momentum Particle Identification Detector (HMPID).

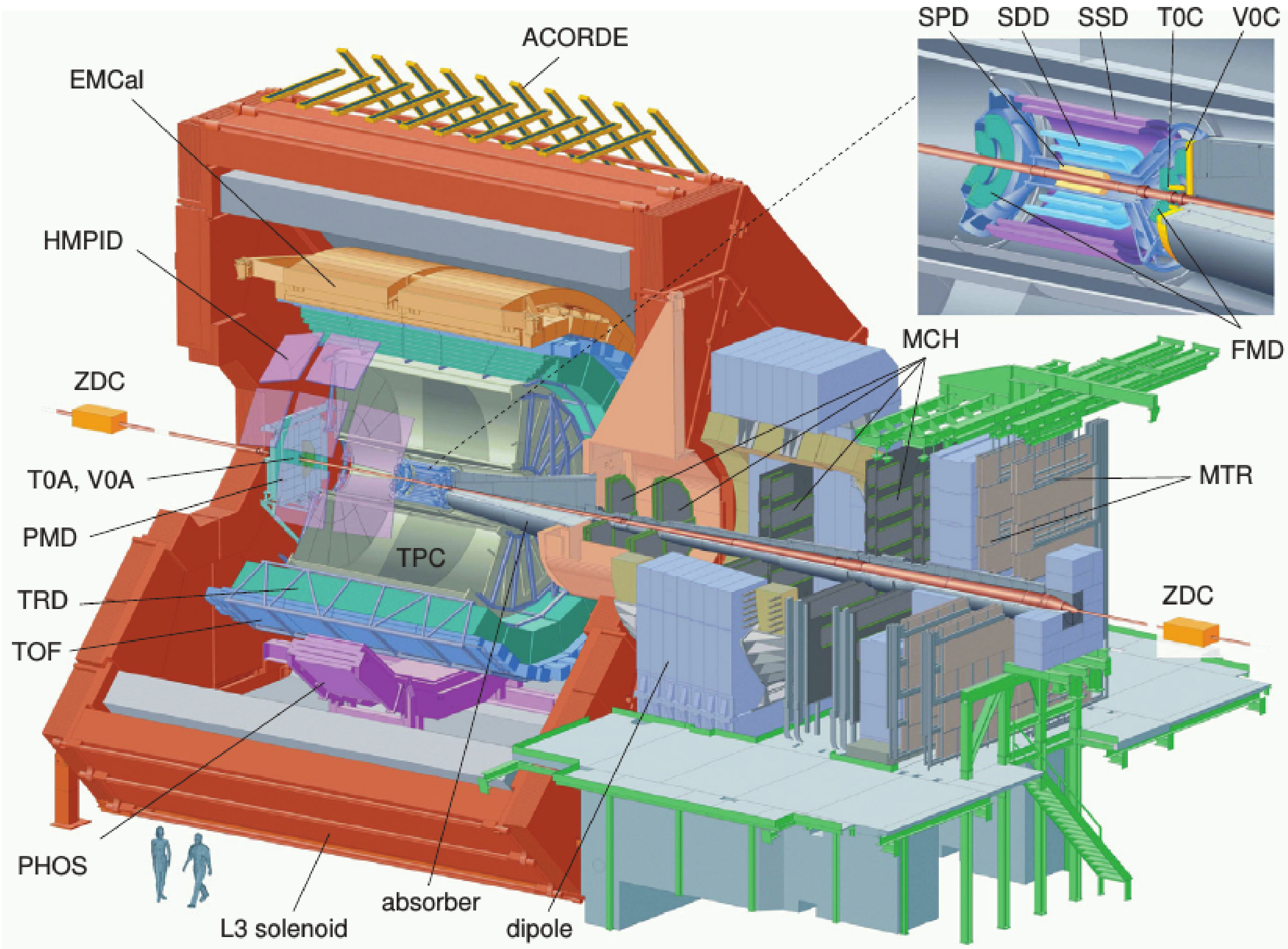

Figure 3-2: (Color online) layout of the ALICE experiment [8].

The ring-imaging Cherenkov detectors have pseudorapiditty coverage $|\eta| \leq 0.6$ and azimuthal coverage 57.6°. There are two electromagnetic calorimeters: the Photon Spectrometer (PHOS) and the Electro-Magnetic Calorimeter (EMCAL).

Arrays of high density lead-tungstate crystals are used to make the PHOS detector. It has pseudorapidity coverage $|\eta| \leq 0.12$ and azimuthal coverage $100°$. PHOS measures scintillating photons coming from the collision directly. Electro-Magnetic Calorimeter (EMCAL) is a lead-scintillator. It has pseudorapidity coverage $|\eta| \leq 0.7$ and azimuthal coverage $107°$. The muon spectrometer, Photon Multiplicity Detector (PMD) and Forward Multiplicity Detectors (FMD) belong to forward rapidity zone. PMD and FMD have a pseudorapidity coverage of $-2.6 \leq \eta \leq -1.8$ and $|\eta| \leq 5.1$ respectively. Trigger signals are provided by T0 and VZERO detectors (scintillator detectors). The Zero Degree Calorimeters (ZDC) is located at $0°$ and approximately 115m away from the interaction vertex . This detector measures energy. Reconstruction and identification of midrapidity leptons, photons and hadrons produced in collisions from very low transverse momentum ($\sim$ 100 MeV/c) to very high transverse momentum ($\sim$ 100 GeV/c) are done by the ALICE detector.

There are total 18 subdetectors. Six of eighteen are used to analysis ALICE data in this thesis. So we will discuss more details on six ALICE subdetectors. One can find detailed description of ALICE detectors in reference [9].

3.3.1 Inner Tracking System

The Inner Tracking System is the main detector system to identify primary vertex of the collisions with a resolution $\sim$100μm. The ITS consists of six layers of silicon detectors. The beryllium beam pipe is surrounded by these six layers. Radius of the beam pipe is 3 cm and the ITS provides mechanical support of beam pipe. So there is no relative movement between beam pipe and ITS. The two innermost layers located at 3.9 and 7.6 cm from the beamline form the Silicon Pixel Detector (SPD). There is a high particle density in heavy ion collisions and it is taken care by SPD. The two intermediate layers at 14.9 and 23.8 cm form the Silicon Drift Detector (SDD) & the two outermost layers at 39.1 and 43.6 cm form the Silicon Strip Detector (SSD). Fig. 3-3 shows a view of the ITS detector. The ITS is also used to reconstruct secondary vertex from decays of B mesons, D mesons and hyperons. Particle which have transverse momentum below 100 MeV are reconstructed and indetified by the ITS.

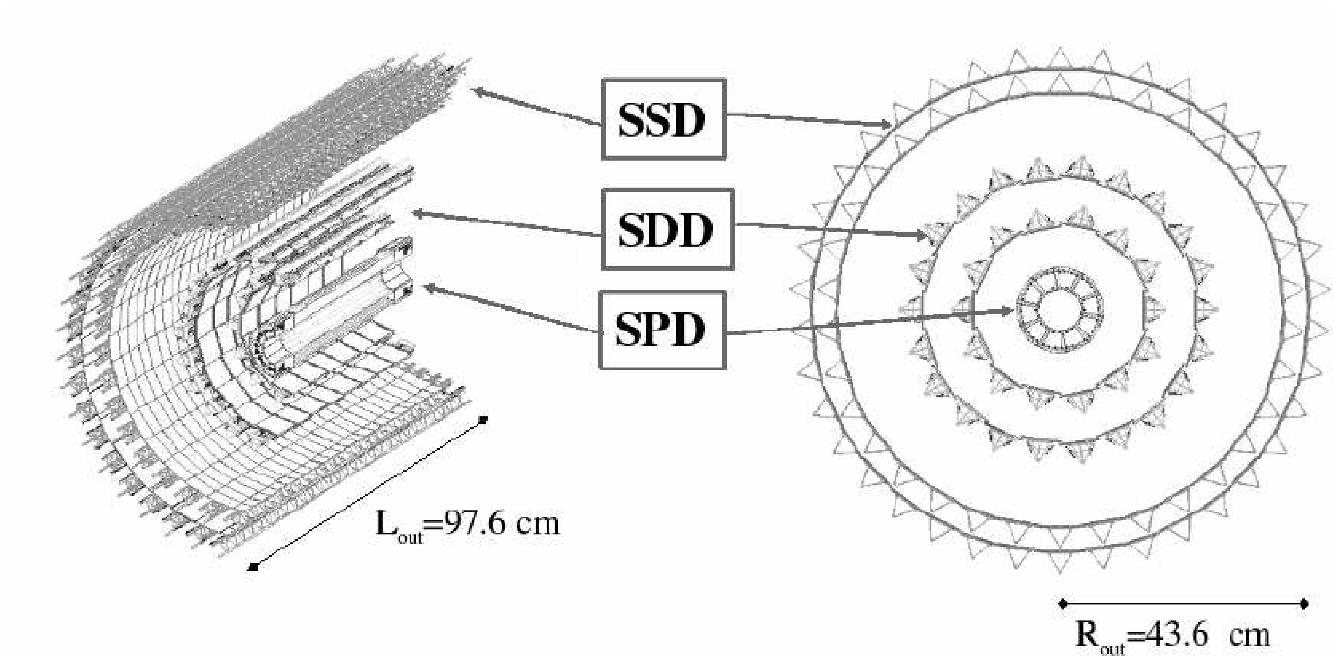

Figure 3-3: (Color online) Inner Tracking System (ITS) :The two innermost layers of Silicon Pixel Detector (SPD), the two intermediate layers of Silicon Drift Detector (SDD), and two outermost layers of Silicon Strip Detector (SSD) [5].

Particles with higher transverse momenta traverse through the Time Projection Chamber (TPC) is also done by ITS. The ITS can separate two particles with close momenta. The ITS covers transverse momentum range from $0.1 < p_T < 3.0$ GeV/c. For pions, it has relative momentum resolution better than 2% within this momentum range. In ITS, there is a non-uniformity in resulting azimuthal acceptance because of dead channels in all three subdetectors.
Number of tracks per unit area is very high at innermost planes (specially for heavy-ion collisions). So the granularity needed for this innermost planes is achieved with the SPD and SDD. The SPD and SDD have psuedorapidity coverage $|\eta| \leq$ 1.98 and $|\eta| \leq$ 0.9 respectively. There is a digital read out in SPD which does not measure the energy loss by traversing particles. There is an analog read out in SDD which performs energy loss measurements i.e dE/dx. The SDD layers are covered by a heat shield to protect heat radiation cominng from the SPD. The SSD also measures energy loss measurements. The SSD is very important for matching tracks from the ITS and TPC. The key parameters of the different layers of the ITS are described in Table. 3.1.

Table 3.1: The key parameters of the ITS [10].

Layer	Type	r(cm)	$\pm$ z	Area(m^2)	Tot. channels
1	pixel	3.9	16.5	0.09	5242880
2	pixel	7.6	16.5	0.18	10485760
3	drift	14.9	22.2	0.42	43008
4	drift	23.8	29.7	0.89	90112
5	strip	39.1	45.1	2.28	1201152
6	strip	43.6	50.8	2.88	1517568
Total area = 6.74 m^2					

3.3.2 Time Projection Chamber

The Time Projection Chamber measures momenta of particles with particle identification, vertex measurement. The TPC which is a gaseous detector was filled with 90m^3 of $Ne/CO_2/N_2$ in the ratio of 90/10/5 during LHC Run I. Gas mixture Ar/CO_2 are used in the ratio 90/10 after Run I. A view of the TPC is shown in Fig. 3-4. Length of the TPC detector along the beam direction is 5 m.

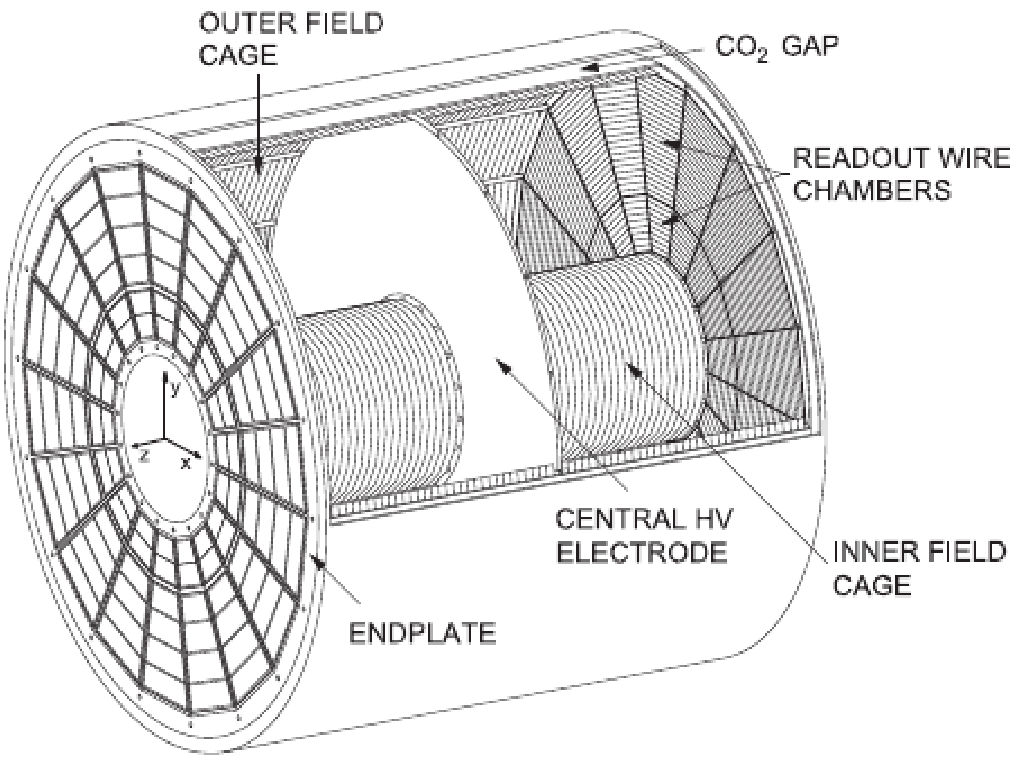

Figure 3-4: (Color online) A 3D view of the TPC. At the centre of the TPC drift volume, there is the high voltage electrode. There are total 18 sectors and 36 readouts at endplates on each end [11].

The key parameters of the TPC detector are described in Table. 3.2.

Table 3.2: The key parameters of the TPC [11].

Azimuthal coverage	2π
Radial position	85 < r < 250 cm
Length (active volume)	5000 mm
Segmentation in φ	18 sectors
Segmentation in r	2 chambers per sector
Segmentation in z	readout on 2 end-plates
Total number of readout chambers	2x2x18 = 72

The TPC covers pseudorapidity range from $|\eta| \leq 0.98$ upto $|\eta| \leq 1.5$. Particles upto 100 GeV/c transverse momenta are reconstructed with a good momentum resolution (if p_T < 20 GeV/c, there are 6% and 4.5$\%$ momentum resolution in Pb+Pb and p+p collisions respectively) by the TPC. Transvere momentum resolution from combination of ITS and TPC is shown in Fig. 3-5. From this figure, it is seen that at $p_T \approx$ 0.2 GeV/c resolution is minimum and it increases with increasing p_T . It has resolution 20% at p_T = 100 GeV/c.
The TPC also identifies particles by measuring the energy loss caused by interaction with the gas of the TPC detector. Measurement of energy loss when particles traversed through gas as a function of total momentum i.e p (Gev/c) is shown in Fig. 3-6. At lower momentum, one can separate between different particle species. But at large momentum, it is not possible to separate particles.

3.3.3 Time Of Flight detector

The Time of Flight detector consists of Multi-gap resistive-Plate Chambers (MRPC). The TOF is placed at a radial distance from 3.77 m to 3.99 m. The TOF detector has two cathodes separated by 5 layers of glass, an anode and more 5 layers of glass.

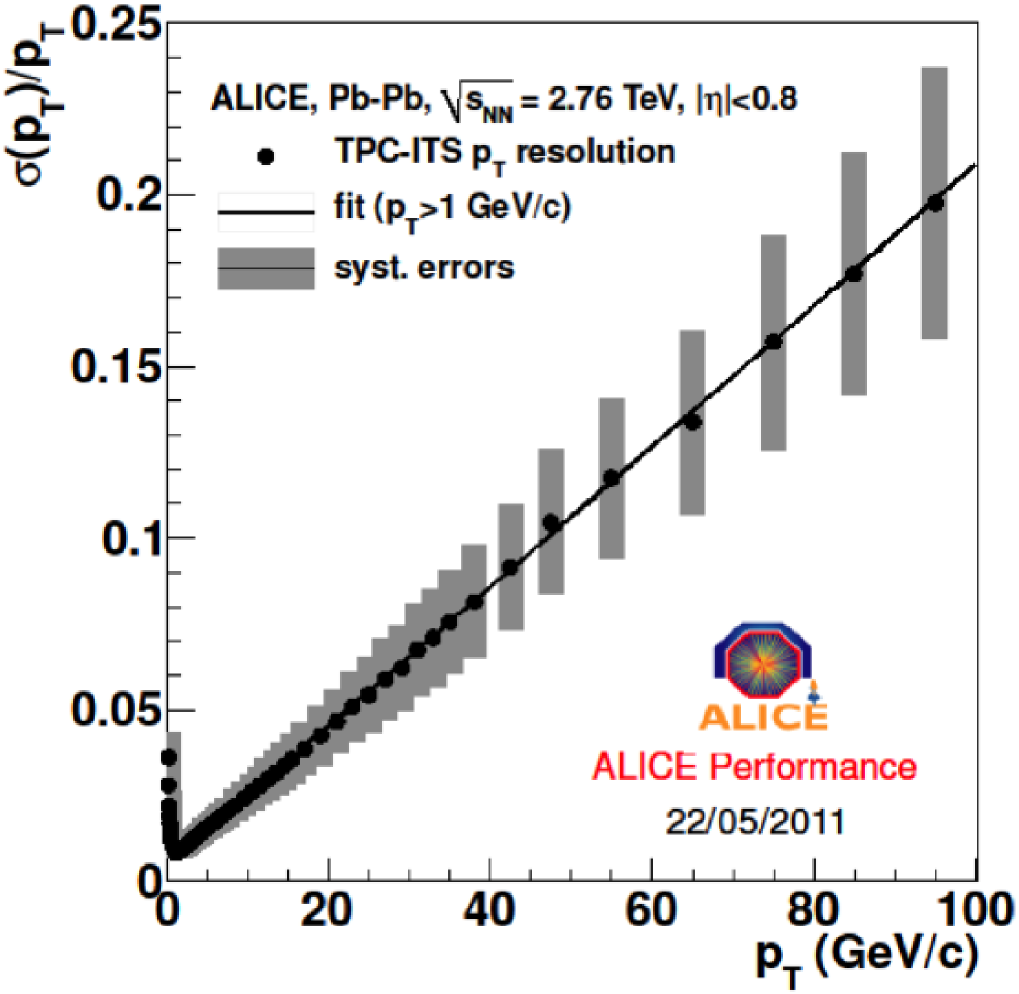

Figure 3-5: (Color online) ITS-TPC p_T resolution in Pb+Pb collisions at $\sqrt{S_{NN}}$ = 2.76 TeV [8].

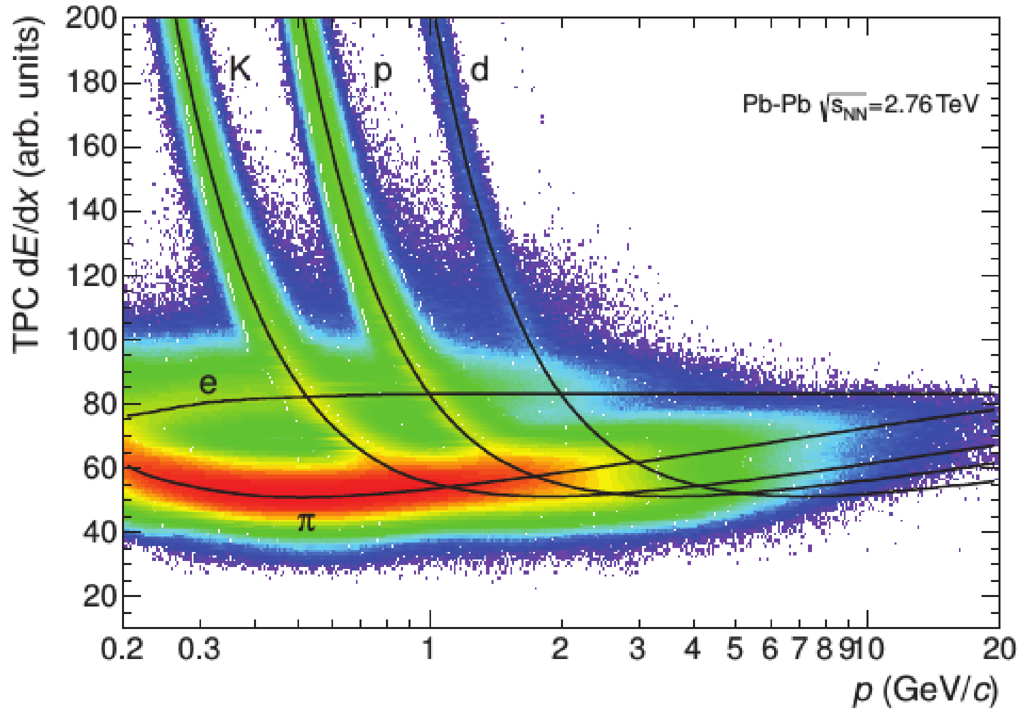

Figure 3-6: (Color online) Left: Specific energy loss (dE/dx) in the TPC vs. particle momentum in Pb-Pb collisions at $\sqrt{s_{NN}}$ = 2.76 TeV. The lines show the parametrisation of the expected mean energy loss. There are no separation between pion, kaon and proton at large momentum. [8].

Whole of this is filled with a pressurized gas. A differential high voltage across the cathodes and anode is applied [12]. The TOF covers psuedorapidity range $|\eta| < 0.9$. The TOF detector has time resolution of 80 ps and identified partilces which have momentum range between 2 to 5 GeV/c. Pion/kaon separation is done by TOF with 3σ cut upto 2.5 GeV/c and kaon/proton with 4σ upto 4 GeV/c . The key parameters of the TOF are desrcibed in Table. 3.3.

Table 3.3: The key parameters of the TOF [8].

Azimuthal coverage	2π
Radial position	3.77 < r < 3.99 cm
Length	7.45 m
Detector active area	141 m^2
Gas volume	16m^3

The TOF is used to measure the time for each particle between its producion in the initial collision and the moment when the particle reaches at the detector. The start time i.e t_0 is given by the TZERO detector. One can calulate the velocity of particle i.e β using Eq. 3.2.

$$\beta = \frac{L}{tc} = \frac{1}{\sqrt{(\frac{mc}{p})^2 + 1}} \tag{3.2}$$

Here L is reconstructed trajectory of particles and t is time measured by TOF. The momentum of the particles i.e p is calculated from the curvature of tracks in the ITS and TPC. So particles with same momenta can be separated by TOF because of different mass.

3.3.4 VZERO detector

The VZERO detector consists of two arrays of scintillator detectors (V0A and V0C) placed along the beam line asymmetrically on each side of the interaction point [5, 13]. V0A and V0C have pseudorapidity coverage $2.8 < \eta < 5.1$ and $-3.7 < \eta < -1.7$ and is placed at 340 cm and at 90 cm respectively. The V0A and V0C are segmented into 32 elementary counters which are distributed in 4 rings and 8 sectors of 45°. The individual scintillation counters has time resolution better than 1 ns and VZERO detector is used as a trigger. The VZERO detector can differentiate between beam-gas interaction and beam-beam interaction by calculating time difference between the arrival of particles at detectors. The beam-beam interaction takes place in between V0A and V0C always. But beam-gas interaction takes place everywhere. The VZERO detector measures global properties of pp, p-Pb and Pb-Pb collisions such as the number of tracks in the collisions i.e multiplicity. Centrality of the collisions is measured with a resolution $\sim$0.5% centrality bin width for most central collisions and $\sim$2% for more peripheral collisions. The distribution of sum of two VZERO amplitude is shown in Fig. 3-7.

3.3.5 T0 detector

The T0 detector consists of arrays of Cherenkov counters. Start time for the TOF detector is given by T0 detector [5]. Time measured by T0 detector is independent of position of vertex position. The T0A and T0C have pseudorapidity coverage $4.61 < \eta < 4.92$ and $-3.28 < \eta < -2.97$ respectively. The collisions time measured by T0 detector has precision of 50 ps.

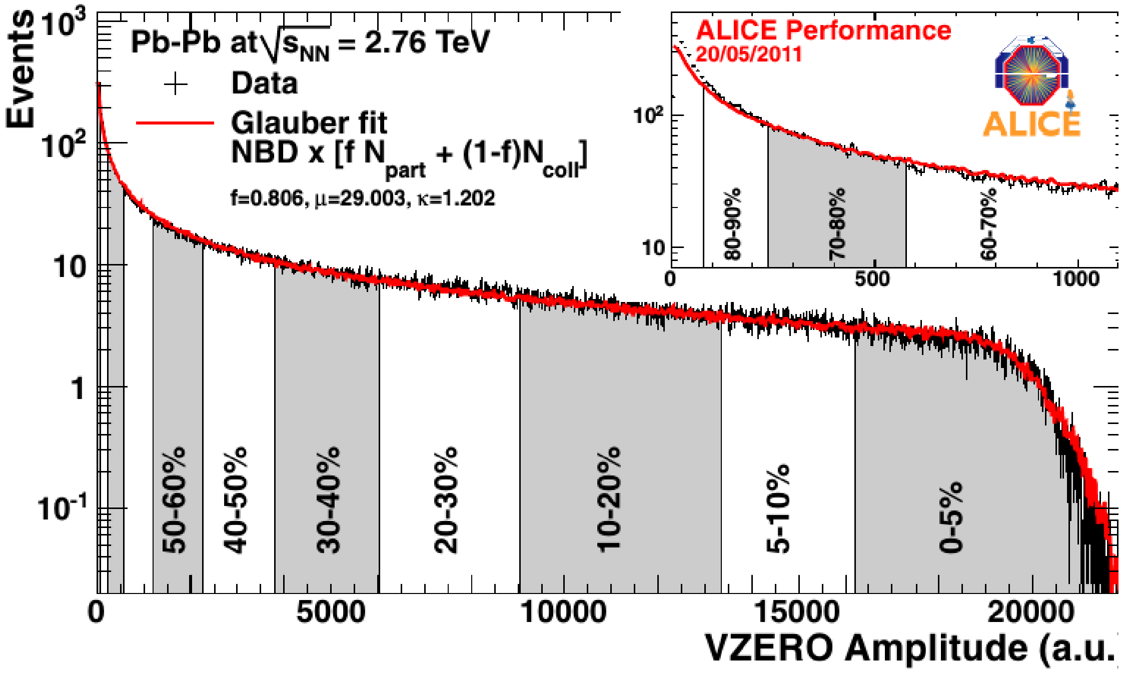

Figure 3-7: (Color online) Sum of two VZERO amplitude for Pb-Pb collisions at $\sqrt{s_{NN}}$ = 2.76 TeV. The distribution is fitted by Glauber model and this distribution is used to calculate centrality of the collisions. [14].

3.3.6 The Zero Degree Calorimeter

The Zero-Degree Calorimeter (ZDC) is a hadronic calorimeter. The ZDC is placed at 115 m on both sides of the interaction region. The ZDC measures nucleons which are not involve in collisions. One can find these particles very close to the beam path. These nucleons are called spectators. Since proton has a positive charge, so mangnetic field of LHC gives a force on protons and deflects protons while neutrons follow straight path. The beam pipe is split into two pipes. The calorimeter (ZN) measuring neutrons placed in between two pipes at an angle 0° with respect to beam axis. The calorimeter (ZP) which measures the protons is placed next to the beam pipe at the location to which the protons are bended to.
There are two electromagnetic calorimeters (ZEM) opposite to muon arm on both sides of the beam line at a distance of 7 m from the interaction point. Energy measurment of partilces which are emitted in the forward direction is done by ZEM. One can get centrality information of an event using the ZDC and ZEM detectors together [5].

Bibliography

[1] European Organization for Nuclear Research (CERN). https://home.cern/topics/large-hadron-collider.

[2] Overall view of the lhc: https://cds.cern.ch/record/1708847.

[3] Lyndon Evans and Philip Bryant. LHC Machine. JINST, 3, (2008),S08001.

[4] C Lefevre. LHC the guide, 2009. CERN-Brochure-2009-003-Eng at http://cdsweb.cern.ch/record/1165534?ln=de.

[5] ALICE Collaboration. The ALICE experiment at the CERN LHC. JINST, 3, (2008),S08002.

[6] M. L. Noriega, "Jet physics in alice" European Physical Journal C-Particles and Fields, vol. 49, no. 1, (2007), 315-319, . 29, 35, 36, 47

[7] T. Bird, "An overview of the ALICE experiment", tech. rep., University of Southhampton, January 2010. 47

[8] ALICE Collaboration: Int. J. Mod. Phys. A 29 (2014) 1430044.

[9] ALICE Collaboration: "Physics Performance Report Vol. I, CERN/LHCC 2003-049", ALICE PPR Volumen I and Volume II.

[10] https://doi.org/10.1016/j.phpro.2012.02.443

[11] The ALICE TPC: Nucl. Instrum.Meth. A 622, (2010),316-367

[12] G. Dellacasa et al., (ALICE Collaboration), ALICE Technical Design Report of the Time Of Flight system (TOF), CERN, 2000

[13] ALICE Collaboration: "Performance of the ALICE VZERO system", JINST 8 (2013) P10016, arXiv:1306.3130 [nucl-ex].

[14] Alberica Toia and ALICE Collaboration : J. Phys. G: Nucl. Part. Phys.38, (2011), 124007

Chapter 4

Data analysis and results

In this chapter, the data set, event and track selections applied in the ALICE data analysis are discussed. Section 4.1 and 4.2 specify Pb+Pb collisions data set with the event and track procedures respectively. Identification of particles is described in section 4.3. Section 4.4 describes contamination in particle identification and correction for detector effciency. Construction of BF and results are shown in section 4.5 and 4.6 respectively.

4.1 Data sample

The analysis is done using ALICE Pb+Pb collision data recorded at energy $\sqrt{s_{NN}}$ = 2.76 TeV in 2010 LHC Run I. Approximately 11.98 million minimum-bias events have been analysed. Data sets for analysis are selected based on the quality assessment done in the ALICE framework. There are condtions for data quality assurance as discussed below.

For analysis, only events tagged as "physics" events during data taking have been considered. Other sets of events have been rejected during LHC luminosity scanning. The data reconstructed after proper calibration have been used for further processing.

4.2 Event and track selection

Once the physics datasets have been chosen, minimum bias trigger (MB) was used to synchronize signals in the VZERO-A and VZERO-C detectors online. Contamination from background events is reduced by offline event selection used also to validate online data selection. Sources of background events are beam-gas interaction and electromagnetic interaction. Beam-gas interaction occurs because of collision between particles in the beam and residual gas in the beam pipe. Beam-beam collision happens latter compared to background events. Using the time information, beam-beam interaction is taken and beam-gas interaction is rejected(as discussed in reference 8 of chapter 3). There is a finite acceptance and size of the ALICE central barrel detectors (specially TPC), so collisions which occured very close to the centre of detector are used for analysis. For this reason z-component of the reconstructed primary vertex is selected to be within 10 cm from the centre of the detector i.e $|V_z| < 10$ cm. Vertex-z distribution is shown in Fig. 4-1. Because of this cut, there is a uniform reconstruction efficiency in the pseudorapidity range $|\eta| < 0.8$.

VZERO scintillator detectors are used to obtain multiplicity of an event. Multiplicity of an event is characterised according to the charge deposition in the VZERO-A detector. VZERO-A is very sensitive to fragmentation of Pb ions. It is because of alignment of VZERO-A detector along the Pb beam direction.

A track is selected as a good track for analysis if it has at least 70 reconstructed space points in the TPC out of 159 space points. Because of this cut , secondary particles produced from weak decays or from the interaction of particles with collider material are removed.

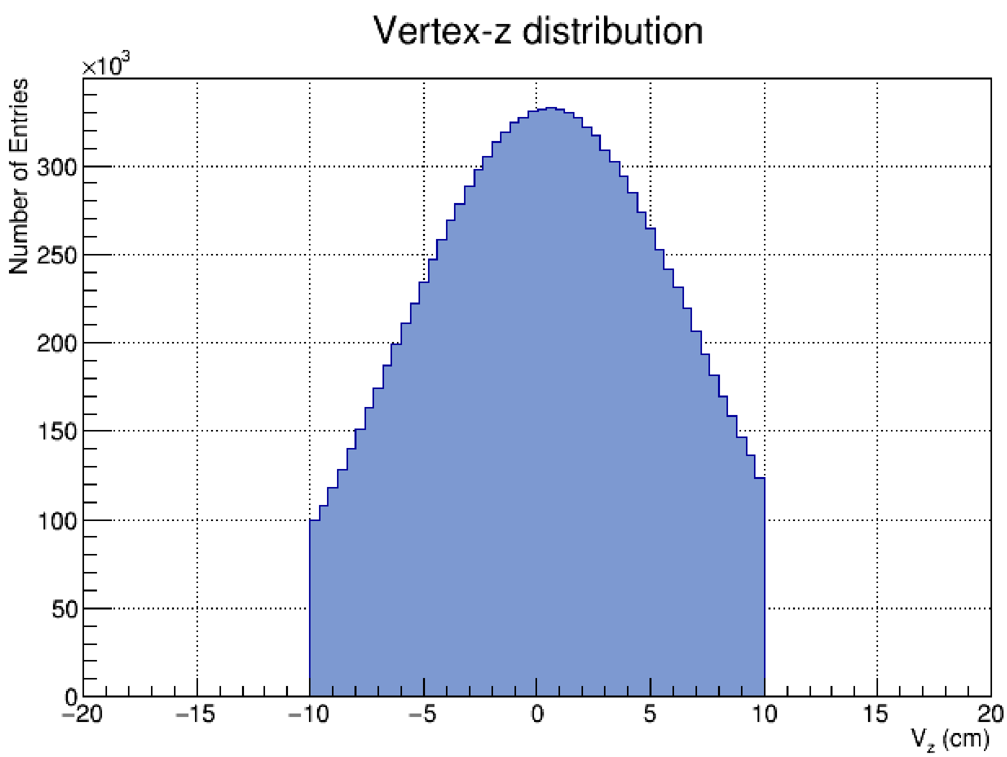

Figure 4-1: (Color online) Vertex-z distribution of Pb+Pb collisions at $\sqrt{S_{NN}}$ = 2.76 TeV.

The χ^2/NDF of the momentum fit per TPC cluster is needed to be below 4, the distribution of which is shown in Fig. 4-2. The distance of closest approach (dca) a track and the event's primary vertex is required to remove further contamination from background tracks. If a track has $dca_{xy} = \sqrt{dca_x^2 + dca_y^2} > 2.4$ cm and $dca_z > 3.2$ cm, this track is not considered for analysis. Reconstruction of tracks have been performed using information from both the ITS and the TPC for a uniform azimuthal angle distribution. Electrons from γ conversions and π^0 decays are rejected using energy loss measurement by TPC. Particles are excluded if the energy distribution of the particles are within 3σ from the theoretical Bethe-Bloch line of specific energy loss in TPC [1]for electrons.

As a next step of data analysis, a pair of opposite charged tracks are taken that fulfill the track selection criteria. There are some contributions from detector effects in these calculated like and unlike-sign pairs. One track is reconsturcted as two tracks because of two track shared same cluster in TPC. Two tracks might also be reconstructed as a signle track due to fusion of clusters. Contributions from track splitting and tracks merging on formation of charged pairs are reduced by applying a cut on the closest distance of two tracks at the entrance of the TPC. Angular difference between two tracks i.e. $\Delta\varphi^*$ used for reduction the contributions from track spliting and tracks merging is given by Eq. 4.1. Pairs which satisfy $|\Delta\eta| < 0.02$ and $|\Delta\varphi^*| < 0.02$ are rejected.

$$\Delta\varphi^* = \varphi_1 - \varphi_2 - \arcsin\left(0.0075\frac{B_z.r}{p_{T1}}\right) + \arcsin\left(0.0075\frac{B_z.r}{p_{T2}}\right) \tag{4.1}$$

Here φ_1 and φ_2 are azimuthal angles of two tracks used for forming pairs, p_{T1} and p_{T2} are transeverse momenta of two tracks, B_z is z-component of the magnetic

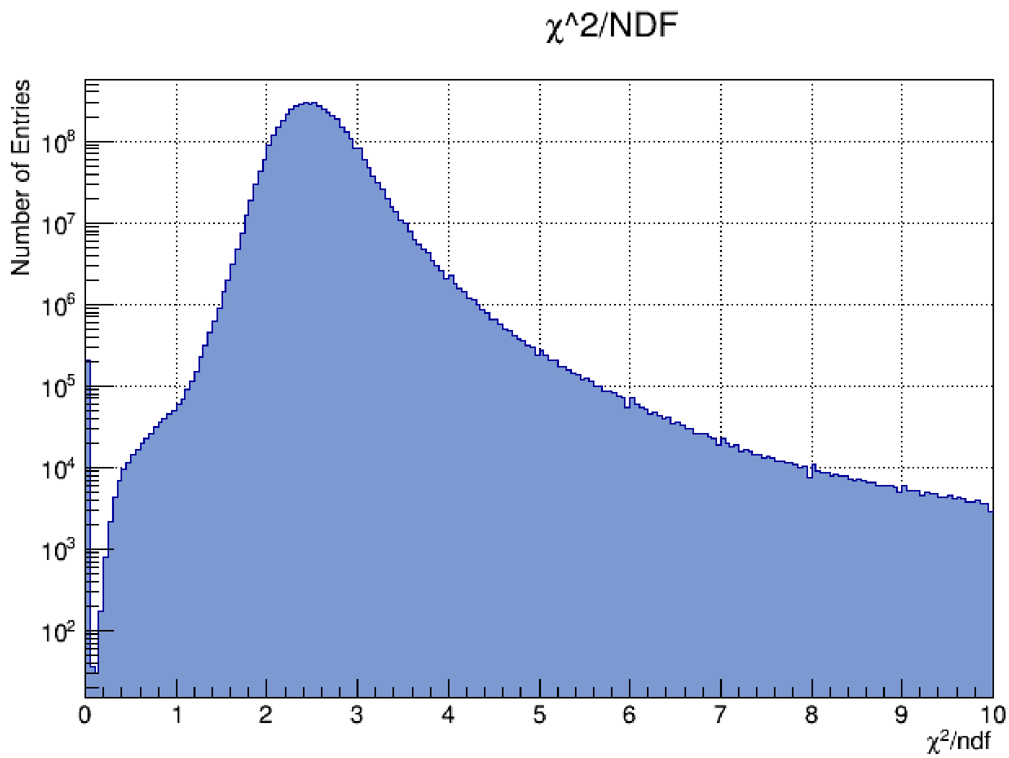

Figure 4-2: (Color online) Distribution of χ^2/NDF for TPC cluster.

field and r is the radius of the TPC with a range of $0.8\ \text{m} < r < 2.5$ m. There are some contributions from short range correlation. Short range correlation is arising from coulomb attraction, repulsion and quantum statistical correlations between two charged particles which are used to form a pairs. A cut on transverse momentum difference between two tracks forming a pair is applied to reduce the short range correlation. The contribution of short range correlation is observed mainly at point $(\Delta\eta, \Delta\varphi)$ = (0,0) in the balance function distribution. There is a peak or dip in the projection of balance function. We have applied Δp_T cut 0.1 GeV/c in this analysis. Δp_T = 0.1 GeV/c is used because quantum statistical correlation/short-range correlations affect balancing pair at small relative momentum.
In this analysis, we have used p_T range of 0.2 to 1.4 GeV/c and pseudorapidity range of $|\eta| \leq$ 0.8. For obtaining correlation function, associated and trigger particles are used to form pairs as function of $\Delta\eta$ and $\Delta\varphi$. Here trigger particle is a particle which has transverse momentum above transverse momentum of associated particle in a defined p_T range.

4.3 Particle identification

Using signals from TPC and TOF detectors, identification of pions, kaons and protons are performed. There is a method called $n\sigma$ method which is used for identification of particles, here σ is the deviation of the measured dE/dx from the Bethe-Bloch estimation of specific energy loss (dE/dx) of particle in the TPC or the deviation of the measured time-of-flight from expectation of reaching time in the

TOF. The dE/dx distributions for pion, kaon and proton are shown in left panel of Fig. 4-3 without $n\sigma$ cut. The right panel of Fig. 4-3 shows β (v/c) distribution of pion, kaon and prton for Pb+Pb collisions at $\sqrt{s_{NN}}$ = 2.76 TeV.

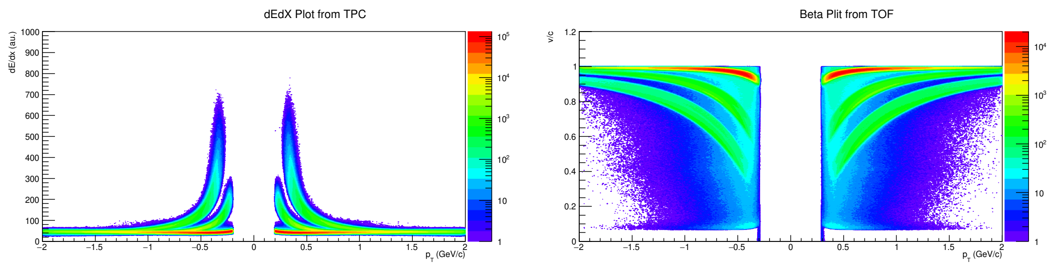

Figure 4-3: (Color online) dE/dx (left) and Beta (right) plot from TPC and TOF detector respectively for pion, kaon and proton at Pb+Pb collisions with $\sqrt{s_{NN}}$ = 2.76 TeV.

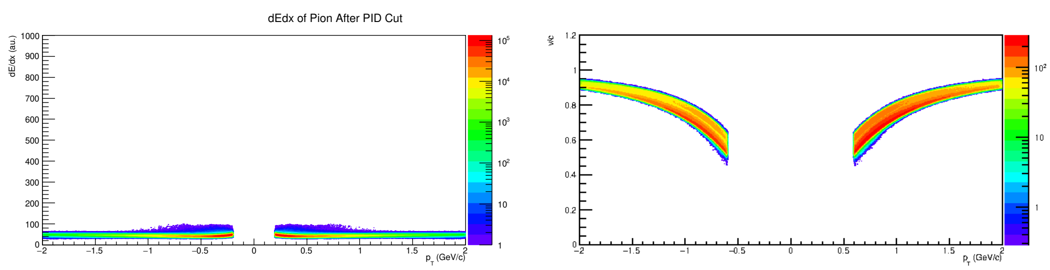

Figure 4-4: (Color online) dE/dx (left) and Beta (right) plot from TPC and TOF detector respectively for pion at Pb+Pb collisions with $\sqrt{s_{NN}}$ = 2.76 TeV after $n\sigma <$ 3 cut.

After $n\sigma$ $<$ 3 cut, dE/dx and β distributions of pions are shown in Fig. 4-4. Here, TPC information have been used for pion identification of particle in the range of $0.2 < p_T < 0.6$. If particle has $p_T > 0.6$, then, the information from both TPC and TOF both have been used to identify particles. The combined $n\sigma$ is defined as $n\sigma^2_{tot} = n\sigma^2_{TPC} + n\sigma^2_{TOF}$.

4.4 Correction

4.4.1 Contamination and efficiency correction

The particles used for balance function analysis are corrected for detector inefficiencies and mis-identification of particles. Montecarlo (MC) simulation data have been used to extract particle efficiency (ϵ) and contamination(λ). HIJING event generator [2] has been used as input to the monteacarlo simulation. The particle efficiency is defined by Eq. 4.2. $N_{reconstructed}$ is the number of reconstructed primary particles of a particular type and N_{truth} is the number of generated primary particles of that type. The contamination is defined by Eq. 4.3. Here $N_{contamination}$ is the number of particles satisfying the criteria but originated from mis-identificated particles. The final correction factor is defined by Eq. 4.4. These factors are calculated for each bin in the grid of transverse momentum p_T , pseudorapidity η and azimuthal angle φ. This correction factor $C_{\lambda,\epsilon}$ is applied to each track for each event as a weighting factor while filling the correlation histograms for same and mixed events. Fig. 4-5 shows single particle contamination (upper panel) , efficiency (middle panel) and final correction factors (lower panel) for pions projected in η, p_T and φ. It is observed that efficiency in η is around 70%. There is a drop of efficiency at η = 0. It is because of the number of particles crossing the central membrane of TPC. It is not possible to reconstruct particles at the central membrane region. The efficiency rises steeply upto the transverse momentum of 0.6 GeV/c and the value of efficiency at $p_T \approx$ 0.6 GeV/c is around 80% as calculated by using TPC only. Efficiency in p_T slightly increases from p_T = 0.6 GeV/c to

2 GeV/c as calculated using TPC+TOF. There is a structure observed in efficiency of φ. It is because of the TPC sectors.

$$\epsilon = \frac{N_{reconstructed}}{N_{truth}} \tag{4.2}$$

$$\lambda = \frac{N_{contamination}}{N_{reconstructed} + N_{contamination}} \tag{4.3}$$

$$C_{\lambda,\epsilon} = \frac{1 - \lambda}{\epsilon} \tag{4.4}$$

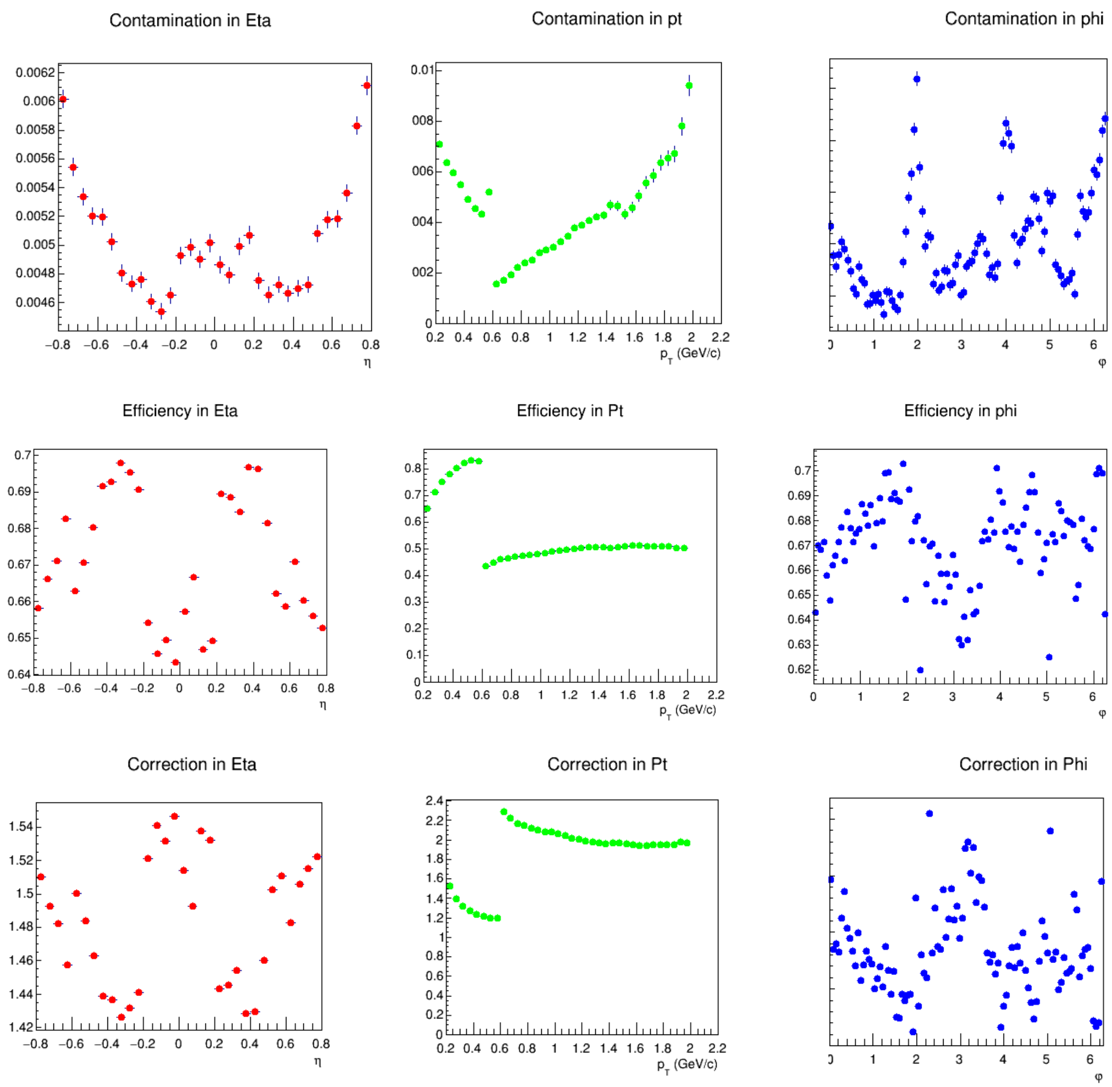

Figure 4-5: (Color online) distributions of Contamination , Efficiency and Correctionfor for Pion in η, p_T and φ at Pb+Pb collisions with $\sqrt{S_{NN}}$ = 2.76 TeV energy.

4.4.2 Mixed event for acceptance correction

The event mixing technique is used to correct detector acceptance for each term of the balance function (Eq. 2.3). Mixed events are formed by combining tracks from different events of similar multiplicity and V_z. There is no remainings physical correlation when a two particle correlation function is calculated using tracks from mixed events. In this analysis 5 events are used to make mixed event. Mixing of 5 events give almost no correlation between particles and it has been used to produce large number of mixing events. Fig. 4-6 shows 2D two particle correaltion for like and unlike sign pairs in $\Delta\eta - \Delta\varphi$ space normalised to 1 at $(\Delta\eta, \Delta\varphi)$ = (0,0). Probability of finding particle pair is higher when particles are very close in η, so we assign this probability to 1. This region also represents maximum amplitude

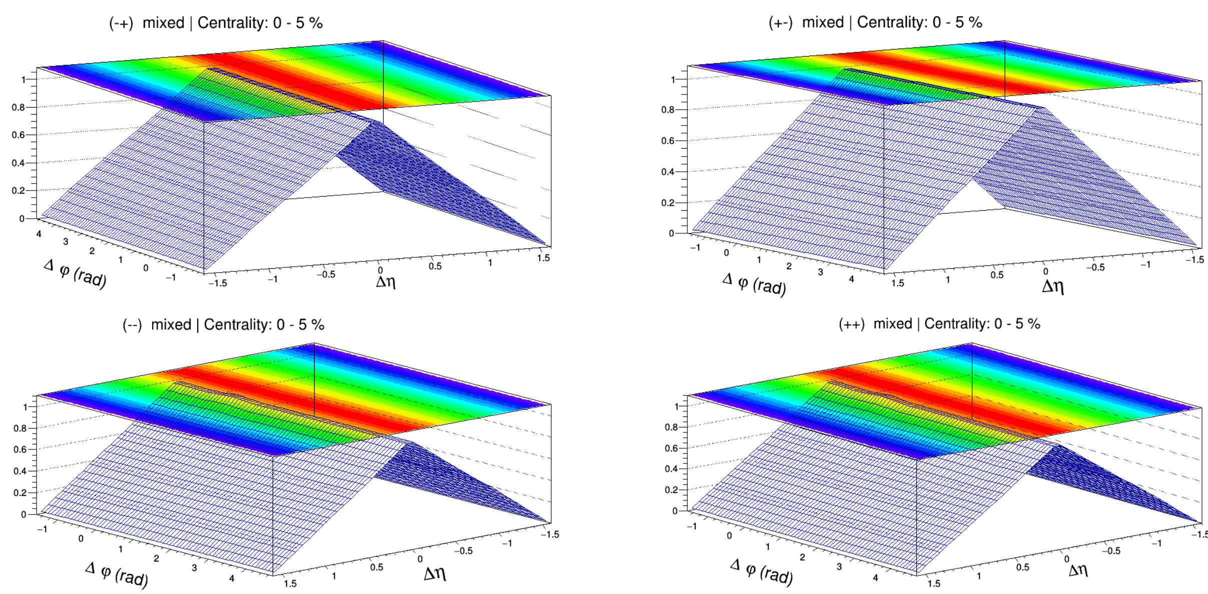

Figure 4-6: (Color online) Two particle correlation for unlike sign (upper) and like sign pairs (lower) in $\Delta\eta - \Delta\varphi$ space using particles from mixed events for 0-5%

4.5 Construction of Balance function

Correction factors as mentioned in section 4.4 have been applied for calculating each term of the equation describing the balance function. The correction factor represents the probability that given a particle i.e *"a"* is reconstructed, another particle i.e *"b"* produced at a relative pseudorapidity ($\Delta\eta = \eta_a - \eta_b$) or azimuthal angle ($\Delta\varphi = \varphi_a - \varphi_b$) would be measured. *a* is called trigger particle and b is called associated particle. p_T of trigger particle is greater than p_T of associated particle. If every charge has an opposite balancing charge, then balance function is normalized to 1 as maintained in Eq. 2.4. In this analysis, balance function of pion is measured within a finite phase space in $|\eta| < 0.8$ and transverse momentum range of 0.2 to 1.4 GeV/c. Within this phase space on event by event basis, the number of positive pions is not equal to the number of negative pions. So balance function of pions should be fractional. Now Eq. 2.3 is rewritten as

$$B(\Delta\eta, \Delta\varphi, p_{T,trig}, p_{T,assoc}) = \left\{ C_{+-}(\Delta\eta, \Delta\varphi, p_{T,trig}, p_{T,assoc}) - C_{--} + C_{-+} - C_{++} \right\} \tag{4.5}$$

Here factor 1/2 is removed because of $p_{T,trig} > p_{T,assoc}$. Here $C_{a,b}$ represents associated yield per trigger particle where a and b could be both positive and negative charged particles. $C_{a,b}$ is written as

$$C_{a,b} = \frac{1}{N_{trigg,a}} \Big[\frac{d^2 N_{same,(a,b)}}{d(\Delta\eta) d(\Delta\varphi)} / \frac{d^2 N_{mixed,(a,b)}}{d(\Delta\eta) d(\Delta\varphi)} \Big] \tag{4.6}$$

$N_{trigg,a}$ represents number of trigger particles *a* and $\frac{d^2 N_{same,(a,b)}}{d(\Delta\eta)d(\Delta\varphi)}$ is particle pair distribution for *a* and *b* type particles from same event. Now $C_{a,b}$ term is corrected for contamination and detector inefficiencies on track by track basis. Pair inefficiencies and acceptance are corrected using mixed event particle pair distribution for *a* and *b* type particles i.e. $\frac{d^2 N_{mixed,(a,b)}}{d(\Delta\eta)d(\Delta\varphi)}$

After constructing two-dimensional balance function distributions in $\Delta\eta$ and $\Delta\varphi$ using all terms in Eq. 4.5, two dimensional correlation plots are projected along $\Delta\eta$ and $\Delta\varphi$ directions. When projection takes place in $\Delta\eta$, we consider $\Delta\varphi$ range $-\pi/2 < \Delta\varphi < \pi/2$. When projection takes place in $\Delta\varphi$, full $\Delta\eta$ i.e $\Delta\eta < 1.6$ is considered. The shape of the one dimensional distribution in $\Delta\eta$ or in $\Delta\varphi$ is quantified by the variance of this distribution.

4.6 Results and Discussions

In this section, results of pion balance function distributions for Pb+Pb collisions at $\sqrt{S_{NN}}$ = 2.76 TeV energy have been discussed.

4.6.1 Balance function of pion in Pb+Pb collisions at $\sqrt{S_{NN}}$ = 2.76 TeV

Balance function of pions in Δy and $\Delta\varphi$ are shown in Fig. 4-7 for three centrality classes. 2D plots from most central collisions (0-5%) to most peripheral collisions (60-70%) are shown. The trigger and associated particles have transverse momenta in the range 0.2 GeV/c $< p_T < 1.4$ GeV/c. It is obeserved that bulk of the pion correlation is at the near side of $\Delta\varphi$ region i.e $-\pi/2 < \Delta\varphi < \pi/2$. Balance function gets narrower in the near side region when centrality of event goes from peripheral to most central. The method of centrality determination has been discussed in 3.3.4.

There are several characteristic structures in two particles correlation functions. Here some of these structures are described. There is a peak at $(\Delta\eta, \Delta\varphi) = (0, 0)$ called near side jet peak. The origin of this peak is intra jet correlations and correlations because of resonance decays. An elongated structure at $\Delta\varphi = \pi$ is ovserved over $\Delta\eta$ resulting from correlation of particles from back-to-back jets. A peak $\Delta\varphi$ = 0 is oberserved over large values of $\Delta\eta$ called ridge structure [3] - [17]. There is a depletion around point at $(\Delta y, \Delta\varphi) = (0, 0)$ for all centrality classes. There is a centrality dependence of this depletion. The depletion is more prominent at the most peripheral collisions as seen in Fig. 4-7. At most central collisions, pion balance function has a smaller depletion than the corresponding value in peripheral collisions. It is observed that there is larger magnitude of balance function at $\pi/2 < \Delta\varphi < 3\pi/2$ for peripheral collisions compared to central collisions.

Now the projection of pion balance function distributions for Pb+Pb collisions at $\sqrt{s_{NN}}$ = 2.76 TeV is shown in Fig. 4-8 as a function of Δy (right panel) and $\Delta\varphi$ (left panel). Events with 0-5%, 30-40% and 60-70% centralities are represented by red, blue and green colours respectively. Each point in these plots has statistical and systematic errors shown. The Systematic error is discussed in section 4.6.2. After careful examination of Fig. 4-8, it is observed that the shape of distributions

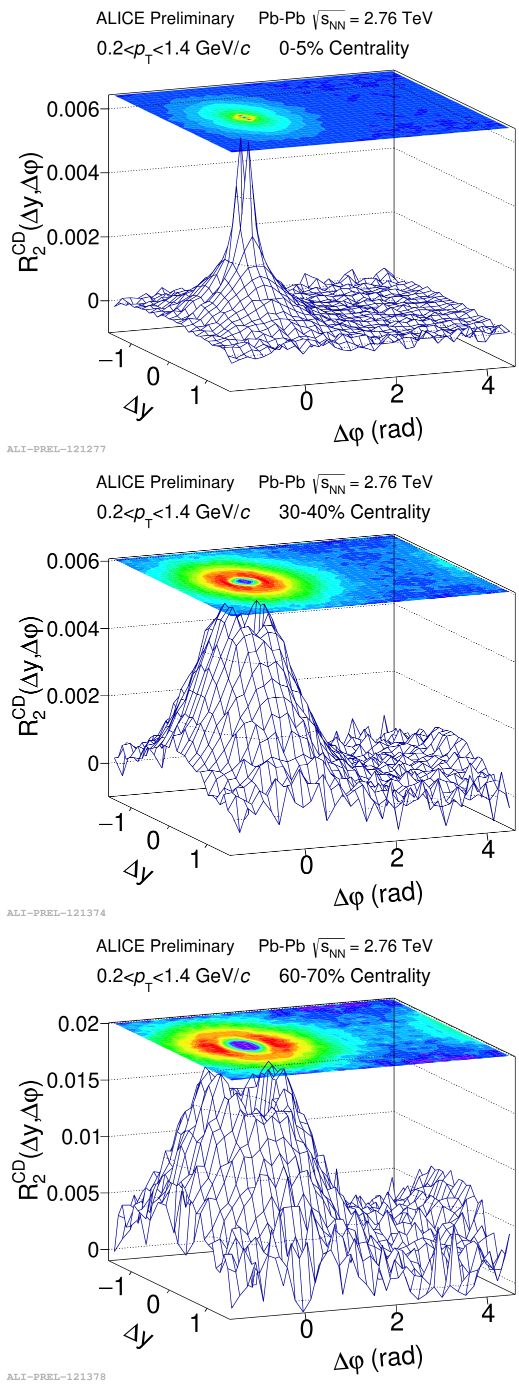

Figure 4-7: (Color online) Balance function distributions of pions as a function of Δy and $\Delta\varphi$ in Pb+Pb collisions at $\sqrt{S_{NN}}$ = 2.76 TeV. 2D plots for three centrality classes 0-5%, 30-40% and 60-70% from top to bottom are shown.

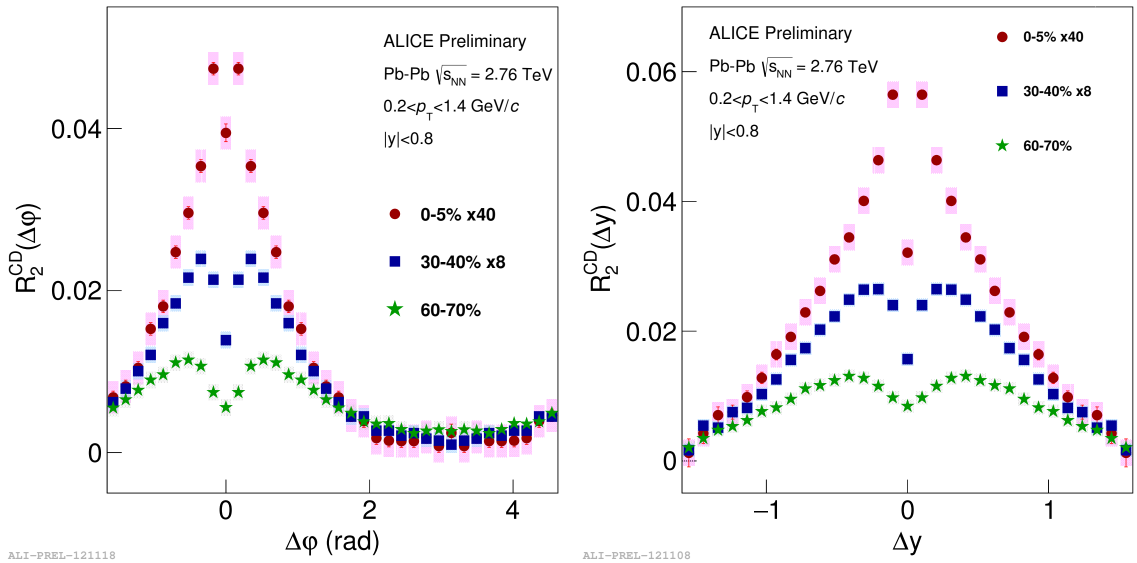

Figure 4-8: (Color online) Projected Balance function distributions of pion for Pb+Pb collisions at $\sqrt{S_{NN}}$ = 2.76 TeV in Δy and $\Delta\varphi$ for three centrality classes 0-5%, 30-40% and 60-70%.

in both Δy and $\Delta\varphi$ changes with centrality. The distributions are narrower for the most central collisions with respect to that of the peripheral collisions. Distributions are symmetry around the mean projected position for all centrality classes. A depletion structure is observed at point $(\Delta y, \Delta\varphi)$ = (0,0) as mentioned earlier. The reason of this depletion is short range correlations i.e Coulomb attraction and repulsion, or quantum statistics correlations. It has been investigated that no detectors effect is contributing in these depletions.

The centrality dependence of pion balance function is quantified by understanding the shape of the balance function distribution. It is done by measuring second moment of distributions (called standard deviation) in Δy and $\Delta\varphi$ and this standard deviation is called width of distribution. Fig. 4-9 shows centrality dependence of the width of the pion balance function distributions in Pb+Pb collisions at $\sqrt{S_{NN}}$ = 2.76 TeV for both Δy and $\Delta\varphi$. In the left panel of Fig. 4-9, two different ranges of $\Delta\varphi$ ($|\Delta\varphi| < \pi/2, |\Delta\varphi| < \pi$) are used. It is oberved from Fig. 4-9 that

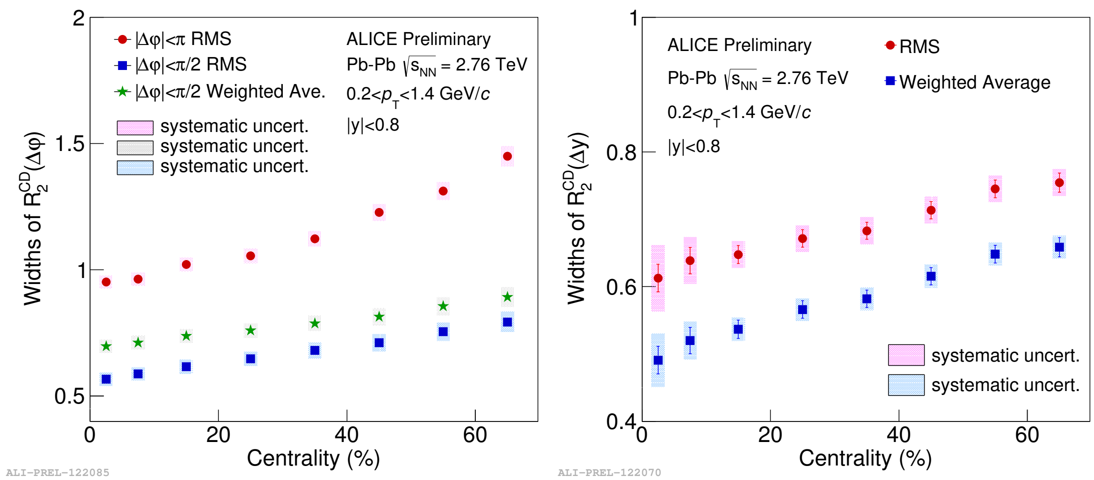

Figure 4-9: (Color online) [ALICE preliminary] The Centrality dependence of width in $\Delta\varphi$ (left plot) and Δy (right plot) for Pb+Pb collisions at $\sqrt{S_{NN}}$ = 2.76 TeV. The transverse momentum used in this plot is within the range $0.2 < p_T < 1.4$ GeV/c. 0-5% centrality is taken as most central collision and 60-70% centrality is taken as most peripheral collision.

the width of the balance function distributions changes as function of centrality. It is decreasing with increasing centrality. It is also observed that width of balance function in $\Delta\varphi$ space is larger when $|\Delta\varphi| < \pi$ is used. The broadening of the balance functions for less central collisions is a result of a larger separation between the balancing charges and higher kinetic freeze-out temperature. It is consistent with picture of delayed hadronisation in more central collisions as dicussed earlier in chapter 2. At low p_T region (0.2 GeV/c $< p_T < 1.4$ GeV/c), the centrality dependence of balance function could also be explained by collective flow in Pb+Pb collision system [18, 19, 20]. The observation of smaller width for central Pb+Pb collisions implies that production of charges occured at later times. If charges are produced at later times, their separation in coordinate space is small.

4.6.2 Systematic errors

Data points shown in figures of section 4.6.1 are shown also with the associated statistical and systematic errors. Systematic errors have been calculated on a bin-bin basis for pion balance function distributions and these errors are propagated to the moments of the distributions.

Systematic erros are obtained by varying event and track selection cuts. There are three components which are playing major roles in the systematic errors calculation for pion balance function. These are vertex-z cuts (V_z) of event, dca cuts of track and PID cuts. Final systematic error is calculated by taking the quadratic sum of all contributions. So systematic error in BF width is as shwon in Eq. 4.7.

$$\sigma_{sys} = \sqrt{\sigma_{V_z}^2 + \sigma_{dca}^2 + \sigma_{PID}^2} \tag{4.7}$$

V_z cuts of event

In this analysis , $|V_z| < 10$ cm is used. For systematic error calculation, $|V_z| < 8$ cm is used. Systematic error on V_z cut is summarized in Table. 4.1

Table 4.1: Systematic on V_z cut for BF width of pion.

Centrality	$\sigma_{\Delta y}$	$\sigma_{\Delta\varphi}$
0-5%	$< 0.19\%$	$< 0.57\%$
30-40%	$< 0.1\%$	$< 0.23\%$
60-70%	$< 0.18\%$	$< 0.48\%$

dca cuts of track

In this analysis, $dca_{xy} < 2.4$ cm and $dca_z < 3.2$ cm are used. Here $dca_{xy} < 0.3$ cm and $dca_z < 0.3$ cm are used for systematic analysis for balance function distribution. The systematic errors for dca cuts on balance function width is shown in Table. 4.2.

Table 4.2: Systematic on dca cut for BF width of pion.

Centrality	$\sigma_{\Delta y}$	$\sigma_{\Delta\varphi}$
0-5%	$< 0.22\%$	$< 0.21\%$
30-40%	$< 1.6\%$	$< 1.0\%$
60-70%	$< 1.2\%$	$< 1.1\%$

PID cuts

In this analysis, PID cuts are used as an independent systematic error and electron rejection cut $< 3\sigma_{electron}$ is used. For systematic analysis, electron rejecetion cut $< 1\sigma_{electron}$ is used. The maximum contribution due to this electron rejection cut to systematic error is around 0.1%.

4.6.3 Discussions

The experimental observable balance function in relative azimuthal angle and in relative pseudorapidity/rapidity of the particle pair gives a hint of hadronisation time of the produced system in heavy ion collisions. In this work, ALICE data have been used to measure balance functions of identified particles. We have measured the balance function distributions for Pb+Pb collisions at $\sqrt{s_{NN}}$ = 2.76 TeV taken by ALICE experiment for pions as trigger and associated particles. We have observed that the width of the balance function in terms of Δy and $\Delta\varphi$ for pions decrease when moving from peripheral to central collisions. It is consistent with the picture of a delayed hadronisation.

It is observed that balance function distributions of pions for Pb+Pb collisions at $\sqrt{s_{NN}}$ = 2.76 TeV have narrower distribution with respect to balance function distributions of pions for Au+Au collisions at $\sqrt{s_{NN}}$ = 200 GeV [21]. It shows that balance function width decreases if system size and energy increase. Collective flow in Pb+Pb collisions at $\sqrt{s_{NN}}$ = 2.76 TeV is higher than value in Au+Au collisions at $\sqrt{s_{NN}}$ = 200 GeV. Collective flow makes balancing charges for staying correlated in momentum space. Therefore, balance function distributions are more narrower for large system size and higher energy.

Bibliography

[1] S.H. Morgan Jr.: "Nuclear Instruments and Methods", P.B. Eby Volume 106, Issue 3, Pages 413-627 (February 1973).

[2] Mikios Gyulassy, Xin-Nian Wang, Computer Physics Communications 83 (1994) 307-331

[3] N. Armesto, C.A. Salgado, U.A. Wiedemann,Phys. Rev. Lett.93, (2004), 242301.

[4] A. Majumder, B. Muller, S.A. Bass,Phys. Rev. Lett.99,(2007),042301.

[5] C.B. Chiu, R.C. Hwa, Phys. Rev. C 72, (2005),034903.

[6] C.-Y. Wong,Phys. Rev. C 78,(2008), 064905.

[7] A. Dumitru, F. Gelis, L. McLerran, R. Venugopalan, Nucl. Phys. A 810, (2008),91-108 .

[8] S. Gavin, L. McLerran, G. Moschelli, Phys. Rev. C 79, (2009), 051902 .

[9] P. Romatschke, Phys. Rev. C 75, (2007),014901 .

[10] E.V. Shuryak, Phys. Rev. C 76,(2007), 047901 .

[11] K. Dusling, D. Fernandez-Fraile, R. Venugopalan, Nucl. Phys. A 828,(2009), 161-177.

[12] S.A. Voloshin, Two particle rapidity, Nucl. Phys. A 749, (2005),287-290 .

[13] J. Takahashi, B.M. Tavares, W.L. Qian, R. Andrade, F. Grassi, Y. Hama, T. Kodama, N. Xu, Phys. Rev. Lett. 103,(2009), 242301 .

[14] B. Alver, G. Roland, Phys. Rev. C 81,(2010), 054905 .

[15] B.H. Alver, C. Gombeaud, M. Luzum, J.-Y. Ollitrault, Phys. Rev. C 82,(2010), 034913 .

[16] Y. Hama, R.P.G. Andrade, F. Grassi, W.-L. Qian, Nonlinear Phenom. Complex Syst. 12,(2009), 466-470 .

[17] P. Bozek, W. Broniowski,Phys. Rev. Lett. 109, (2012), 062301 .

[18] ALICE Collaboration, Eur. Phys. J. C 76 (2016) 86

[19] P. Bozek Phys. Lett. B, 609 ,(2005), 247.

[20] S. Voloshin Phys. Lett. B, 632, (2006),490.

[21] STAR Collaboration: Phys. Rev. C 82,(2010), 024905.

Chapter 5

Balance function as an observable for Chiral Magnetic Effect (CME) : a model studies

5.1 Introduction

The Chiral magnetic effect (CME) [1] is the phenomenon of electrical charge sepatation in the presence of an external magnetic field induced by imbalance of a chirality (basically there is an imbalance between densities of right handed and left handed chiral fermions). Here an electromagnetic current is created along the direction of magnetic field. Several experimental measurements have been dedicated towards the search for the CME at RHIC and LHC [2, 3, 4, 5, 6]. In condensed matter systems, the CME is also studied [7].

In QCD, there are special gauge field configurations which are characterized by a topological invariant quantity called winding number Q_w [8]. The winding number which is an integer is defined by

$$Q_w = \frac{g^2}{32\pi^2} \int d^4x F^a_{\mu\nu} \tilde{F^{\mu\nu}_a} \tag{5.1}$$

Here g represents QCD coupling constant. The gluonic field tensor is represented by $F^a_{\mu\nu}$ and its dual is represented by $\tilde{F^{\mu\nu}_a}$. The non-zero value of Q_w arises because of renormalization of the theory [9] cannot be performed in a chirally invariant way. So flavour singlet axial current $j^\mu_5 = \bar{\psi_f}\gamma_\mu\gamma_5\psi_f$ is no longer conserved even in chiral limit i.e m $\rightarrow 0$ limit where ψ_f is a quark field and $\left\{\gamma_\mu\right\}_{\{\mu=0,1,2,3\}}$ is Dirac matrices. One can observe it from Eq. 5.2

$$\partial^\mu j^\mu_5 = 2\sum_j m_f \langle\bar{\psi_f}\mathrm{i}\gamma_5\psi_f\rangle_A - \frac{N_f g^2}{16\pi^2} F^a_{\mu\nu}\tilde{F^{\mu\nu}_a} \tag{5.2}$$

Here, N_f represents number of quark flavour, ψ_f a quark field, m_f quark mass. The spatial integration of Eq. 5.2 gives rate of the chirality change induced by topological gauge field configurations. It is given in Eq. 5.3. Here chiral limit is chosen i.e m_f =0. N_R and N_L represent net number of quarks with right handed and left handed chirality. Bacially, N_R is sum of the number of right-handed quarks and right-handed anti-quarks. Similarly N_L is sum of the number of left-handed quarks and left-handed anti-quarks. Spin and momentum parallel to each other for right handed massless fermions and for left handed massless fermions, spin and momentum are antiparallel. At time t = $-\infty$, it is assumed that there is an equal number of right-handed and left-handed fermions i.e $N_R = N_L$.

$$\frac{d(N_R - N_L)}{dt} = -\frac{N_f g^2}{16\pi^2} \int d^3x F^a_{\mu\nu} \tilde{F^{\mu\nu}_a} \tag{5.3}$$

At time t = ∞, using Eq. 5.1 and integrating Eq. 5.3 with respect to time, one can get

$$(N_R - N_L)_(t = \infty) = -2N_f Q_w \tag{5.4}$$

From Eq. 5.4, it is observed that a gauge field configuration with positive Q_w converts right-handed fermions into left-handed fermions and this field configuration can separate charge in presence of an electromagnetic field. Chiral magnetic effect is illustrated in Fig. 5-1. Because of large magnetic field, all quarks have a lowest Landau level.

Along the magnetic field direction, spins of quarks are aligned and spins of quarks with opposite charges are alligned antiparallel to the magnetic field direction. The right handed fermions with postively charged and the left handed fermions with negatively charged move in upward direction along magnetic field. Similarly the right handed fermions with negatively charged and the left handed fermions with positively charged move in downward direction opposite to magnetic field. Now these fermions interact with gauge field configuration with non-zero Q_w and left handed fermions convert to right handed fermions by reversing momentum if Q_w is negative. After interaction with gauge field, a difference between right handed and left handed fermions is created and it generates an

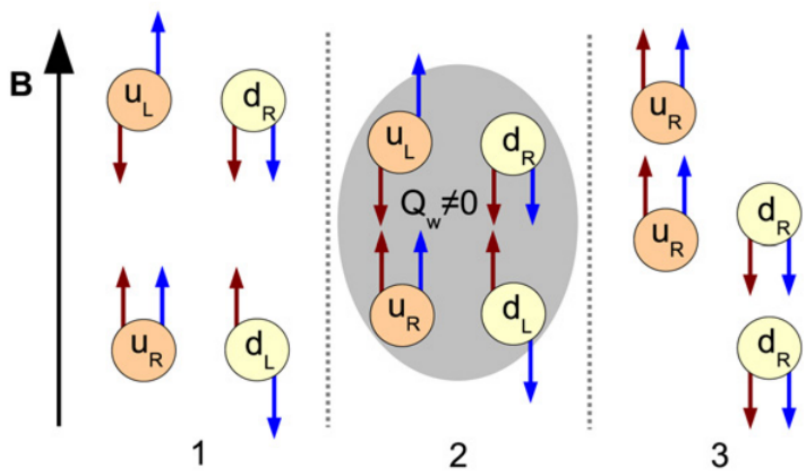

Figure 5-1: Illustrative description of chiral magnetic effect in the presence of large magnetic field. The red arrows and blue arrows represent momentum and spin of quarks respectively as shown in left panel. Up and down quarks have lowest Landau level in the presence of a large magnetic field. Initially there are equal number of right handed and left handed quarks. Now these quarks interact with a gauge field configuration with non-zero negaive Q_w and a left handed up or down quark converts to right handed up or down quark by reversing the momentum direction as shown in middle panel. Because of this, there is a motion of right handed up quarks in upward direction and right handed down quarks in downward direction as shown in right panel. A charge difference of Q = 2e will be created between two sides of a plane perpendicular to the magnetic field [8].

electromagnetic current along the magnetic field direction. This current creates a charge separation in the perpendicular direction of magnetic field.

5.2 Balance function and elliptic flow of pions probing CME: model studies

In this chapter, we will discuss about probing chiral magnetic effect using balance function of all charged particles and elliptic flow of pions [10].

It has been estimated that in high energy heavy-ion collisions, spectator protons produce a strong magnetic field $eB_y \approx m_\pi^2$ or $\sim 3.14 \times 10^{14}$ T [11]. A P- and CP-odd domain in the presence of a large magnetic field can generate chirality by inducing up-down asymmetry in the production of quarks and antiquarks. This asymmetry should be reflected in the final hadron production mainly of pions. An electric dipole moment pointed from the negative charge to the positive charge direction is created because of this charge separation. In this work, we have implemented this charge separation in a heavy-ion event generator known as A Multi-Phase Transport (AMPT) model via creating electric dipole moment at the partonic level. The details about AMPT model & introduction to CME have been described in section 5.2.1.

We propose two observables widely used in heavy ion collisions i.e the balance function of charged particles and the elliptic flow of pions as the observables for the CME. These observablese are discussed in chapter 2 and 1 respectively. In this work we have studied the sensitivity of the BF structure with the varying fraction of charge separation.

In Ref. [12] it has been suggested that the gamma correlator i.e two particle correlation γ is defined as $< cos(\varphi_1 + \varphi_2 - 2\psi_{RP}) >$ where ψ_{RP} is the reaction plane angle and φ_1, φ_2 denote the azimuthal angles of the produced charged particles. γ is sensitive to the CME effects.

The azimuthal distribution of produced particles with parity odd observables may have the following form

$$\frac{dN}{d\phi} \sim 1 + \sum_{n=1}^{\infty} (2v_n \cos[n(\phi - \Psi_R)] + 2a_n \sin[n(\phi - \Psi_R)]) \tag{5.5}$$

where ϕ is the azimuthal angle and Ψ_R is the reaction plane angle. *Sine* term represents the charge separation and the parameter a_n describes the parity violation effect. We have calculated these parity violation terms in the form of balance function moments as discussed in ref. [13]. The gist of this ref. [13] has been discussed below.

We know $\gamma_P = \cos(\phi_i + \phi_j) = \cos(2\phi_i)\cos(\Delta\phi) - \sin(2\phi_i)\sin(\Delta\phi)$ where P stands for parity and $\Delta\phi = \phi_j - \phi_i$. γ_P can be expressed when weighted with azimuthal distribution of particles as

$$\gamma_P = \langle C_b \cos(2\phi) \rangle - \langle S_b \sin(2\phi) \rangle \tag{5.6}$$

where

$$C_b = \frac{1}{Z_b} \int d\Delta\phi B(\Delta\phi) \cos(\Delta\phi), \tag{5.7}$$

$$S_b = \frac{1}{Z_b}\int d\Delta\phi B(\Delta\phi)\sin(\Delta\phi), \tag{5.8}$$

$$Z_b = \int d\Delta\phi B(\Delta\phi) \tag{5.9}$$

Z_b is the integral of balance function used as normalization factor. We have used trigger and associated particles in the ϕ range of $-\pi$ to π. Balance function being a function of $\Delta\phi$ is therefore independent of ϕ. $\langle C_b\cos(2\phi)\rangle$ and $\langle S_b\sin(2\phi)\rangle$ could therefore be written as $C_b\langle\cos(2\phi)\rangle$ and $S_b\langle\sin(2\phi)\rangle$ respectively.

From Eq.5.5 one can get the n-th harmonic co-efficient defined as v_n is $\langle\cos[n(\phi - \Psi_R)]\rangle$ where $\langle..\rangle$ denotes average over particles [14, 15]. The second Fourier coefficient v_2 called elliptic flow $\langle\cos(2\phi)\rangle$ is the quantity of our interest. In our simulation Ψ_R is taken as 0 as per the implementation of AMPT model. In a non-central heavy ion collision, a pressure gradient in azimuthal angle is established because of the initial spatial anisotropy [16]. Due to this, pressure gradient along in-plane is higher than along the out-of-plane. So more particles are emitted in-plane than out-of-plane and it gives a positive elliptic flow coefficient. However, observed v_2 has also been explained in transport model as due to anisotropic escape of partons [17, 18].

In section 5.2.2, we have described the method of charge separation that is implemented at the quark level in AMPT model. In section 5.2.3 and 5.2.4 , we have discussed results and summary respectively.

5.2.1 A MULTI-PHASE TRANSPORT MODEL

In this work, we have implemented charge separation at the partonic level in Au+Au collisions at $\sqrt{s_{NN}}$ = 200 GeV using the AMPT model. The AMPT model consists of different components with the heavy ion jet interaction generator (HIJING) to implement the initial conditions, Zhang's parton cascade (ZPC) for modelling the partonic scatterings, the Lund string fragmentation model or a quark coalescence model for hadronization, and a relativistic transport (ART) model for hadronic rescattering[19, 20, 21]. HIJING provides spatial and momentum distributions of the minijet partons and of the soft string excitations [22, 23]. The cascading of partons are carried out using the ZPC model [24]. Partonic cross sections between 1 and 3 mb have been used for flow like studies using this model. However, in Ref [25] in which CME effect has been simulated using AMPT, parton cross-section of 10 mb has been used to explain STAR data. We have, therefore, used 10 mb partonic cross-section for this work. AMPT model has two versions , one is the Default AMPT and the other is the string melting(SM) version. In the default AMPT model, partons are combined with their parent strings when they stop interacting and the resulting strings are converted to hadrons using the Lund string fragmentation model [26, 27, 28]. In the AMPT with string melting [29, 30, 31], a quark coalescence model is used instead to combine partons into hadrons. In the string melting mechanism, all excited strings that are not from the projectile or the target nucleons or without any interactions are converted to partons according to the flavor and spin structures of their valence quarks. Subsequently the dynamics of the hadronic matter is described by a hadronic cascade, which is based on the ART model [32, 33]. In the ART model, charges are not conserved. We have used NTMAX = 3 for minimising rescattering among hadrons. If one excludes hadron evolution in string melting model, main contribution of evolution are carried by parton cascade.

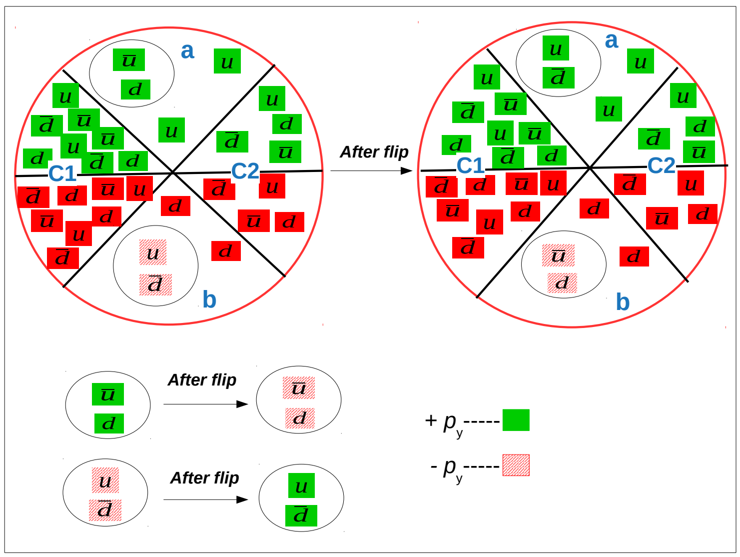

Figure 5-2: (Color online) Charge Separation mechanism shown schematically

5.2.2 PROCEDURE OF GENERATING CHARGE SEPARATION

The manifestation of the chiral magnetic effect is seen by a charge separation along the direction of the magnetic field. The charge separation is a result of P and CP odd domains. According to theory, in non-central heavy ion collisions, spectator protons create a magnetic field perpendicular to the reaction plane. We thus introduce a charge separation perpendicular to the reaction plane. Fig. 5-2 shows schematically the method of charge separation mechanism we have implemented in AMPT-SM model.

In AMPT, RP angle is at 0°. To have a direction of charge separation perpenidcular to RP, we first choose u, $\bar{u}$, d and $\bar{d}$ which have azimuthal angle between $\mid 1.0472^{c} \mid$ to $\mid 2.0944^{c} \mid$ i.e lying in regions $\mathbf{a}$ and $\mathbf{b}$ in Fig. 5-2. p_y momenta of the quarks in those selected regions are then modified in such a way that it results in a net positive charge in the upward direction and a net negative charge in the downward direction. Please note that quarks of other regions remain unchanged. The main purpose of selecting quarks from these two regions .i.e region $\mathbf{a}$ and $\mathbf{b}$ is to simulate a scenario of the CME where charge separation is created perpendicular to the RP and in-plane quarks remain unaffected.

To achieve this, we replace a fraction of total number of upward going negatively charged quarks with downward going positively charged quarks and vice versa. In practice, $-p_y$ of a positively charged u quark and $+p_y$ of a negatively charged $\bar{u}$ quark are flipped to each other making positively charged quark upgoing and negatively charged quark downgoing. Similarly flipping takes place between the $+p_y$ of a negatively charged d quark with the $-p_y$ of a positively charged $\bar{d}$ quark. This charge separation method was used in Ref.[25]. As shown in the Fig. 5-2, before flipping, each of the regions marked with $\mathbf{a}$ and $\mathbf{b}$ lying perpendicular to the reaction plane is with net-charges of $\frac{1}{3}e$. Now after flipping the corresponding regions are with charges of $\frac{7}{3}e$ and$-\frac{5}{3}e$ respectively thereby generating a charge separation perpendicular to the reaction plane. After the implementation of flipping at the partonic level, the evolution of the system follows. The fraction (f) of the total number of quarks that have been flipped is taken as an input parame-

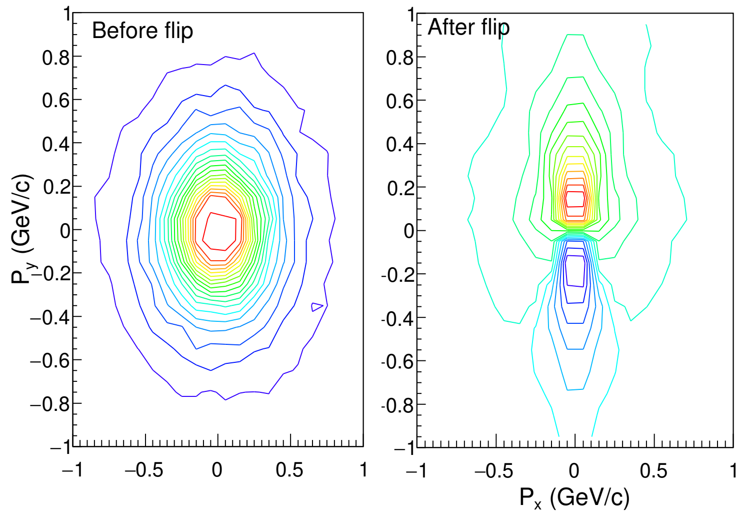

Figure 5-3: (Color online) Net electric charge distributions on the transverse plane before and after flipping with a 20% flipping fraction.

ter. We have calculated multiplicities of $\bar{u}$ and d quarks separately in the region **a** i.e $M^{\mathbf{a}}_{\bar{u}}$ and $M^{\mathbf{a}}_{d}$ respectively. Similarly multiplicities $M^{\mathbf{b}}_{u}$ & $M^{\mathbf{b}}_{\bar{d}}$ of u and $\bar{d}$ quarks respectively in region **b** have been obtained. $M^{\bar{u},u}_{small}$ = min ($M^{\mathbf{a}}_{\bar{u}}, M^{\mathbf{b}}_{u}$) & $M^{\bar{d},d}_{small}$ = min ($M^{\mathbf{b}}_{\bar{d}}, M^{\mathbf{a}}_{d}$). We then calculate $f \times M^{\bar{u},u}_{small}$ for every event and this number is the number of ($u, \bar{u}$) quarks to be flipped by exchange of p_y momenta. Similar procedure has been followed for d and $\bar{d}$. In this work, f = 0, 0.1, 0.2, 0.3, 0.4, 0.5, and 0.6 have been used. The AMPT-SM has been used in which the quarks are hadronized by coalescence method as discussed earlier. The observable discussed in chapter 2 and elliptic flow have been studied for the finally produced hadrons. In high-energy heavy-ion collisions, these observables might be studied with centrality as the magnitude of the magnetic field created in such collisions depends on centrality. In the present study, different magnitudes of charge separation as given by f represent different magnitudes of the produced magnetic field and can be compared with collisions of various centralities.

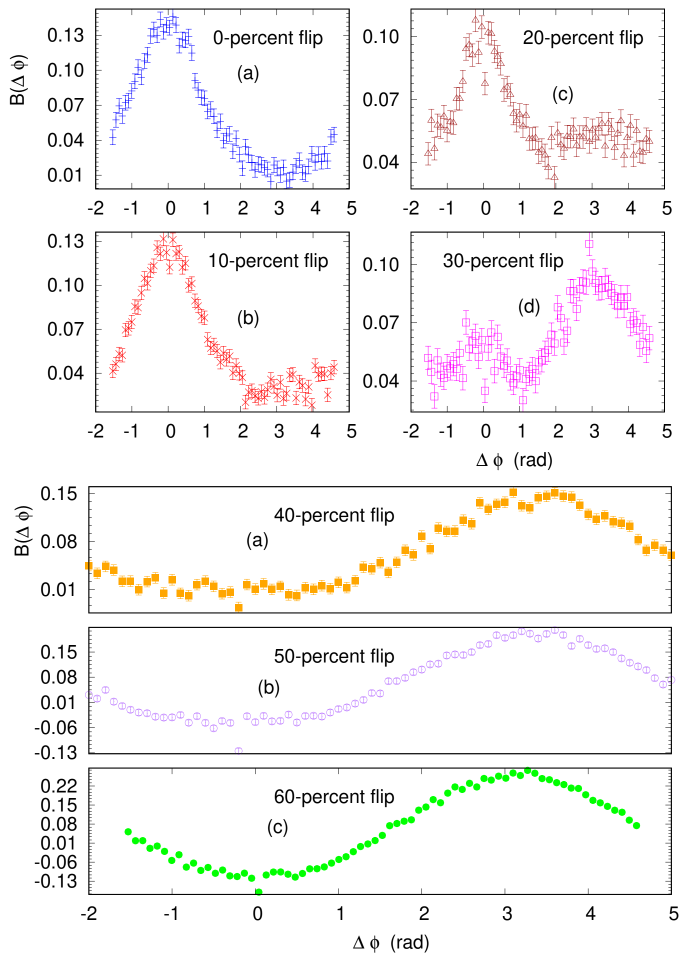

Figure 5-4: (Color online) BF for Au+Au minimum bias at $\sqrt{s_{NN}}$ = 200 GeV with different flipping fractions from 0 to 60 %

5.2.3 Results

Fig. 5-3 shows the net electric charge distributions on the transverse plane before and after flipping of quarks in Au+Au collisions at $\sqrt{s_{NN}}$ = 200 GeV. The contours indicate the net charge density profile. One can see that the distribution is symmetric when there is no charge separation. There is a net electric charge distribution on the transverse plane after flipping 20 $\%$ of quarks. It is clearly observed that an out-of-plane charge separation is generated after introduction of charge separation effects in the AMPT model. Fig. 5-4 show the charged particle balance function at different flipping fractions. It is clearly seen that the shape of the balance function evolves with the flipping fraction. While without flipping, it shows a peak$\sim 0^c$, the peak shifts towards π^c when flipping for charge separation is 30 $\%$ or greater. For parity violation, balance function should have a peak at $\Delta\phi \sim \pi^c$ [13]. We have studied the effect of the widely used observable i.e γ-correlator on BF. γ_P correlator in the form of BF's moment as defined in Eq. 5.6 is shown in Fig. 5-5. We have also shown γ_P averaged with N_{part} (number of participants) distribution as defined in Eq. 5.10 in Fig. 5-6.

$$\langle\gamma_P(N_{part})\rangle = \frac{\int d(N_{part})\gamma_P(N_{part})N_{part}}{\int d(N_{part})N_{part}} \tag{5.10}$$

where $\int d(N_{part})N_{part}$ is the N_{part} distribution. In this work, we have used impact parameter range from 0 to 12 fm and N_{part} in the range of 21 to 392.

Fig. 5-5 shows that the parity odd observable in form of BF moments becomes negative when flipping fraction is ~ 30 $\%$ or higher. This signifies the presence of

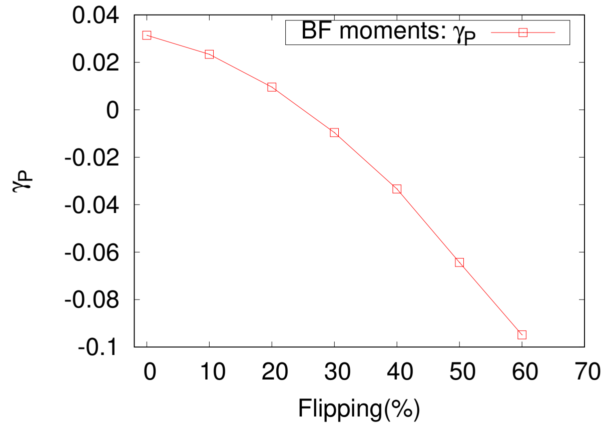

Figure 5-5: (Color online) γ-correlator in the form of BF's moment with different flipping fractions

more balancing pairs in out-of-plane relative to that of in-plane direction. It may be noted that this effect is due to the 2^{nd} term in Eq. 5.6 which arises due to the CME effect.

Fig. 5-6 shows that $<\gamma_P>$ with same charges and opposite charges have nega-

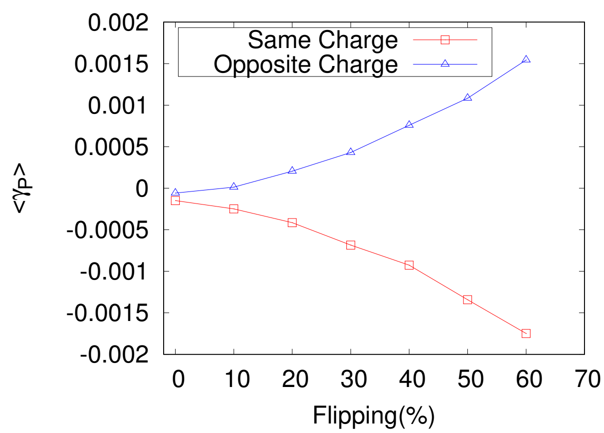

Figure 5-6: (Color online) $<\gamma_P>$ with different flipping fractions

tive and positive values respectively. This figure indicates that gamma correlator has larger magnitudes with higher flipping fraction for both same and opposite charge correlation. γ-correlator used in [34] as an observable also shows similar trend thereby showing that the CME effect implemented in AMPT model is reasonable. It should be mentioned that Fig. 5-6 in this work and plot in Ref.[25] might look similar. However, in this work, in Fig. 5-6, we have plotted the gamma correlator averaged with N_{part} vs flipping fractions. In Ref.[25], gamma correlator is plotted with different centralities. As the event with different flipping fractions might be related with centrality, a connections may be drawn between two cases. Fig. 5-7 shows the elliptic flow(v_2) of pions as a function of p_T for different flipping

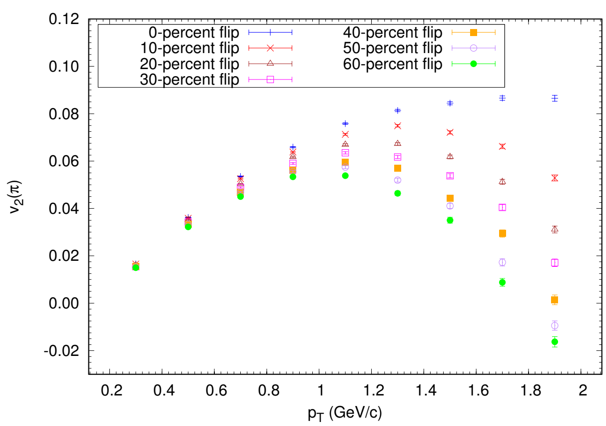

Figure 5-7: (Color online)Elliptic flow of pions for different flipping fractions and no flip

fractions in the initial partonic state of the collisions. It is observed that the elliptic flow of pion increases upto $p_T \sim 1.1$ GeV/c and then decreases at higher p_T. There is an increase in out-of plane particle production , so v_2 shows a decreasing trend for higher flipping fractions. So elliptic flow is sensitive to the CME effects because of out-of-plane charge separation and it shows a strong decreasing trend.

5.2.4 SUMMARY

In this study, momenta of initial partons of AMPT generator have been flipped to generate an out-of-plane charge separation in Au+Au collisions at $\sqrt{s_{NN}}$ = 200 GeV. The fraction of a type of quark(u,$\bar{u}$,d,$\bar{d}$) to be flipped has been taken as a variable. This charge separation represents the effect of parity-odd observable in heavy ion collisions where magnetic fields are generated. We have studied the effect of this charge separation on two widely used observables i.e charge particle BF and elliptic flow of pions. γ-correlator has also been used for comparison. The observables are chosen in such a way that they characterize the effect of net-charge and their distribution on azimuthal plane. Different fractions represent varying centrality in such collisions. In this study, with varying fraction of flipping, both the BF and v_2 show significant sensitivity with the peak of the BF shifting from $\Delta\phi = 0$ towards $\Delta\phi = \pi$ with increasing flipping fraction and v_2 of pions decreases at higher p_T. The reduction in v_2 with respect to no-flipping scenario depends on the flipping fraction. The gamma correlator in form of BF moment with different flipping fraction shows a decreasing trend. We also notice that $< \gamma_P >$ for same charge correlation and opposite charge correlation have opposite values and varies with charge separation. Experimentaly, the STAR has an upper limit for the value of gamma correlator of the order of 10^{-3}. We have observed that the gamma correlator of $\approx 10^{-3}$ corresponds to flipping fractions range of 0 to 60$\%$. We hereby propose to look at both the observables i.e BF and elliptic flow together for making an unambiguous conclusion on the generation of parity-odd effects in high energy heavy ion collisions.

Bibliography

[1] K. Fukushima, D. E. Kharzeev, and H. J. Warringa, Phys.Rev. D 78, 074033 (2008).

[2] B.I. Abelev, et al., ALICE Collaboration Phys. Rev. Lett., 110 (2013), 012301.

[3] B.I. Abelev, et al., STAR Collaboration Phys. Rev. Lett., 103 (2009), 251601.

[4] B.I. Abelev, et al., STAR Collaboration Phys. Rev. C, 81 (2010), 054908.

[5] L. Adamczyk, et al., STAR Collaboration Phys. Rev. C, 88 (2013), 064911.

[6] L. Adamczyk, et al., STAR Collaboration Phys. Rev. Lett., 113 (2014), 052302.

[7] Qiang Li, Dmitri E. Kharzeev, Nuclear Physics A, 956, (2016), 107-111.

[8] Kharzeev, D.E., McLerran, L.D., Warringa, H.J, Nucl. Phys. A803, 227-253 (2008).

[9] R.D. Peccei, H.R. Quinn, Phys. Rev. D 16 (1977) 1791; S. Weinberg, Phys. Rev. Lett. 40 (1978) 223.

[10] S.N Alam, S.Chattopadhyay, "Effect of simulating parity-odd observables in high energy heavy ion collisions on balance functions of charged particles and elliptic flow of pions ", Nulcear Physics A 977 (2018) 208-216

[11] Kharzeev, D.E., McLerran, L.D., Warringa, H.J, Nucl. Phys. A803,(2008), 227-253.

[12] S.A Voloshin, Phys.Rev.C 70 (2004) 057901

[13] Schlichting, Pratt, Phys. Rev. C 83 (2011) 014913, S.Pratt, arXiV:1002:1758v1

[14] S. Voloshin and Y. Zhang, Z. Phys. C 70,(1996), 665 .

[15] A. M. Poskanzer and S. A. Voloshin, Phys. Rev. C 58,(1998),1671 .

[16] R. Snellings, New J. Phys. 13, (2011),055008 .

[17] Z.W. Lin et al. Nuclear Physics A 956,(2016), 316-319 .

[18] Liang He et al. Physics Letters B 753,(2016), 506-510 .

[19] B. Zhang, C.M. Ko, B.A. Li, Z.W. Lin, Phys. Rev. C 61 (2000) 067901.

[20] Z.W. Lin, S. Pal, C.M. Ko, B.A. Li, B. Zhang, Nucl. Phys. A 698 (2002) 375.

[21] Z.W. Lin, C.M. Ko, B.A. Li, B. Zhang, S. Pal, Phys. Rev. C 72 (2005) 064901.

[22] X.N. Wang, M. Gyulassy, Phys. Rev. D 44 (1991) 3501.

[23] M. Gyulassy, X.N. Wang, Comput. Phys. Commun. 83 (1994) 307.

[24] B. Zhang, Comput. Phys. Commun. 109 (1998) 193.

[25] Guo-Liang Ma,Bin Zhang, Physics Letters B 700 (2011) 39-43.

[26] B. Andersson, G. Gustafson, and B. Soderberg, Z. Phys. C 20,(1983), 317 .

[27] B. Andersson, G. Gustafson, G. Ingelman, and T. Sjostrand,Phys. Rep. 97, (1983), 31 .

[28] T. Sjostrand, Comput. Phys. Commun. 82,(1994), 74 .

[29] Z. W. Lin and C. M. Ko, Phys. Rev. C 65,(2002), 034904 .

[30] Z. W. Lin, C. M. Ko, and S. Pal, Phys. Rev. Lett. 89,(2002), 152301 .

[31] Z. W. Lin and C. M. Ko, J. Phys. G 30,(2004), S263 .

[32] B. A. Li and C. M. Ko, Phys. Rev. C 52,(1995), 2037 .

[33] B. Li, A. T. Sustich, B. Zhang, and C. M. Ko, Int. J. Mod.Phys. E 10,(2001), 267.

[34] B. I. Abelev et al. (STAR Collaboration), Phys. Rev. Lett.103, (2009),251601.

Chapter 6

Discussions

In this chapter, we have summarized discussion of ALICE experimental results of balance function distributions of pions for Pb+Pb collisions at $\sqrt{s_{NN}}$ = 2.76 TeV and probing chiral magnetic effects in heavy ion collisions using balance function of all charged particles produced using AMPT model. In section 6.1, balance function results are desrcibed and in section 6.2 balance function giving description of chiral magnetic effects is described.

6.1 ALICE results for balance function of pions

Balance function observable is an excelent observable which can give information regarding hadronisation time of produced system in high energy heavy ion collisions. A correlation in relative rapidity/pseudorapidity or in relative azimuthal angle between two charged particles is measured by balance function as mentioned in ref. [1] of chapter 2. We have presented results on the BF measured for pions at Pb+Pb collisions at $\sqrt{s_{NN}}$ = 2.76 TeV in ALICE experiment. We have analyzed ALICE data for 8 centrality bins. 0-5% centrality bin is called most central collisions and 60-70% centrality bin is called most peripheral collisions. The width of the balance function distribution (variance of distribution) is used to quantify the correlation strength between particles in pair. The widths of the BF of pions measured in Δy and $\Delta\varphi$ decrease with increasing centrality i.e peripheral to central collisions. So for most central collisions, there is a small separation between balancing charges compared to peripheral collisions. It means balancing pairs are strongly correlated in phase space defined by Δy and $\Delta\varphi$ for most central collisions. It suggests that charges are created at later times. It hints that there is a delayed hadronisation of the produced system.

In BF distributions of pions, a dip at ($\Delta y, \Delta\varphi$) = (0,0) is observed. It is because of mainly coulomb force between balancing charges or quantum statistics correlations. The BF distributions of pions in Pb+Pb collisions at $\sqrt{s_{NN}}$ = 2.76 TeV have narrower distribution than distributions from Au+Au collisions at $\sqrt{s_{NN}}$ = 200 GeV. The width of balance function has energy and system size dependence. It could be explained as a result of collective flow. Collective flow has larger value in large system size as well as for higher energy. It gives a hint that system produced in high energy heavy ion collisiions exist for a substantial amount of time.

6.2 Chiral magnetic effect using balance function

Chiral magnetic effect is the effect of charge separation in heavy ion collisions at the presence of external magnetic field (spectator nucleons produce magnetic field). The BF measures strength of charge separtion in balancing charges,therfore BF should be a good obervable for analysing CME. Elliptic flow also a good observable for describing chiral magntic effect because charge separtion takes place perpendicular to reaction plane. Charge separation means there is a certain distance between positive and negative charged particles. Therefore a dipole is formed. For analysing CME using BF of all charged particles produced by AMPT model, a dipole moment has been created by flipping momenta of some fraction of quarks perpendicular to reaction plane. This fraction has been taken as a variable.

We have observed that BF shows a peak towards π^c from 0^c when flipping fraction is 30$\%$ or greater. It gives that more balancing pairs are emitted in the direction perpendicular to the reaction plane for large flipping fraction.

CME effect is the effect of parity violation in the strong interaction between quarks. CME is quantified by γ correlator. We have observed that BF moments of γ correlator have negative values when flipping fraction is 30$\%$ or greater. We also have observed that γ correlator averaged with number of participants give negative values for same charges and positive values for opposite charges. Elliptic flow of pions shows a decreasing trend for higher flipping fractions. Therefore v_2 is sensitive to CME because of large out of plane charge separation.